INFORMATION TO USERS

This material was produced from a microfilm copy of the original document. While the most advanced technological means to photograph and reproduce this document have been used, the quality is heavily dependent upon the quality of the original submitted.

The following explanation of techniques is provided to help you understand markings or patterns which may appear on this reproduction.

1. The sign or "target" for pages apparently lacking from the document photographed is "Missing Page(s)". If it was possible to obtain the missing page(s) or section, they are spliced into the film along with adjacent pages. This may have necessitated cutting thru an image and duplicating adjacent pages to insure you complete continuity.

2. When an image on the film is obliterated with a large round black mark, it is an indication that the photographer suspected that the copy may have moved during exposure and thus cause a blurred image. You will find a good image of the page in the adjacent frame.

3. When a map, drawing or chart, etc., was part of the material being photographed the photographer followed a definite method in "sectioning" the material. It is customary to begin photoing at the upper left hand corner of a large sheet and to continue photoing from left to right in equal sections with a small overlap. If necessary, sectioning is continued again — beginning below the first row and continuing on until complete.

4. The majority of users indicate that the textual content is of greatest value, however, a somewhat higher quality reproduction could be made from "photographs" if essential to the understanding of the dissertation. Silver prints of "photographs" may be ordered at additional charge by writing the Order Department, giving the catalog number, title, author and specific pages you wish reproduced.

5. PLEASE NOTE: Some pages may have indistinct print. Filmed as received.

University Microfilms International
300 North Zeeb Road
Ann Arbor, Michigan 48106 USA
St. John's Road, Tyler's Green
High Wycombe, Bucks, England HP10 8HR

77-12,738

HEYMSFIELD, Gerald M., 1949-
A DUAL DOPPLER INVESTIGATION OF SOME KINEMATIC AND DYNAMIC ASPECTS OF THE HARRAH TORNADIC STORM.

The University of Oklahoma, Ph.D., 1976
Physics, atmospheric science

Xerox University Microfilms, Ann Arbor, Michigan 48106

THE UNIVERSITY OF OKLAHOMA

GRADUATE COLLEGE

A DUAL DOPPLER INVESTIGATION OF SOME KINEMATIC AND DYNAMIC ASPECTS OF THE HARRAH TORNADIC STORM

A DISSERTATION

SUBMITTED TO THE GRADUATE FACULTY

in partial fulfillment of the requirements for the degree of

DOCTOR OF PHILOSOPHY

BY

GERALD M. HEYMSFIELD

Norman, Oklahoma

1976

A DUAL DOPPLER INVESTIGATION OF

SOME KINEMATIC AND DYNAMIC ASPECTS

OF THE HARRAH TORNADIC STORM

APPROVED BY

DISSERTATION COMMITTEE

ACKNOWLEDGEMENTS

I wish to express my gratitude to Dr. J. McCarthy, the chairman of my doctoral committee, for his support, encouragement and assistance during this work. I am deeply appreciative of my doctoral committee members, Drs. Doviak, Duchon, Inman, Kessler and Walker, who have given helpful assistance and comments on the final form of the dissertation. Discussions with Drs. Eddy, Fein, and Sasaki and Messrs. Steven Koch and Stephan Nelson also provided valuable insight into the work.

The broad support of the National Severe Storms Laboratory is acknowledged. Their cooperation in making available data for this study and permission for using the NSSL computer is appreciated. The Computer Data Processing group is given special acknowledgement.

The form in which this dissertation is presented is due to the patience of Miss Leslie Lippoldt, Ms. Peggy Hussey and Mrs. Joan Kimpel. Miss Lippoldt typed the first draft of the dissertation. Ms. Hussey typed the revised and final dissertation copies. Mrs. Kimpel has produced drafted copies of the figures.

This work was supported by the Atmospheric Research Section, National Sciences Foundation, (Grant ATM 74-0340 A02) and by NOAA (Grant 04-5-022-3).

ABSTRACT

The major emphasis of this work is to provide a detailed analysis of the Harrah tornadic storm on June 8, 1974, using dual Doppler radar observations from the National Severe Storms Laboratory. Emphasis is placed on the low and mid-level storm scale structure with length scales larger than about 5 km. Some inferences are made on the tornado scale, which is a sub-grid scale phenomenon.

The three-dimensional winds and reflectivity fields were computed. The radial velocity data for wind computations were interpolated to grids using the Eddy-Gandin statistical objective analysis. The vertical component was evaluated in cylindrical coordinates (Armijo, 1969). The accuracy of the three-dimensional winds depend on interpolation errors due to : (i) random observational errors; (ii) evolution and dissipation of storm structure over the data collection interval; and (iii) the assumption of the storm vector in adjustment of data to a common reference time. Tests were performed which suggest random errors in interpolated values are sufficiently large to require additional grid smoothing. The analysis is also sensitive to Taylor's hypothesis assumed in regard to (ii) and (iii).

Analysis of four data sets over a 28 min interval are presented. One cell in the Harrah storm is discussed in detail. This cell (A_1) has characteristics more in agreement with supercell storms. The observations for cell A_1 reveal a vortex doublet at mid-levels, a strong low-level inflow jet supplying warm moist air to a tilted updraft, and downdrafts on both storm flanks. The right flank downdraft reaches the surface along the front flank of the storm, while a weaker left flank downdraft undercuts the updraft and forms a gust front along the right rear flank. The low-level tornado cyclone exists between the low-level inflow and the descended air at the right rear flank. The mid-level vortex doublet is associated with an anticyclonically turning downdraft along the left flank, and a cyclonically rotating updraft.

The divergence and tilting terms in the vorticity equation are evaluated. The sum of these terms in the scaled vorticity equation is defined as vorticity production. The vorticity production at mid-levels was generally positive along the right flank and negative along the left flank of cell A_1. A mechanism for producing and intensifying the observed airflow is suggested on the basis of these calculations.

The motion of cell A_1 of the Harrah storm deviated only a few degrees to the right of the mean tropospheric wind. Two simple potential flow analogies are considered

(Appendix A) based on the observed mid-level vortex doublet. No net Magnus force is associated with a simple vortex doublet. On the other hand, if the updraft is considered as a cyclonically rotating barrier, the vortex doublet produces a large steering force. A few possible explanations are given for forces opposing the rightward steering force.

LIST OF TABLES

LIST OF SYMBOLS

a	radius of cylinder
$b,\hat{b}$	true and estimated ACF
C_p	pressure coefficient
d	2d is separation distance between radars
E	mean square interpolation error
e	residual error
F_d	force on cylinder along X-axis
F_s	force on cylinder along Y-axis
L_x,L_y,L_z	integral scales
P_r	average power received
R	range to center of radar gate
$\vec{r}_1(\Delta x',\Delta y',\Delta z)$	space lag of autocorrelation function
$\vec{S}$	advection vector
SNR	signal-to-noise ratio
T	time lag of autocorrelation function
T_0	reference (analysis) time
t	observation time
t'	time difference between observation time and reference time
U,V,W,X,Y,Z	Cartesian (tangent plane) wind components and coordinates (Y-axis directed North)
U_s,V_s	components of storm motion vector
u,v,w,x,y,z	Cartesian (tangent plane) wind components and coordinates (y-axis parallel to radar baseline)
$u_r,u_s,u_\alpha,r,s,\alpha$	cylindrical wind components and coordinates (s-axis parallel to radar baseline)

$\vec{V}$	absolute wind vector
$\hat{V}_{ai}, V_{ai}$	interpolated and true radial air motion at a grid-point for Norman (i=1) and Cimarron (i=2) radars
$\vec{V}_H$	300 mb wind vector
$\vec{V}_L$	850 mb wind vector
$\vec{V}_M$	700 mb wind vector
$\vec{V}_r$	wind vector relative to cell A_1
$\vec{V}_s$	motion vector of cell A_1
$\vec{V}_{WT}$	mass-weighted tropospheric wind vector
v_a, v_a'	true and measured pulse volume average of radial velocity of air
v_r, v_r'	true and measured pulse volume average of radial velocity of precipitation
v_T, v_T'	true and estimated pulse volume average of particle fallspeed
v_θ	rotational speed
x', y', z	Cartesian (tangent plane) coordinates with x'-axis parallel to radial passing through center of analysis grid
z	position in complex space
Z_e	effective radar reflectivity factor
z_m, z_0	cloud top height and cloud base height
$\Delta, \Delta x, \Delta y, \Delta z, \Delta r, \Delta s$	grid-spacings
$\sim$	matrix, or column vector
β	radar azimuth from North
$\delta, \delta_r, \delta_t$	fluctuating component of: radial air motions, radial precipitation motions, and terminal fallspeed term
ε	fraction of unexplained variance at a grid-point

ζ	vertical component of relative vorticity
θ	radar elevation angle
θ_s	saturation wet-bulb potential temperature
θ_w	wet-bulb potential temperature
κ	circulation strength
ρ	mass density
ρ_0	surface mass density
σ_T^2	total variance of radial air motion
$\sigma_u, \sigma_{u_s}, \sigma_v, \sigma_w$	error standard deviation of winds
$\sigma_{v_a}^2$	variance of true radial air motion
σ_δ^2	variance of fluctuations of radial air motion
σ_ζ	error standard deviation of divergence or vorticity
Φ	velocity potential
$\phi, \hat{\phi}$	model and predicted weight coefficients
Ψ	stream function
ω	complex potential

TABLE OF CONTENTS

TABLE OF CONTENTS--Continued

A DUAL-DOPPLER INVESTIGATION OF SOME KINEMATIC AND DYNAMIC ASPECTS OF THE HARRAH TORNADIC STORM

CHAPTER I

INTRODUCTION

Severe thunderstorms have been studied considerably in recent years. They are complex phenomena which encompass a wide range of scales of phenomena, from the synoptic scale down to the tornado scale. Dynamical, as well as thermodynamical and microphysical processes are operative in these storms. This work examines the airflow in a severe tornadic storm using dual-Doppler radar observations as the primary source of data. The storm scale airflow is important to our understanding of storm movement and tornado genesis. The recent advances in Doppler radar are enabling finer scale wind measurements so that we may obtain a better understanding of these processes. The rather broad scope of past severe storm investigations are related to the present study. More complete reviews are given elsewhere (e.g., Fujita, 1963; Newton, 1965; Davies-Jones and Kessler, 1974; and Browning, 1975).

Storm Classification

The first comprehensive investigation of thunderstorms resulted from the Thunderstorm Project (Byers and Braham, 1949). From this study emerged a model of an airmass thunderstorm which undergoes a regular life cycle of three stages of development: 1. growing; 2. mature; and 3. dissipating stages. Since then, severe thunderstorms have been studied considerably, and are found to be far more complex than the simple Byers and Braham model. Severe thunderstorms have been basically categorized according to three types: a. supercell, b. multicell, and c. squall line. A fourth type proposed by Marwitz (1972) has been called the severely sheared storm. The supercell type has been further subdivided into the severe right moving storm (SR) and the severe left moving storm (SL).

The supercell storm airflow model of the SR type was originally described in Browning and Ludlum (1962), and Browning (1965) as quasi-steady over a period greater than about 40 min, having three radar observed features: a. the wall, b. the echo overhang (presently called the embryo curtain in Browning and Foote (1975)), and c. the vault. The vault or weak echo region (WER) was defined by Browning as an echo free, but cloud-packed region of suspected intense updraft. The airflow model resulting from Browning (1965), Fankhauser (1971), and others is summarized by Davies-Jones and Kessler (1974):

a. Warm moist mT air flows into the storm's right front flank, rises in a tilted updraft, and exits the storm through the anvil.

b. Cooler, drier (low θ_e) mP mid-level (approximately 7 km) air enters the left flank of the storm. This air sinks due to evaporative cooling resulting from precipitation falling out of the updraft.

c. In lower levels, a "pseudo cold front", or flanking line is established as the descending rain-cooled air undercuts the moist potentially unstable updraft air. This is also a favorable location for new cell development.

d. As the "pseudo cold front" advances, a nearly steady state condition is established in which the updraft is continually regenerated.

While supercells are generally considered as an isolated storm, these storms are quite often observed with flanking lines of cumulus clouds (Lemon, 1974) which sometimes merge into the main updraft.[1,2] Perhaps the most notable characteristic of a supercell is a strong quasi-steady updraft. An alternative SR updraft structure was suggested by Danielson (1975) in which the updraft separates into a cyclonic

---

[1]Cell is defined in subsequent sections as any region in which a strong updraft existed at one time. This includes supercell and Byers and Braham type cells.

[2]Storm is defined as a cell or group of cells which appear to interact as an entity including environment immediate to the cell(s).

branch on the right rear storm flank and an anticyclonic branch along the left flank; downdrafts occur on both storm flanks. This type of downdraft structure has not been examined extensively, however.

The airflow in the SL was studied by Hammond (1967) and was inferred to be a mirror-image of the SR type. The SR was found (see e.g., Charba and Sasaki, 1971) to move 4.6 to 10.8 m s^{-1} slower than the mean tropospheric wind, in a direction 5° to 25° to the right of these winds. The SL was on the average 5.2 m s^{-1} slower and 37° to the left of the mean tropospheric wind direction. Quite often it is observed that SR and SL result from a splitting storm (e.g., Fujita and Grandoso, 1968; Actemeier, 1975). The angle between the splitting storms may be as large as 60°.

The multicell storm (Newton and Fankhauser, 1964; Chisholm, 1970; Marwitz, 1972) consists of cell clusters not formed in distinct lines, which continually evolve and migrate through the storm. Individual cells of the Byers-Braham type go through an evolutionary process having a total lifetime of about 60 min. The most favored region of cell development is along the right flank. First echoes typically occur at mid-levels (-12°C and 7 km) at approximately 15 min intervals.[3] These cells successively inten-

[3]First echoes are observed at mid-levels since growing raindrops first become detectable by radar at this level. The updraft associated with this cell would originate at lower levels.

sify and take over the role of the main updraft. The same storm may be multicellular at one time, and supercell (quasi-steady) at another time.

The squall line in contrast has overall motion to the right of the mean winds while individual cells move to the left, right or with the mean tropospheric winds. New cells form on the upwind end of the squall line at 20 to 40 min intervals. The cells on the downwind side are usually oldest and dissipating.

Marwitz (1972) has suggested certain environmental conditions are favorable to the formation of supercell or multicell storms. In his study, both types of storms had severe instability, where parcel theory suggested that the cloud air was about 4°C warmer than the environment at 500 mb. The environmental shear was not severe ($<5 \times 10^{-3} s^{-1}$), for both cases. The main distinguishing feature between supercell and multicell conditions were suggested to be the sub-cloud winds. The supercell winds veered greater than 50° and were greater than 10 m s^{-1}, while the multicell winds were less than 8 m s^{-1} in the sub-cloud layer.

The High-Speed Updraft

The importance of a single large updraft in strongly sheared environmental winds which veer with height has been the subject of a number of studies, for example Newton and Newton (1959). With the exception of the outer turbulent

mixing region, a strong updraft may act as an effective barrier to the environmental flow, as in the hydrodynamic analogy of a cylinder in a uniform flow field. Fig. 1 shows several updraft analogies considered in past literature.

In the classical potential flow around a cylinder in a uniform flow (Fig. 1a), the maximum wind speeds and lowest pressures are found to the left and right of the center of the cylinder (facing downstream), while stagnation points and the highest pressures are found on the upstream and downstream portions of the cylinder. Newton and Newton (1959) proposed a model to explain new cell growth on the right forward flank based on this hydrodynamic analogy in a sheared environment. As a result of the positive and negative pressure perturbations induced on the cylindrical barrier, due to the Bernoulli effect, a vertical pressure gradient results, which was suggested to produce cell growth along the right flank.

The observational results suggest that severe thunderstorms act as barriers to environmental flow. Brown and Crawford (1972) investigate the environmental winds near a thunderstorm with single Doppler data and conclude that the high reflectivity region acts as an obstacle to the environmental airflow. Their results were not as conclusive at higher levels, however. Kraus (1974) inferred from single Doppler data that there is a wake downstream of the updraft and downdraft. Since single Doppler radar

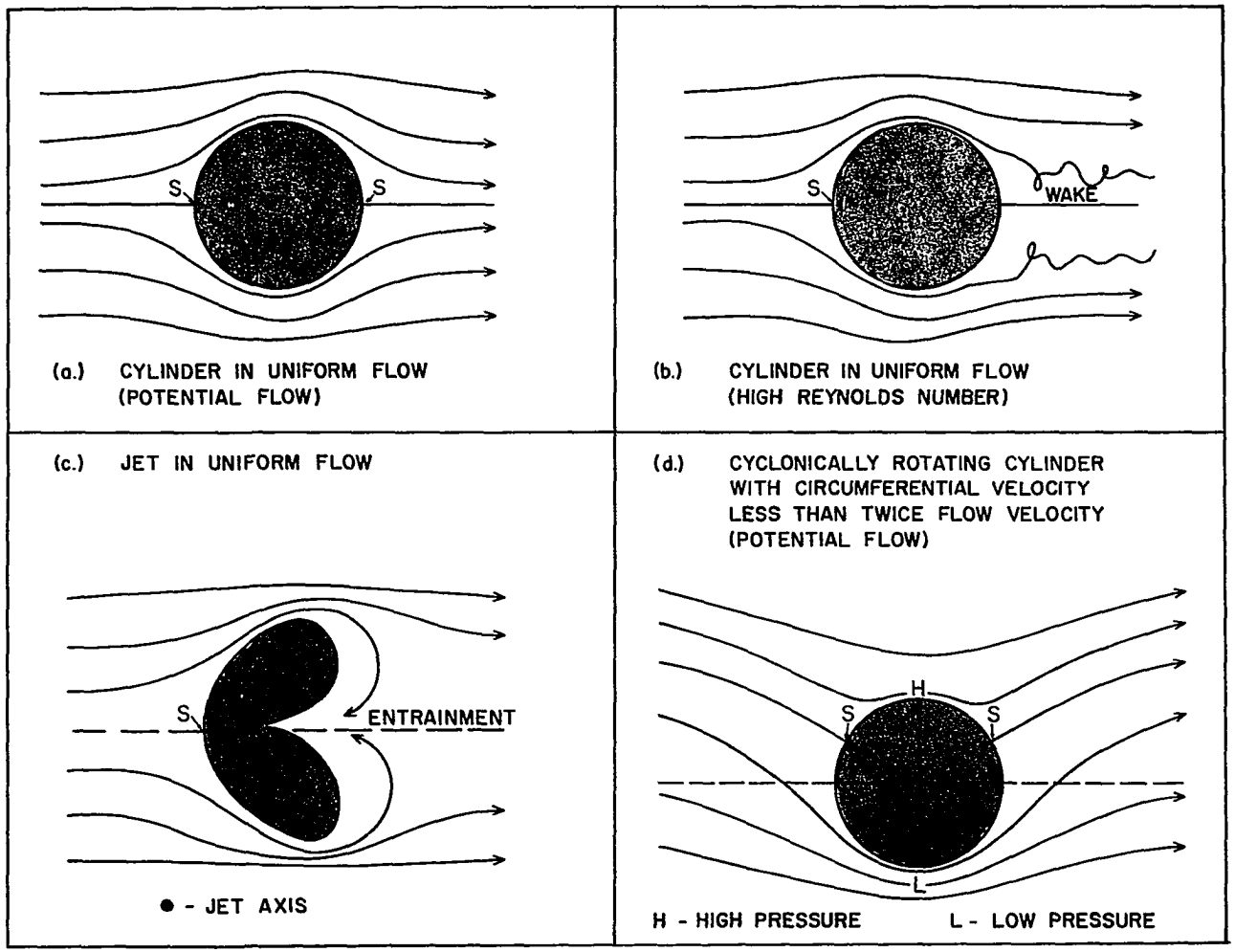

Fig. 1. Updraft flow analogies. The updraft is shaded and S indicates a stagnation point. In (d), the lift force is directed toward the bottom of the figure.

observations were used in these studies, caution must be taken in their interpretation. Fankhauser (1971) investigated the motion of chaff at the 500 mb level around the thunderstorm. Most bundles tended to flow around the storm, but a single bundle was observed to merge with the storm. It was concluded that the storm effectively acted as a barrier to the mid-level flow, although some entrainment occurred. Davies-Jones (1974) concluded from a study of soundings released in updrafts that the updrafts were undiluted by the environment, and the maximum vertical velocity was in mid-levels at approximately 4.8 km.

While these observations support the simple hydrodynamic analogy, one obvious deficiency is separation of flow around the cylinder. The high Reynolds number of storms, approximately 10^4 (see e.g., Jessup, 1972; Danielson, 1975; Connell, 1975), suggests separation of flow to the lee of the cylindrical analogy (Fig. 1b), which weakens the irrotational, non-divergent, inviscid and non-turbulent flow assumptions of potential flow theory. In this regard, Connell has suggested that a jet in a uniform flow field is a more realistic analogy since it acts as a less rigid barrier, and for the Reynolds number concerned, counter rotating vortices with corresponding pressure deficits are formed in the lee of the jet (Fig. 1c). One questionable point concerning this model is that strong entrainment in the downwind portion of the jet is typically observed (Margason,

1969) and observations of severe storms generally do not support this (e.g., Davies-Jones, 1974).

The hydrodynamic analogy of a cylinder in environmental flow has also been used to explain storm deviation (e.g., Goldman, 1966; Charba and Sasaki, 1971; Fujita and Grandoso, 1968). If the cylinder is rotating, as storms are often observed to rotate, the Magnus effect derived from potential flow theory predicts that cyclonically rotating cloud experiences a deflective force at a right angle to the relative wind direction, due to the strong pressure gradient force in this direction (Fig. 1d). A left moving storm, which presumably is rotating anticyclonically, experiences a deflective force to the left of the environmental winds. This offers an explanation for both SR and SL storms.

In summary, the high-speed updraft indeed blocks ambient environmental winds, but the analogy to that of a rotating cylinder has theoretical weaknesses since potential flow theory is used. More recently, the three-dimensional severe storm model by Schlesinger (1975) sheds light on some of these questions. Some of the conclusions from Schlesinger's model are briefly: i) a vortex doublet is present at mid-levels, ii) thermal buoyancy and pressure gradient force are the dominant vertical forces, iii) a storm propagation mechanism is suggested by mid-level horizontal pressure gradient force, iv) it was suggested that

the mid-level vortices were formed by the tilting of vorticity into the vertical, and, v) that Newton and Newton's hypothesis was probably not valid in this case. In view of these results, there is obvious ambiguity of the role of the high-speed updraft in severe storms.

Tornadoes and Tornado Cyclones

The tornado cyclone or parent circulation is a region of strong circulation, generally 5-10 km in diameter, on the same size scale of the radar hook echo (e.g., Fujita, 1963). Several studies were conducted in Oklahoma with single Doppler radar to identify tornado cyclone signature continuity in space and time. Burgess and Brown (1973) and Burgess, et al. (1975) studied the space and time continuity of tornado vortex signatures (TVS) in relation to surface damage tracks of tornadoes. These signatures are identified by an azimuthal shear region having closely spaced isotachs, and a couplet of radial velocity moving toward and away from the radar. The observations generally suggest the presence of a strong circulation, but are limited by the single wind component measured from one radar.

Tornadoes are found under a variety of conditions and are a few hundred meters in diameter. The detection of a tornado is presently somewhat difficult. With the combined Rankine vortex assumption, it is possible however to estimate tornadic wind speeds from Doppler velocity spectra

(Zrnic and Doviak, 1975). Two favored locations for tornadoes from visual and radar observations have been suggested in previous literature. They may form along the flanking line, possibly in association with the gust front, or in the vicinity of the tornado cyclone circulation.

The genesis mechanisms for tornadoes is not well understood, although a number of theories have been proposed. A few consider an application of the vorticity equation to determine the vorticity production mechanisms which generate the large vorticities required for tornado genesis. Barnes (1970) gives a possible explanation of updraft rotation and tornado genesis by the tilting term in the vorticity equation, a result of the large frictionally and thermally induced vertical wind shear in the low-level moist air. Vorticity is stretched and concentrated by updrafts along the storm's flank and subsequently merged into the main updraft. Smaller vortices may then form around the main rotating updraft. Gray (1969) gives another mechanism for tornado genesis in which the vorticity source is hypothesized to be the result of barrier flow associated with an updraft in a strongly sheared environment. A cyclonic circulation along the right front flank of the storm, combined with simultaneous intense cumulus scale convergence produce vorticity through the divergence term in the vorticity equation. It is interesting to note that in Schlesinger's model, the results suggested the im-

portance of the tilting term rather than the divergence term in the vorticity equation.

Other theories consider frictional convergence an important mechanism for vorticity generation. Maddox and Gray (1973) propose that once a vortex is formed along the gust front, intensification may result from frictional convergence toward its center. Other theories have been proposed, however, the sources are clearly not well understood.

Objectives

Previous work done on severe thunderstorms indicates that although many observations were obtained, they are still insufficient to make definitive comparisons with theories on storm deviation and the genesis and demise of tornadoes. Even with the impressive tools available today, the tornado scale (.5 km) wind observations are still smaller than our sampling capability. The proposed work attempts to make a detailed study of dual Doppler velocity and reflectivity observations from a severe thunderstorm on June 8, 1974, and to relate these to previous observations and speculative theories. Of particular interest in this study are the simple dynamical implications of some of the kinematical properties in relation to storm structure. Up to this point, it is still not clear where the large sources of vorticity required for tornado genesis originate;

whether it is due to blocking flow at mid-levels, or vertical shear of the horizontal winds in the lower troposphere, or other mechanisms. An evaluation of the vorticity equation terms shed light on theories such as proposed by Barnes (1970) and Gray (1969). The main emphasis will be on lower storm levels (less than approximately 6 km altitude), particularly in the region of the gust front, tornado cyclone and updraft-downdraft couplet.

The research is a diagnostic study of kinematic fields. The objective analysis for radar data previously developed (Heymsfield, 1976) is extended to compute vertical velocities. Vertical and horizontal cross-sections are constructed in order to locate key storm features, on scales larger than the tornado scale. The divergence and vorticity are computed, and subsequently related to the storm features. The tilting and divergence terms of the vorticity equation are evaluated and then related to previous storm structure findings. The results will also provide insight into some of the magnitudes of parameters for numerical modeling. An important part of the research is a synthesis of data to verify that the computed quantities are meaningful.

Doppler Observations and Support Data

On June 8, 1974, data were collected jointly by the National Severe Storms Laboratory (NSSL) and the University

of Oklahoma. The primary data source was from the two NSSL Doppler radars located at Norman (NRO), Oklahoma, and Cimarron (CMF), Oklahoma. The radars are separated by 41.4 km, along a 309.9° - 51.1° radial. Other support data included NSSL WSR-57 digitized radar reflectivity data, NSSL rawinsondes released from Norman, and aircraft observations. The University of Wyoming aircraft collected thermodynamic and wind data, and also dispersed chaff (McCarthy, et al., 1974, 1975) to enhance the radar detectability of the weak echo region (WER).

Doppler observations for this study were four tilt sequences from each radar, centered in time at 1545, 1555, 1605 and 1613 CST. The azimuth and elevation angle increments were 1°, the gate spacing was 0.6 km. The lowest tilt was 0.2°, stepped up to 8° or 9°. The resulting density of observations were in the approximate range of 1 to 10 per cubic kilometer. The characteristics of the two radars are given in Table 1.

A brief review of the Doppler terminology is given to facilitate later usage. The Doppler spectrum, S(f), gives the frequency spectrum of backscattered power from the precipitation targets in the radar pulse volume, moving in a direction radial from the radar. The Doppler velocity spectrum is related to the Doppler spectrum by $v = \lambda f/2$, where λ is wavelength of the radar. The total average power received by the radar, P_r, is defined according to $\int_{-\infty}^{\infty} S(v)\,dv$.

TABLE 1

CHARACTERISTICS OF DOPPLER RADARS ON JUNE 8, 1974

	NORMAN (NRO)	CIMARRON (CMF)
Wavelength	10.52 cm	10.94 cm
Peak Power	750 KW	500 KW
Pulse Length	1 μsec (150 m)	1 μsec (150 m)
Half-Power Beam Width	0.81°	0.81° (estimated)
Nyquist Velocity Cointerval	±34.2 m sec^{-1}	±35.6 m sec^{-1}
Pulse Repetition Time (PRT)	768 μsec	768 μsec
Antenna Gain (includes waveguide and radome transmission loss)	44.8 dB	43.2 dB

The mean Doppler velocity and variance of the Doppler spectrum are given by

$$v_r = \int_{-\infty}^{\infty} v\, S(v)\,dv \;/\; \int_{-\infty}^{+\infty} S(v)\,dv$$
$$\sigma^2 = \int_{-\infty}^{\infty} (v-v_r)^2\, S(v)\,dv \;/\; \int_{-\infty}^{+\infty} S(v)\,dv \quad , \qquad (1)$$

where targets moving at velocity v in the radial direction are weighted according to the backscattered power of these targets. The mean Doppler velocity is the mean of S(v), while the variance gives the dispersion of radial velocities of the targets. The geometry of the wind components contributing to the radial velocity measurement at a radar range gate is shown in Fig. 2. The radial velocity may be given according to the Cartesian components (X, Y, Z; U, V, W) and mean particle fallspeed, v_T, by the relation

$$v_r = U \sin\beta \cos\theta + V \cos\beta \cos\theta + (W + v_T) \sin\theta, \qquad (2)$$

where v_T is the mean terminal fall velocity of precipitation targets in the radar volume, and R, β, and θ are the range, azimuth, and elevation angle of the radar volume. The last term gives the contribution from the mean vertical motion of the precipitation particles, and can amount to several meters per second for elevation angles less than 10°.

Measurements of mean Doppler velocity, variance of the Doppler spectrum, and reflectivity were obtained from the radars in routine processing by NSSL. The Doppler velocity measurements were carefully edited on the computer.

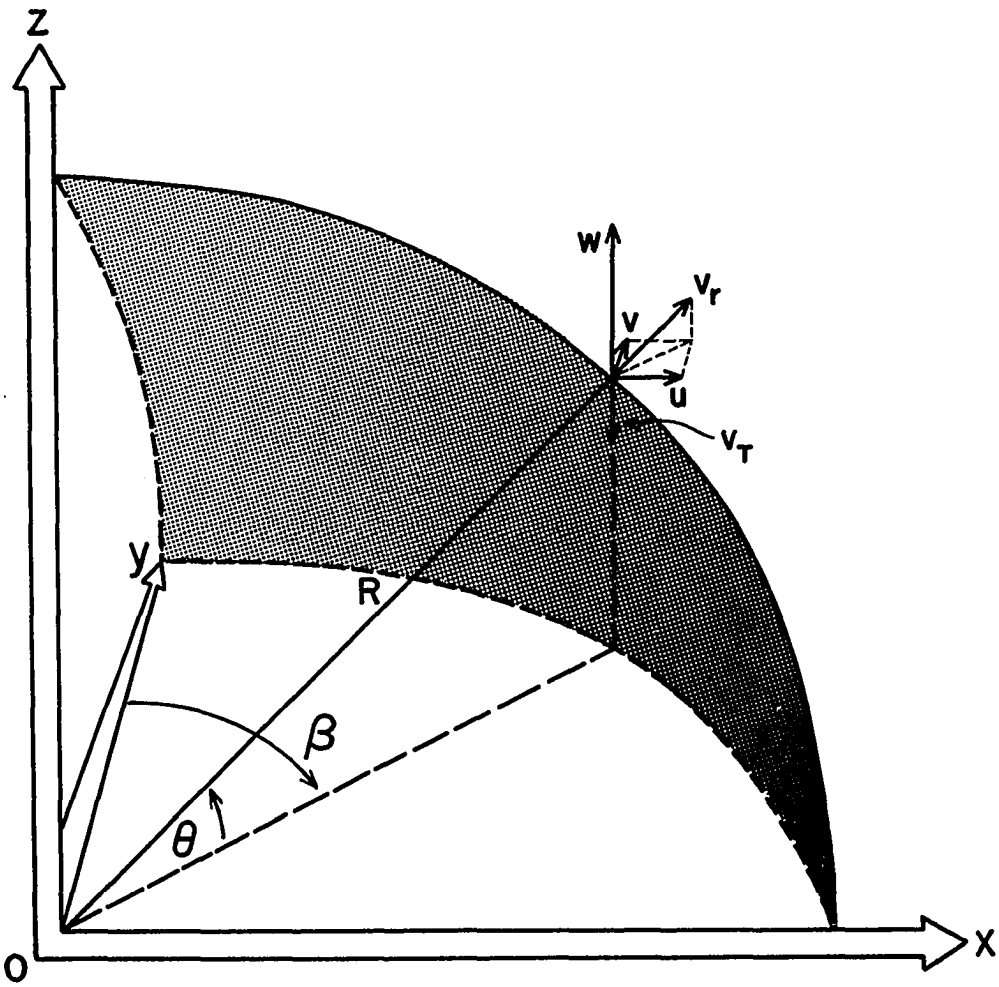

Fig. 2. Velocity components contributing to Doppler radial velocity at one range gate.

Folding of the Doppler spectrum was corrected, and spectra from regions of weak radar returns were eliminated. Doppler spectrum folding occurs when the precipitation targets have radial velocity magnitudes larger than the Nyquist velocity. It is evident in a data field when gradients between successive range gates (or, between range gates in adjacent radials) are approximately twice the Nyquist velocity. By checking these gradients, range gate radial velocities were re-folded. Errors arise in the radial velocities when the radar returns are weak. Data were thus eliminated when power was below a signal-to-noise ratio of 6dB and 3dB for the Norman and Cimarron radars, respectively. Doppler velocities with Doppler standard deviations larger than about 10 m s^{-1} were also eliminated, as they may have resulted from an error in the analog to digital conversion in the radar processing. Other systematic errors such as radar position coordinates were not corrected or known. As will be seen later, it was necessary to correct for these systematic observation errors prior to objective analysis.

CHAPTER II

METEOROLOGICAL CONDITIONS ON JUNE 8, 1974

Synoptic and Subsynoptic

On June 8, 1974, a number of severe storms occurred in Oklahoma. Twenty tornadoes were reported, and the property damage was estimated in the millions of dollars. The upper level support for this system was a major long wave trough situated over the mountain states, with diffluence occurring over Oklahoma during the afternoon. At 1800[4] the 500 mb jet had winds in excess of 50 kt. Fig. 3 shows the NMC surface analysis from Tidwell (1975). Discontinuous retrogression occurred on June 7, and by 0000 cyclogenesis was occurring east of the Sacramento mountain range in New Mexico (Fig. 3a). After 0600 (Fig. 3b) the low intensified and moved into western Kansas, where a classical occlusion of the front began. The warm front passing through Oklahoma during early morning hours produced severe storms which dissipated shortly afterwards. The cold front at 1500 (Fig. 3c), which extended from western Oklahoma through southern New

[4]All times throughout this and later sections are given in CST. All heights are given above the surface (unless otherwise indicated), which is approximately 360 m above Mean Sea Level (MSL).

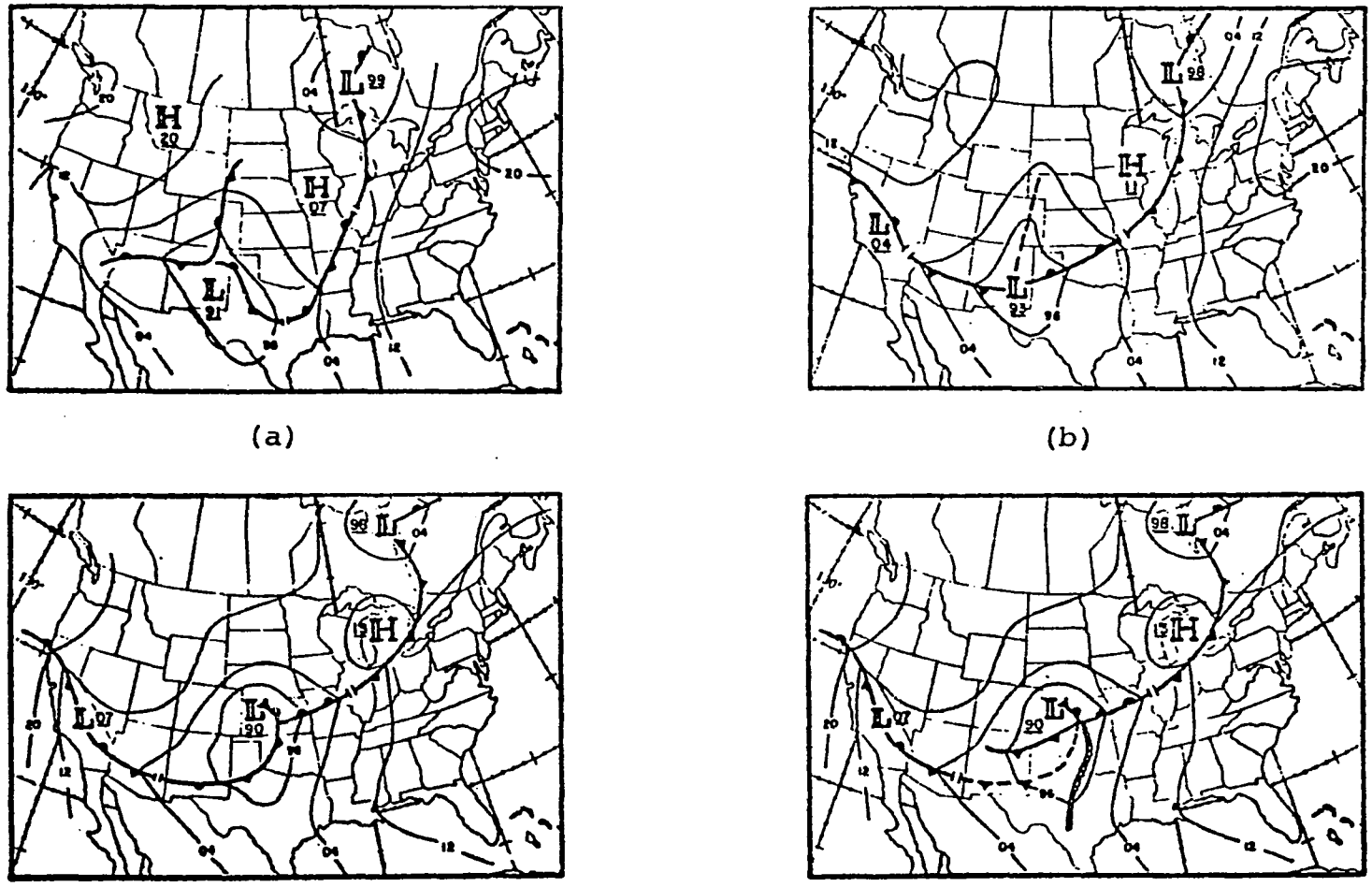

Fig. 3. NMC's surface analysis charts for (a) 0000, (b) 0600, and (c) 1500. (d), 1500 hand analyzed using Tegtmeier's SSL-DLW complex model (from Tidwell, 1975).

Mexico, was analyzed according to the Tegtmeier (1974) model (Fig. 3d). The subsynoptic condition which helped trigger thunderstorms during the afternoon was a dry-line wave, subsynoptic low complex. The dry-line existed through central Oklahoma and a cold front was present in northern New Mexico. The bulge in the dry-line was centered west of Oklahoma City (OKC), with a region of strong moisture convergence southwest of Oklahoma City.

Radar Observations-Overview

The organization of the severe storms present during the afternoon on June 8 was quite complex. The most extensive studies were performed in the northeast quadrant from OKC, from 1545 to 1613. Isolated storms began southwest of OKC with movement toward approximately 50°. After about 1700 a squall line existed with a 40°-220° orientation. Fig. 4 presents a sequence of low-level WSR-57 reflectivity radar observations from 1530 to 1630.[5] The figure is a space-time representation, i.e., the grid for each analysis time is spaced along the horizontal axis according to time. The approximate locations of storm A, or the Harrah storm, and storm B are indicated in Fig. 4. WER associated with these storms are seen along the southern boundary of the echo.

[5]The objective technique for obtaining WSR-57 data on horizontal planes was developed by S. P. Nelson of NSSL. Throughout this and later sections, reflectivity is expressed in units of dBZ according to 10 log Z_e, where Z_e is effective reflectivity factor in $mm^{-6}m^{-3}$.

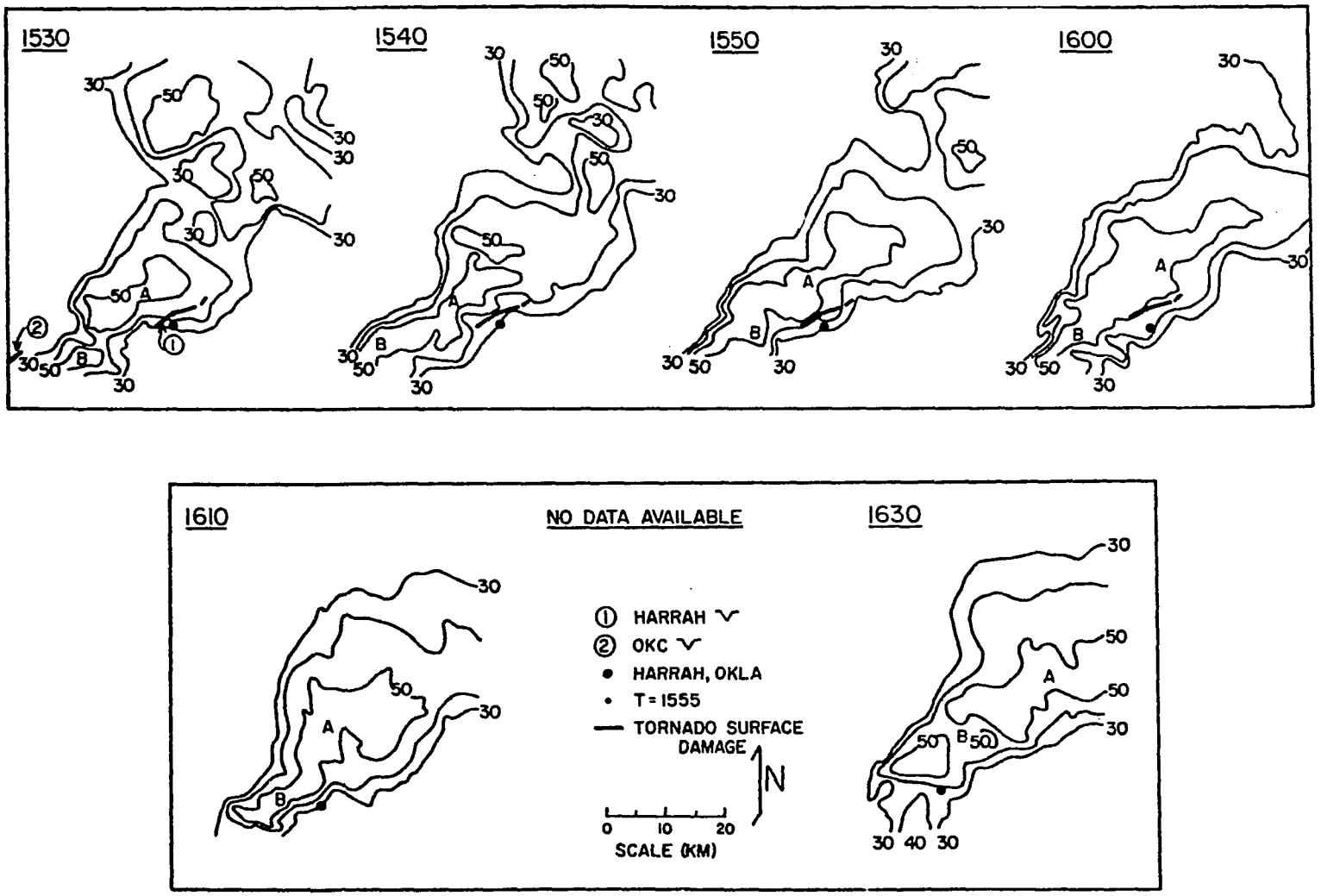

Fig. 4. Objectively analyzed 1.5 km reflectivity fields from WSR-57 radar. Contours are given in 10 dBZ intervals.

Two more storm systems are located approximately 30 km to the north and northeast of storm A. These are not labeled since they are out of the dual Doppler analysis domain. Storm B consists of two cells, as will become evident later, spaced approximately 10 km apart. The radar tops of storms A and B (i.e., when high enough radar scans were collected) were approximately 15.5 km.

Two tornadoes occurred between 1530 and 1630 in the analysis region. Fig. 4 indicates the surface damage tracks of the OKC tornado and the Harrah tornado by thick line segments. The 1505 time given for the OKC tornado is only approximate, while the Harrah tornado passes the Harrah power station at 1555, and is indicated by a small dot.[6] The OKC tornado did moderate damage to a few buildings, while the Harrah tornado destroyed or damaged several farm buildings. There were no reports of hail damage associated with storms A and B.

A sequence of .2° elevation angle radar scans of reflectivity from the Cimarron Doppler radar are shown in Fig. 5A-J. Storm A and storm B developed hook echoes. The hook echo associated with storm A (Fig. 5B to Fig. 5G) was first evident at about 1536, began to wrap up

---

[6]These were determined from an aerial survey conducted by NSSL and OU personnel. Two tornadoes at about 1350 and 1505 occurred in OKC on June 8. The 1505 tornado has an inaccurate time since it was incorrectly reported as 1535, and later inferred by NSSL personnel as 1505.

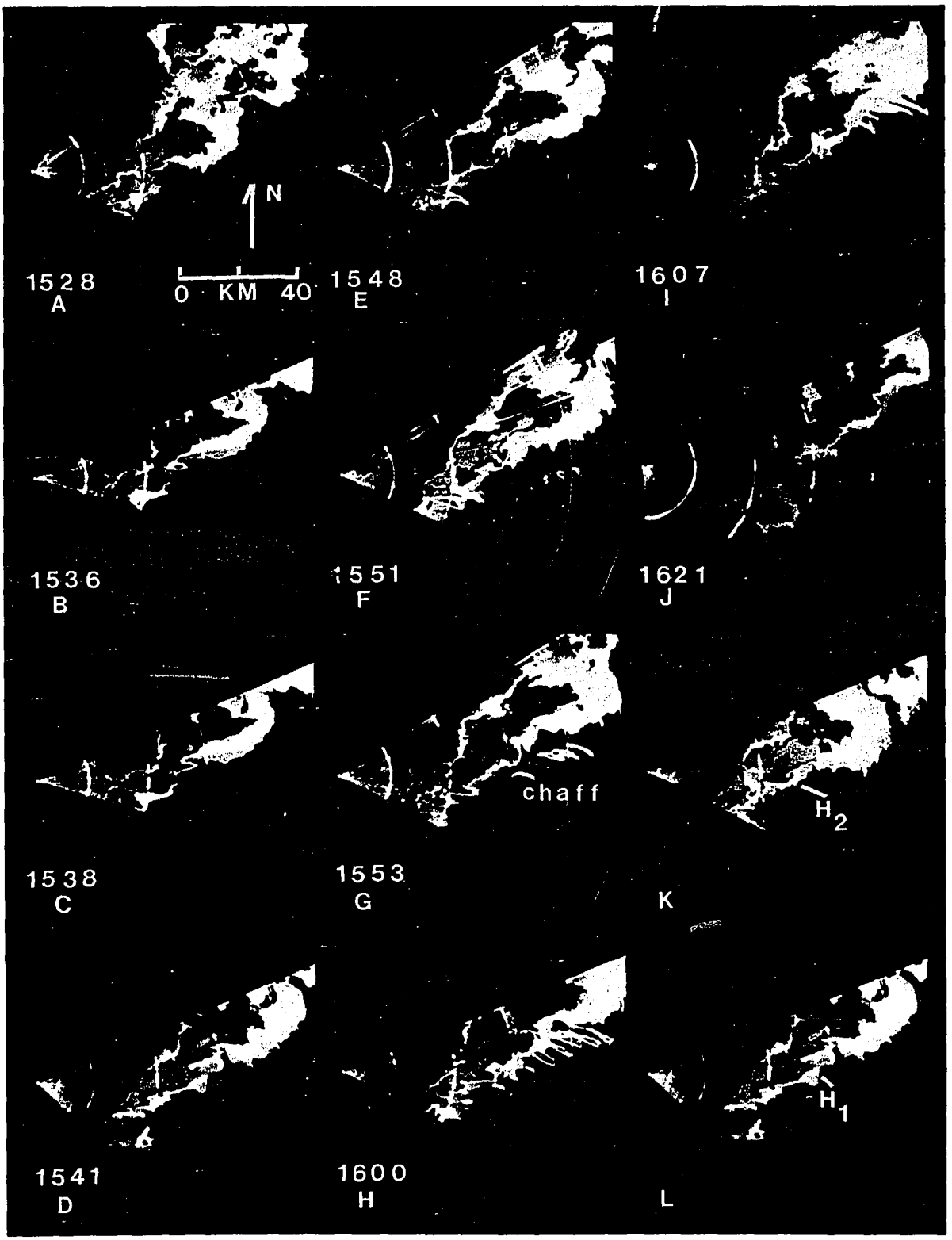

Fig. 5. Intensity-contoured display of Cimarron Doppler radar azimuthal scans for: 0.2° and 1° elevation angle (A-J) from 1528 to 1621; (K) 5° elevation angle at 1543; (L) 1° elevation angle at 1541. Chaff is seen to the south of the storms in F to I. H_1 is the main hook echo; H_2 is a feature possibly associated with the tornado and new cell growth.

by 1539, and by 1557 filled in. It should be noted that chaff were dispersed along a northeast-southwest line at about 1540 (see McCarthy et al. 1974) and is observed to cyclonically flow into storm A (Fig. 5F to Fig. 5I). Storm B had a hook echo by 1548 which lasted beyond 1621. Both had a duration of about 20-25 min, and storm A occurred too late to be associated with the OKC tornado. Storm A is studied in most detail in later analysis of the kinematic and reflectivity fields.

Storm Environment

The environmental conditions for storm A are discussed in this section, and then related to previous storm environment criteria. The soundings representative of the storm environment were released from Norman (NRO); they were located to the south-southwest of most storm development. Six soundings were released at approximately 2 h intervals, beginning at 1115, 5 either entered clouds or did not reach high altitudes. The 1115 sounding in Fig. 6a was 4.5 h before the first analysis time, and will be used since it was the only one to reach the tropopause.[7] The sounding released at 1710 (Fig. 7a) shows the changes in the environment due to movement of the 500 mb trough. In Fig. 6b and Fig. 7b, the wet bulb potential temperature, θ_w, and saturation wet bulb potential temperature,

[7]The rawinsonde data were plotted using the routine developed by Davies-Jones and Henderson of NSSL.

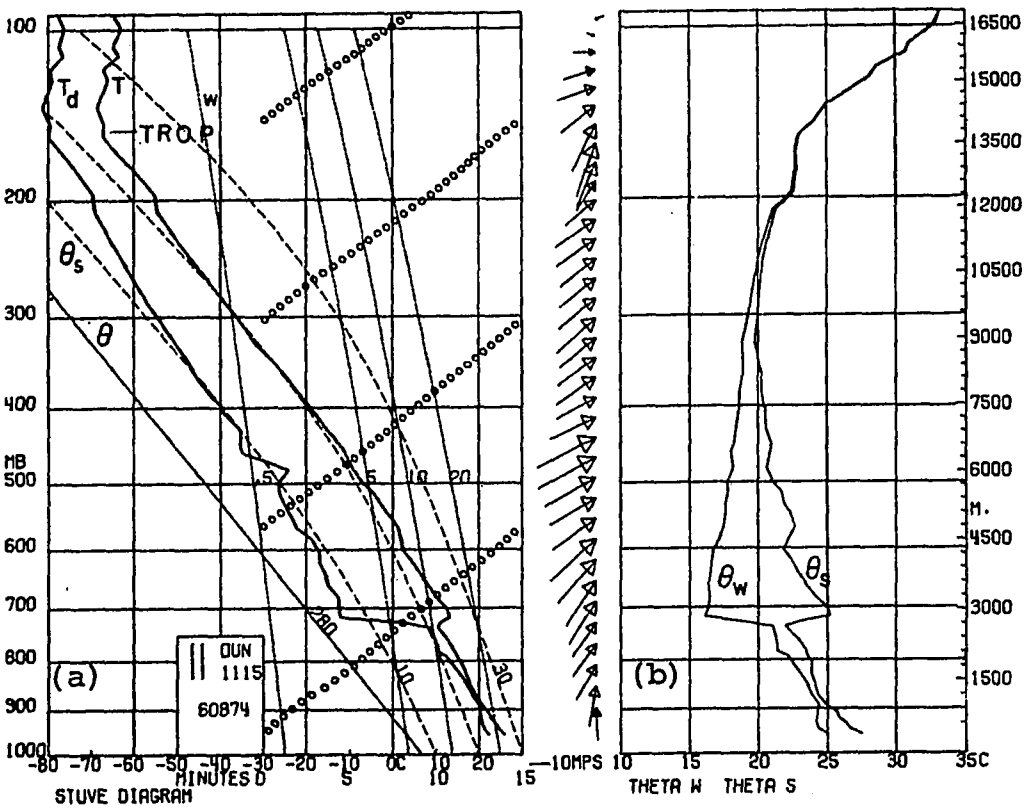

Fig. 6. NRO sounding for June 8, 1974, at 1115: (a) Stüve diagram; (b) θ_w and θ_s profiles. Heights given above MSL.

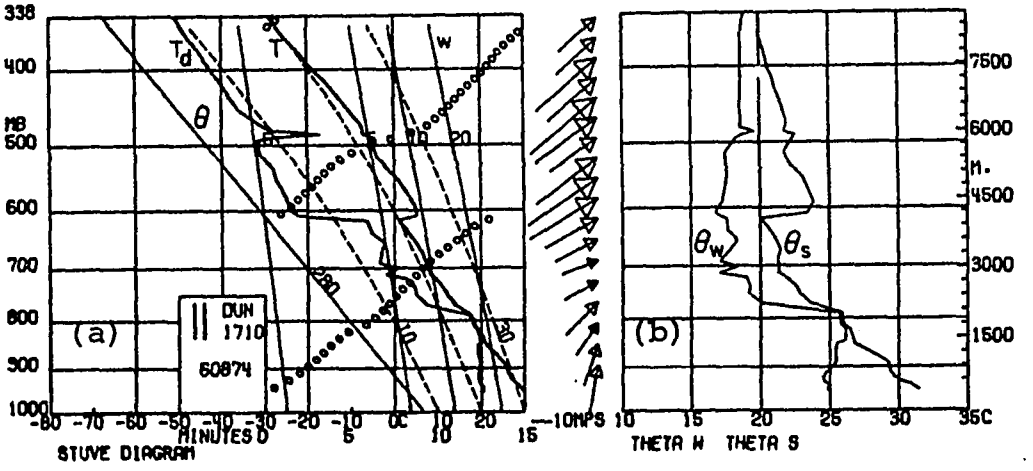

Fig. 7. Same as Fig. 6 except at 1710.

θ_s, are shown. θ_w is a conservative property with respect to condensation and evaporation processes. θ_s is θ_w with 100% saturation. The heights are given above MSL in these soundings.

The 1115 sounding indicates the atmosphere is potentially ($\partial\theta_w/\partial z < 0$) and conditionally ($\partial\theta_s/\partial z < 0$) unstable at lower levels. Dry mid-level air existed above a moist low-level stratum 2-3 km thick, which is extremely favorable for strong convection and is a typical Type 1 sounding (Fawbush and Miller, 1954). The 0°C level was located at about 4 to 4.5 km, and the tropopause is located at about 13.8 km. The θ_w minimum of 16°C occurs at approximately 3 km, decreasing from a surface value of 25°C. The temperature excess at 500 mb was 8°C.

The one-dimensional cloud model discussed by Davies-Jones (1974) was applied to this sounding to obtain an upper limit on the vertical motion field. The level of free convection (LFC) for the 1115 sounding was 1050 m, and the lifting condensation level (LCL) was 850 m. The model coefficients were adjusted so that entrainment and water loading were neglected (essentially the parcel method). Assuming a vertical velocity of 2.5 m s^{-1} at the LFC, the vertical motion is 7.09 m s^{-1} at 1.5 km, 23.7 m s^{-1} at 4.5 km, and 32.55 m s^{-1} at 6.3 km.

Wind hodographs for June 8, 1974 are shown in Fig. 8 and Fig. 9. The winds have been averaged at 1 km inter-

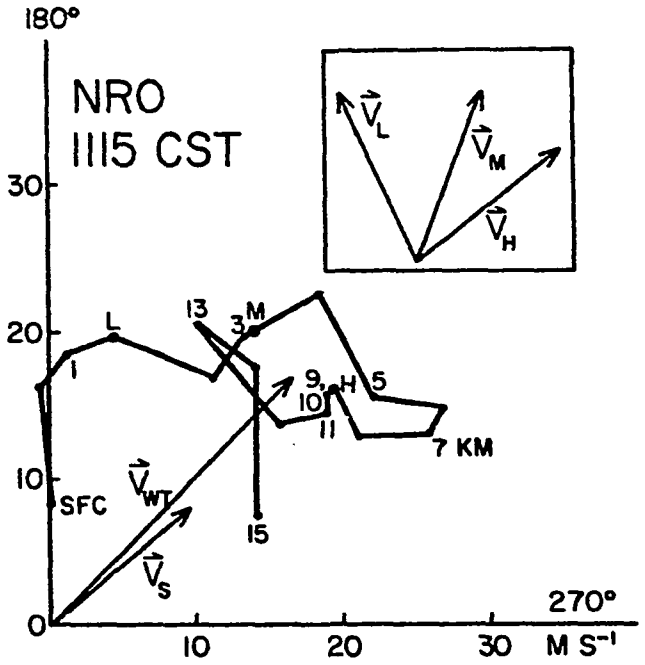

Fig. 8. NRO wind hodograph at 1115. Heights are given in kilometers above MSL. Insert gives winds relative to storm A for L(850 mb), M(700 mb), and H(300 mb).

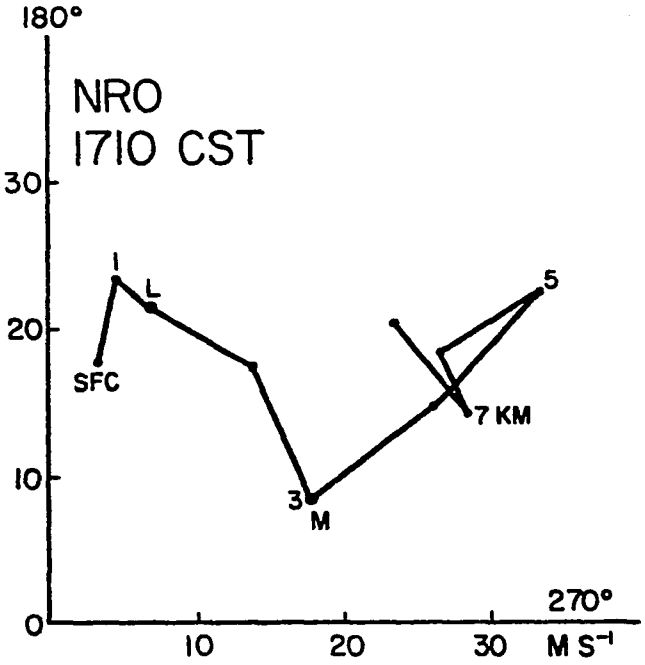

Fig. 9. Similar to Fig. 8 except at 1710.

vals over 50 mb layers. The environmental wind structure at 1115 is typical for severe storm development; i.e., low-level southerly moist flow and southwesterly flow of drier mid-level air. At low-levels, less than approximately 3 km altitude, the directional shear is quite strong (35° at 1115, and 60° at 1710). The low-level winds are greater than 9 m s^{-1}. Vertical shears computed from the environmental winds were about $2 \times 10^{-3} s^{-1}$ between 3 and 10.5 km; however, the Doppler observations discussed below suggest vertical shears of approximately $5 \times 10^{-3} s^{-1}$ along the right flank of storm A.

The vertical environmental wind structure changes during the day as a result of the southeasterly movement and intensification of the 500 mb trough, and the movement of the surface low (Fig. 3). The 1115 and 1710 mid-level shear patterns are similar to those found by Henderson (1974) on April 29, 1970, and are not typical of a Great Plains thunderstorm (e.g., Browning, 1965; Fankhauser, 1971) in which winds do not back with height. Differences in these soundings are perhaps associated with the changes in the storm system on June 8 from isolated cells beginning at 1200 to a squall line forming at about 1700.

For subsequent computations the 1115 sounding is used. This sounding seems reasonable when compared with aircraft winds representative of the environment. The aircraft winds at approximately 1600 were subjectively averaged

at two flight levels: 28.3 m s^{-1} from 216° at 3.35 km and 24.7 m s^{-1} from 190° at 1.35 km. The 1115 sounding results were reasonably close in comparison: 25.6 m s^{-1} from 213.7° and 20.2 m s^{-1} from 191.6°, respectively.

The mean-weighted tropospheric wind $\vec{V}_{WT}$ is important in determining the movement of individual cells with respect to the mean winds. $\vec{V}_{WT}$ was determined from a mass-weighted value computed according to

$$\vec{V}_{WT} = \int_{z_0}^{z_m} \rho\vec{V}dz \; / \int_{z_0}^{z_m} \rho dz, \qquad (2)$$

where z_0 and z_m are cloud base (approximately 1 km) and the tropopause (13.8 km), respectively. The $\vec{V}_{WT}$ determined according to (2) was 23.7 m s^{-1} from 225.5°.

All relative winds are henceforth given relative to the main updraft of storm A. Storm relative winds are given by $\vec{V}_r = \vec{V} - \vec{V}_s$, where $\vec{V}_s$ is storm motion, and $\vec{V}$ was determined from analysis of the translational movement of the WER and hook echo of storm A, using low-level reflectivity fields. Over about a 30 min time interval, $\vec{V}_s$ was approximately 12 m s^{-1} from 230.3°. Inserted on Fig. 8 are environmental winds relative to storm A for 850 mb ($\vec{V}_L$), 700 mb ($\vec{V}_M$), and 300 mb ($\vec{V}_H$). These winds are similar to those in the Browning (1965) study of supercell storms. The low-level, high θ_w, air typically flows toward the right front flank, while the lowest θ_w mid-level air is directed toward the right flank. The maximum $\vec{V}_r$ was 21.6

m s^{-1} from 251° at 6.5 km. According to the 1115 sounding, storm A moves only 5° to the right, and 13.6 m s^{-1} slower than the mean tropospheric wind. This storm motion deviation may be slightly larger if it is taken into account that the mid-level winds backed slightly after 1115.

The environmental conditions present on June 8 (i.e., strong sub-cloud winds, strong potential instability, strong wind veer with height, strong vertical shear of the horizontal environmental winds) are generally within the range of values suggested by Marwitz (1972) for a supercell storm. The classification of the June 8 storm, however, is somewhat ambiguous as will become evident later.

CHAPTER III

COMPUTATION OF THREE-DIMENSIONAL WINDS FROM RADAR DATA

Wind field computations from two Doppler radars involve considerable processing of the vast quantity of data obtained. A single Doppler radar gate samples velocity and reflectivity data over spherical surfaces (Fig. 2), which must subsequently be interpolated to Cartesian coordinates for meteorological interpretation.[8] It is important for these analyzed fields of radial velocity to be error-free, since derivatives in subsequent kinematic computations are sensitive to errors in the initial velocity fields. The statistical objective analysis scheme we use to interpolate the observations to grid-points, minimizes the mean square error of the difference between true grid-point value and the interpolated grid-point value given by a linear sum of the observations. Smoothing of random observational errors is achieved by this technique and data weights are determined according to the statistical structure.

---

[8]Cartesian coordinates are henceforth defined according to the tangent plane assumption. For regions of most interest in the analysis, z = 0 km would be less than 250 m above the surface.

Fig. 11 gives a block diagram which utilizes two techniques for determining the three-dimensional wind field: i) a statistical interpolation scheme for radial velocity observations, and ii) use of continuity equation in cylindrical coordinates (Armijo, 1969) for computation of vertical wind. To avoid confusion, the meteorological Cartesian coordinates are given by (U,V,w;X,Y,z), the rotated Cartesian and cylindrical coordinates (Fig. 10) are given by (x,y,z;u,v,w) and $(r,s,\alpha;u_r,u_s,u_\alpha)$, respectively; (x',y',z) define a coordinate system with the x' direction parallel to the radar radial passing through the center of the analysis grid. The origin for these coordinate systems is at the Norman radar. To reduce computation time, edited, space-time adjusted range gate values of radial air motion from each radar are interpolated to both Cartesian and cylindrical coordinates. The interpolated values of radial air motions from each radar are then combined in both coordinate systems to give u_r and u_s winds. The vertical wind component is found in cylindrical coordinates from integration of the continuity equation. The u,v,w winds on horizontal planes, which are desired in later meteorological analysis, are found from u_r and u_s on Cartesian coordinates using an interpolated w component from cylindrical coordinates. The assumptions involved in the above are discussed in following sections. The CMF reflectivity observations were interpolated only to the Cartesian frame, for which discussion is omitted.

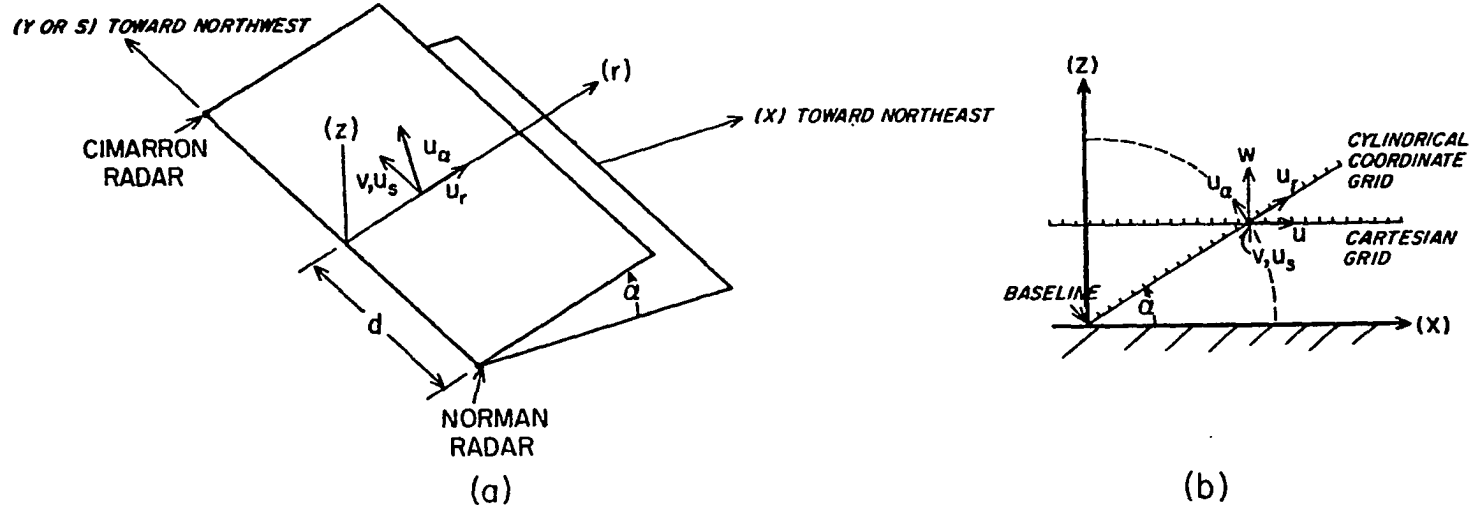

Fig. 10. Geometry of wind computations: a) cylindrical geometry, and b) a vertical (z-x) cross-section showing cylindrical and Cartesian grids.

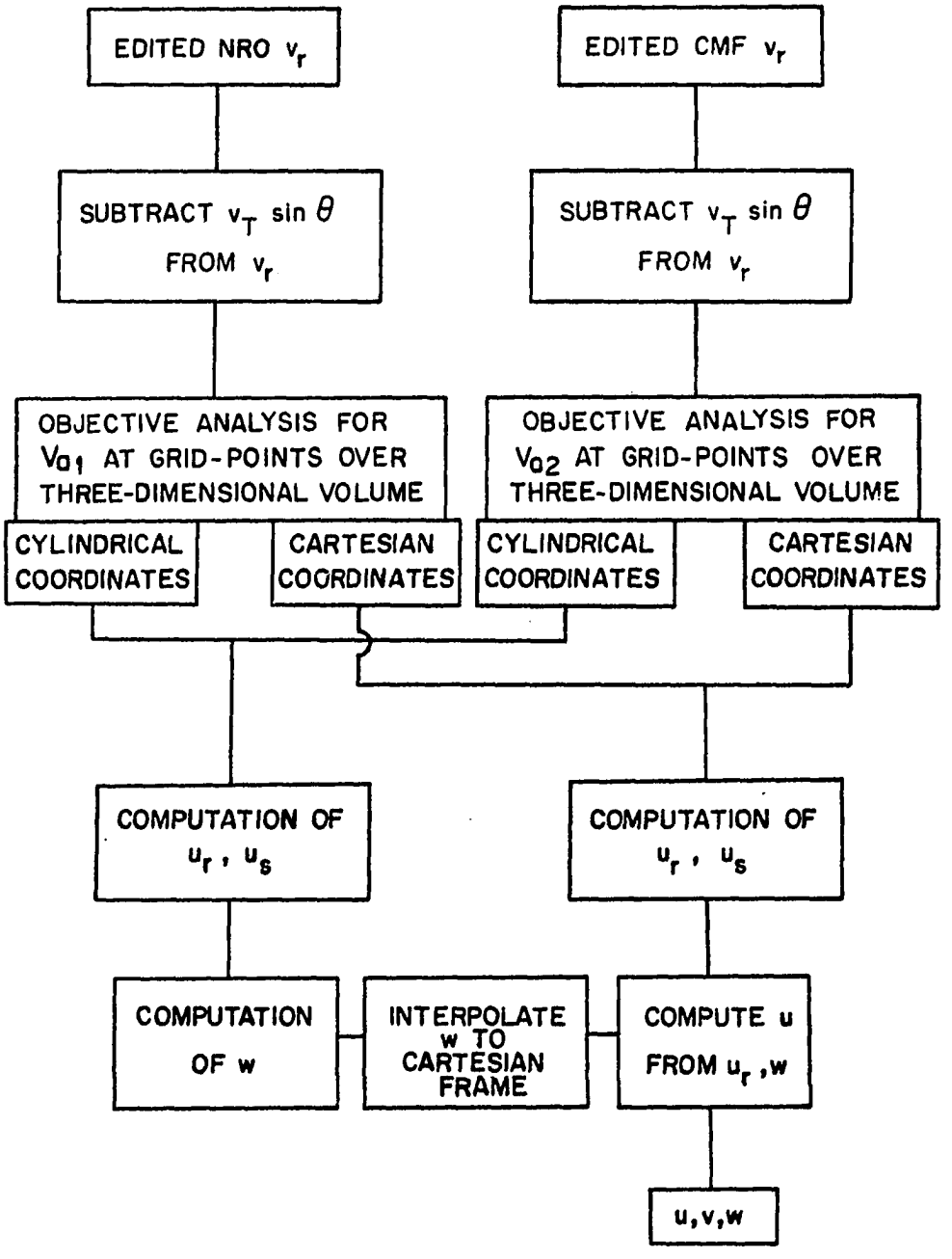

Fig. 11. Flow diagram of computation of three-dimensional winds.

Interpolation of Doppler Radial Velocities to Grid-Points

Consider random and systematic errors in the measured radial velocities which are used in the computations. Random errors prior to interpolation may arise from the variance of the Doppler velocity estimate, from turbulent air motions on scales larger than the radar pulse volume, and from instrument noise. The variance of the mean spectral estimate depends on factors such as spectral broadening due to turbulence on scales smaller than the pulse volume, and wind shears. According to Doviak et al. (1976a,b), 95% of spectrum widths were less than about 10 m s^{-1} for an earlier time on June 8, 1974. This would correspond to an error in the mean spectral estimate of about 1.23 m s^{-1}. According to Heymsfield (1976), the total random error in radial velocity averaged over 4 analysis times and separate storm regions is about 2.3 m s^{-1}. This would suggest that turbulence on scales larger than the pulse volume, and instrument noise contribute to the random errors in the radial velocity estimate. Systematic errors arise from the long data collection interval (approximately 5 min), and the requirement to analyze this data at one time.

Weighting schemes for data interpolation have been designed in a number of different ways, but generally the weight function is prescribed a priori, or it is computed from the data aposteriori. The statistical optimal interpolation for scalar fields (Gandin, 1963; Eddy, 1963, 1973)

is an example of the latter, since it employs an auto-correlation function determined from observations to assign weights to data. This scheme is employed and discussed in more detail in Heymsfield (1976). There are several assumptions in using the statistical objective analysis: i) over small three-dimensional regions, systematic trends are neglected; ii) only random errors in the data as previously discussed are considered; iii) the "frozen turbulence hypothesis"; iv) homogeneity; v) the density variation is assumed a function of height, z; vi) all precipitation is liquid such that an estimate of the mean fallspeed can be obtained from the radar reflectivity factor. These assumptions are discussed below.

In computing air motions from Doppler radial velocities, the assumption is made that precipitation falls relative to the air at its terminal velocity, and shares the horizontal air motion. The validity of this assumption decreases with increasing size of precipitation particles; however for large raindrops it is a reasonable assumption (see Kessler, 1969, Appendix A). The observed radial air motion v_a' for a range gate represents a pulse volume average, and is defined according to the observed radial velocity of precipitation v_r' by the relation

$$v_a'(R,\beta,\theta) = v_r'(R,\beta,\theta) - v_T' \sin\theta, \qquad (3)$$

where the prime indicates measured quantities. An estimate

of mean fallspeed (assumption (vi)) is given by Joss and Waldvogel (1970) by the relation (also see Fig. 12)

$$v_T' = -2.65 Z_e^{.114} \left[\frac{\rho_0}{\rho}\right]^{0.4} , \qquad (4)$$

where Z_e is in $mm^6 m^{-3}$, ρ_0 is surface mass density, $\rho(z)$ is the mass density at a particular altitude, and v_T' is in $m\ s^{-1}$. The correction factor for density variation with altitude on the right side of (4) from Foote and duToit (1969) is shown in Fig. 13.

Gunn and Kinzer (1949) and other empirical studies of raindrop fallspeeds indicate that v_T has a maximum value of approximately 10 $m\ s^{-1}$ at 1013 mb. From (4), fallspeeds greater than 10 $m\ s^{-1}$ are implied from the data at 1013 mb. Thus, it is assumed that the maximum v_T is 10 $m\ s^{-1}$ at 1013 mb. It is mentioned that (4) applies for liquid precipitation and if hail with an approximate v_T range of 5 to 40 $m\ s^{-1}$ were present, (3) would be underestimated. The June 8, 1974, reflectivities were greater than 50 dBZ, suggesting the presence of hail. Due to the lack of better understanding of the precipitation types present in different locations in the storm (e.g., graupel, hail, raindrops, etc.), (4) was assumed.

The density variation is assumed a function of height in subsequent computations. Three forms of density variation with height were considered and shown in Fig. 13: a) constant lapse rate atmosphere, b) an empirical profile deduced from Darkow's (1969) tornado proximity soundings,

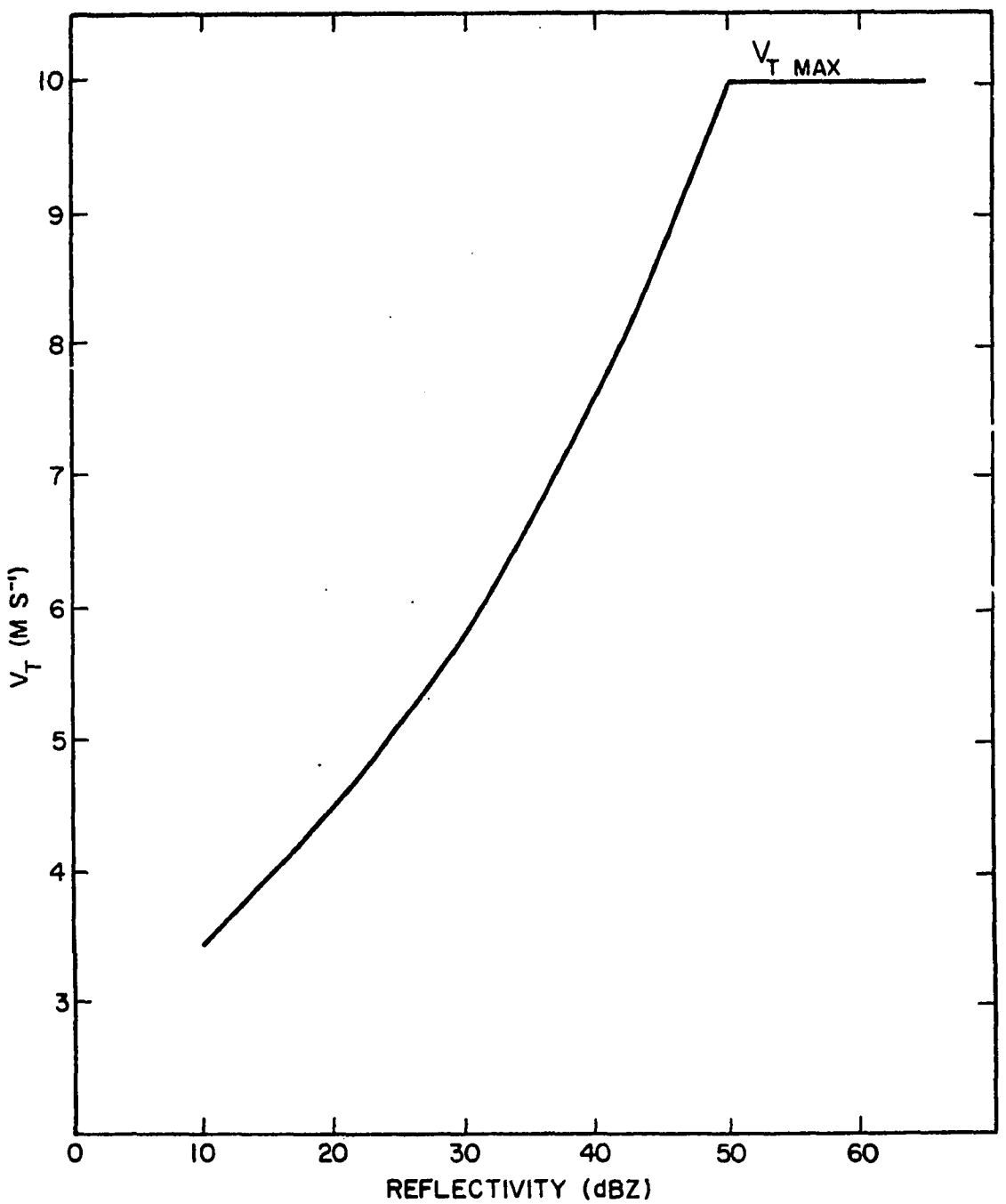

Fig. 12. Terminal velocity relation for liquid precipitation at 1013 mb. The upper limit of v_T = 10 m s^{-1} is shown.

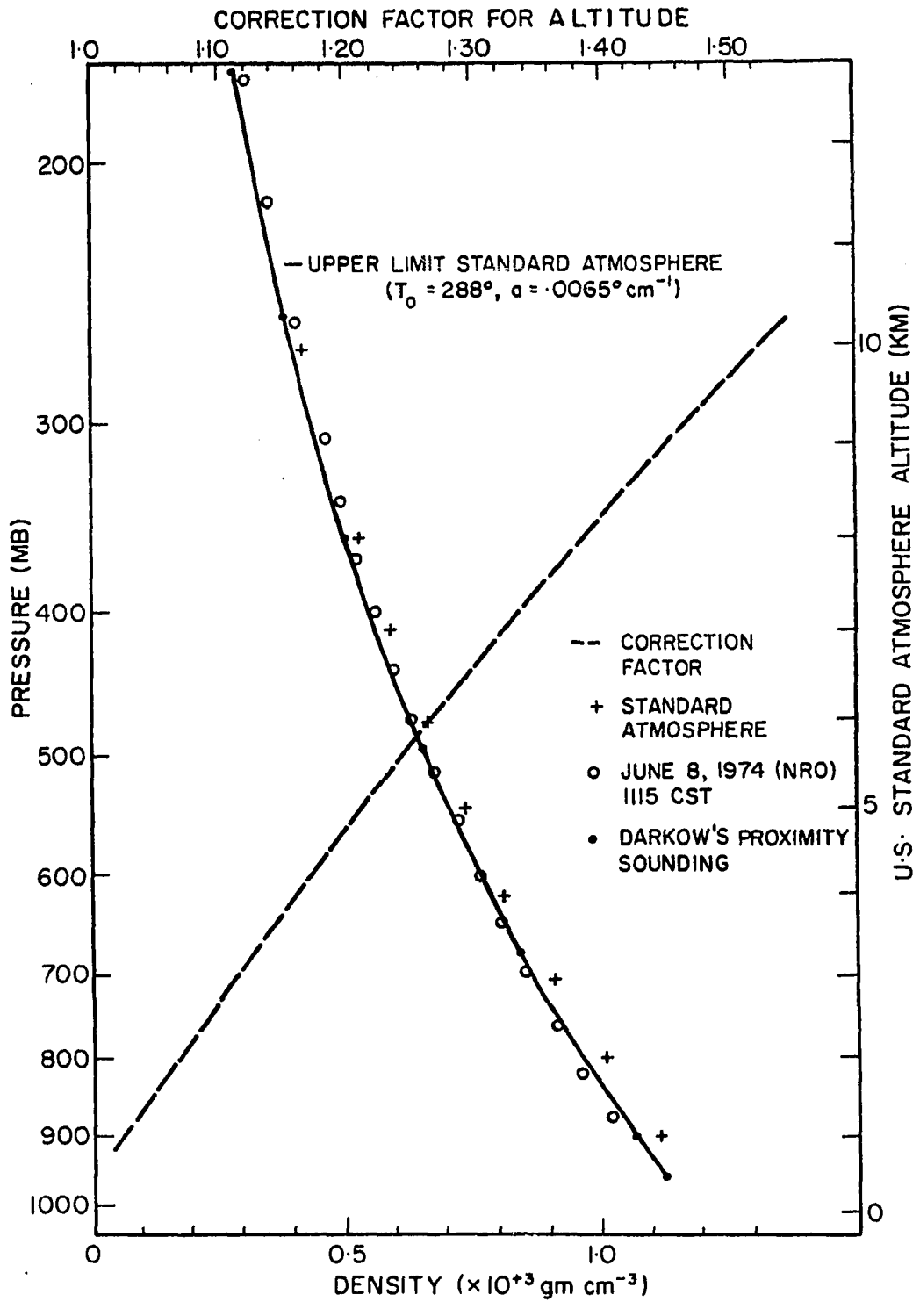

Fig. 13. Density variation with height, and altitude correction factor for fallspeed given in Fig. 12.

c) the June 8, 1974, environment sounding at 1115. The empirical relation was obtained from a quadratic fit to Darkow's data

$$\rho(z) = 1.17 - .103z + .003z^2 \ , \qquad (5)$$

where z is in kilometers and ρ is in kg cm^{-3}. Due to its generality and reasonable fit to c), it is used in subsequent calculations, although the density variation within clouds is presumably much more complex.

The analysis in Heymsfield (1976) is modified so as to interpolate v_a' rather than v_r'. It is mentioned that previous analyses interpolated v_r'. This modification uses the range gate Z_e rather than one which has been interpolated to a grid-point from, for example, a region of strong reflectivity gradients. The observed air motion for a range gate may now be separated into a true value v_a at the pulse volume center and a fluctuation due to uncorrelated errors:

$$\begin{aligned} v_a' &= (v_r + \delta_r) - (v_T \sin\theta + \delta_t) \\ &= v_a + \delta \end{aligned} \qquad (6)$$

where the unprimed quantities represent the true values (neglecting systematic biases), δ_r and δ_t are the errors corresponding to the two terms on the right side of (3), and $\delta (=\delta_r + \delta_t)$ is the random error in the observed air motion. The δ_t is due to uncertainty in the Z_e estimate

(about 1 dBZ from Heymsfield (1976)), which according to Doviak et al. (1976a) is theoretically quite small. Thus, δ is about 2.3 m s^{-1}, as an average value. Position errors have been neglected, and from assumption ii), $\langle v_a' \rangle = \langle v_a \rangle$ and $\langle \delta \rangle = 0$ where the angle braces indicate ensemble average value. Justification for ignoring trends may be found in Gandin (1963) for a dense observation network, as is the present case.

For each radar, an independent objective analysis is performed. The v_a' are interpolated to grid-points in both Cartesian and cylindrical frames. The grids are oriented as shown in Fig. 10 with $\Delta = \Delta x = \Delta y = \Delta z = \Delta r = \Delta s = 1$ km, and $\Delta\alpha = 1.4°$. At each grid-point in either coordinate system, the interpolated radial air motion $\hat{V}_A$ is estimated from the v_a' in the vicinity of the grid-point, by the linear combination of M observations.

$$\underset{\sim}{\hat{V}}_a = \underset{\sim}{v}_a' \, \underset{\sim}{\phi} \, , \tag{7}$$

where $\underset{\sim}{\hat{V}}_a$ is a (N×1) column vector, $\underset{\sim}{v}_a'$ is a (N×M) matrix, $\underset{\sim}{\phi}$ is a (M×1) column vector of population weights, and N is the number of observation sets. The direction of $\hat{V}_a$ is given by the radar radial passing through the grid-point. It is desired to minimize the mean square interpolation error E of the difference between the true grid-point value, V_A, and $\hat{V}_A$:

$$E = \overline{(\underset{\sim}{V}_a - \underset{\sim}{\hat{V}}_a)^2} \, . \tag{8}$$

The weighting coefficients ϕ and interpolation error are predicted from a linear regression model, for which details are given in Eddy (1973) and Heymsfield (1976). The total variance of the observations, σ_T^2, is partitioned according to

$$\sigma_T^2 = \sigma_{v_a}^2 + \sigma_\delta^2 = \sigma_{v_a}^2 \, (1 + (SNR)^{-1}), \tag{9}$$

where $\sigma_{v_a}^2$ is true variance of the radial air motions, σ_δ^2 is due to uncorrelated fluctuations, and SNR, or $\sigma_{v_a}^2/\sigma_\delta^2$, is signal-to-noise ratio. The SNR is assumed constant and σ_T^2 is assumed homogeneous over a field of observations. The true b and estimated $\hat{b}$ space-time autocorrelation function (ACF) are related by

$$b = \hat{b} \, (1 + (SNR)^{-1}). \tag{10}$$

The estimated data weights may now be given by the relation

$$\hat{\underset{\sim}{\phi}} = \hat{\underset{\sim}{b}}^{-1} \hat{\underset{\sim}{b}}_0 \quad , \tag{11}$$

where $\hat{\underset{\sim}{b}}$ is a (M×M) matrix, and $\hat{\underset{\sim}{b}}_0$ is a (M×1) column vector. The i, j matrix elements are given by $\hat{b}_{ii}$ equal 1, $\hat{b}_{ij}$ are the estimated autocorrelation between the i^{th} and j^{th} observations; where i = 1 .., M, j = 1, .., M, $\hat{b}_{0i}$ are the estimated autocorrelation between the i^{th} observation and the grid-point value, the $E\left[\hat{\phi}\right] = \phi$, and $E[\ ]$ indicates expected value. The fraction of unexplained variance at the grid-point is given as

$$\varepsilon = (1 - b_{\underset{\sim}{0}}{}^{t} \hat{\underset{\sim}{\phi}}) \quad , \tag{12}$$

where $\varepsilon = E/\sigma_T^2$. The residual at a grid-point in the classical regression is $\underset{\sim}{e} = \underset{\sim}{V}_a - \hat{\underset{\sim}{V}}_a$, where V_a is taken as the grid-point value of v_a'. The ten closest observations (i.e., M = 10) were interpolated to a grid-point, since ε was insensitive to inclusion of additional observations.

The M weights in (7) are determined from the statistical structure given by the space autocorrelation of the data. Homogeneity is assumed so that irrespective of position, the autocorrelation depends only on the vector distance between two points. In a previous study of June 8, 1974, discrete three-dimensional ACF were computed in the x',y',z coordinate system for each radar and also over separate 15 × 15 × 4 km^3 storm regions (Fig. 14). The requirement for homogeneity is better satisfied for separate storm sections since they may contain different physical phenomena. For these calculations, the "frozen turbulence" or Taylor hypothesis was assumed. This states that when the spatial atmospheric field is advected at a uniform velocity $\vec{S}$ without any mixing or changes of the structure, then

$$b\ (\vec{r}_1 - \vec{S}T) = b\ (\vec{r}_1, T)\ , \qquad (13)$$

where $\vec{r}_1$ and T, are space and time lags, respectively. Thus, the ACF of a field varying in both space and time was replaced after a translation of the radial velocity observations by an autocorrelation function depending only on space. This assumes the storm structure is neither evolving or dis-

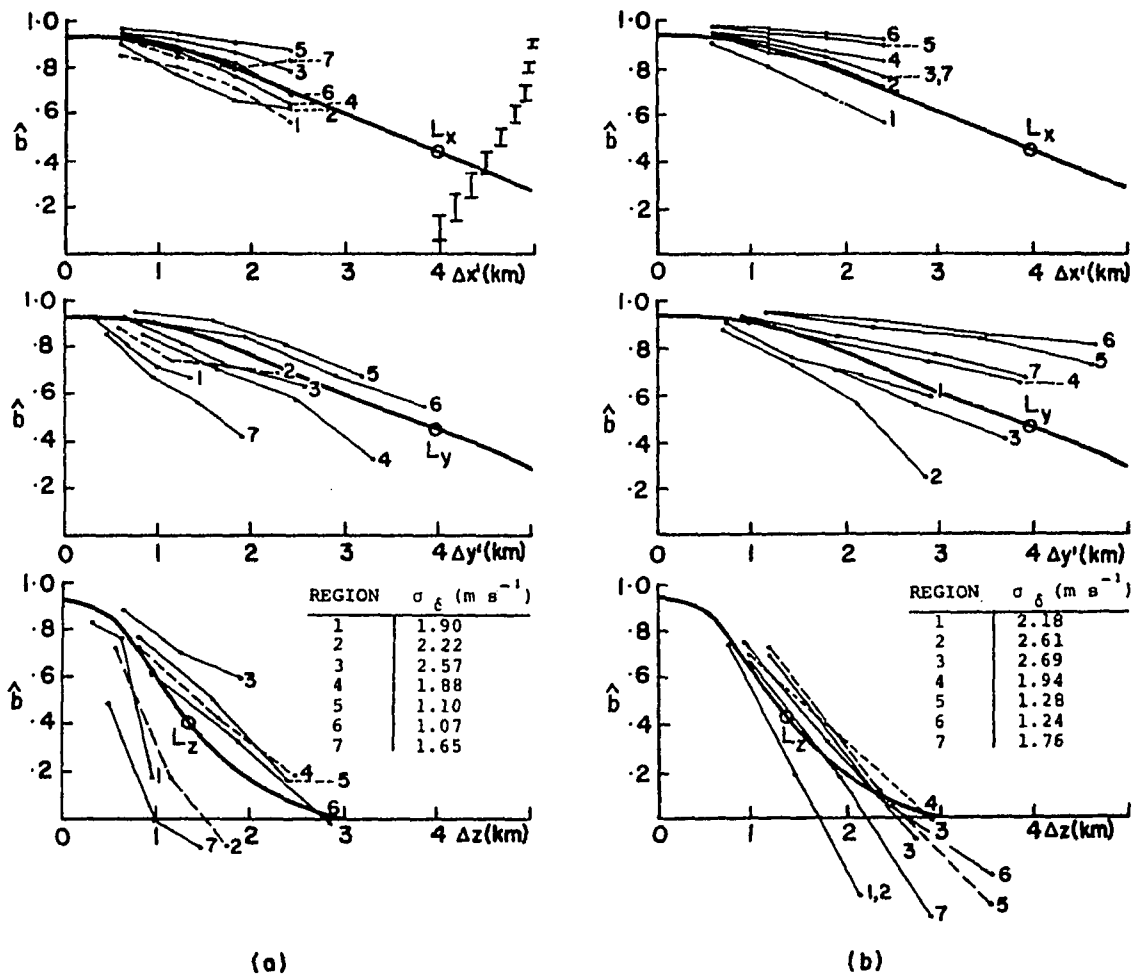

Fig. 14. The unsmoothed discrete ACF for (a) Norman radial velocity, and (b) Cimarron radial velocity. Analytical relation according to (15) is shown by thick curve. 95% confidence intervals are given in (a) top for $\hat{b}$ = 0.1, 0.2, ..., 0.9 and a sample size of 1000. L_x, L_y, and L_z computed from (15) are also shown. The computed observation noise for each region is tabulated. Regions 1 through 7 are as given in Heymsfield (1976).

sipating over the few minutes of data collection. It is not possible to test this assumption with the present data having 10 min time intervals; however, it is reasonable over the short data collection period if the storm structure is quasi-steady.

The important question of what value of $\vec{S}$ to use is perhaps one of the weakest points in the analysis. The advection vector was assumed as $\vec{V}_s$ (uniform with height), or what is later seen to be approximately the movement of the main updraft core of storm A. This appears reasonable if the high-speed updraft is viewed as the core of the storm, with all other air motion relative to it. Each measurement, v_a', was thus adjusted horizontally according to a reference time T_0 as follows

$$v_a'(X,Y,z,T_0) = v_a'(X-U_s t', Y-V_s t', z, T_0+t'), \quad (14)$$

where U_s, V_s are the components of $\vec{V}_s$, t is observation time and $t' = t-T_0$. The time to space conversion enables the weighting of data according to spatial position, rather than in the space-time frame in which it is collected.

For reasons of computer economy, an analytical ACF is used as representative of all storm regions and for both radars. Recall that the ACF's in Fig. 14 are anisotropic and asymmetric. These ACF's as well as from three other data collection times, suggest some general features of the ACF for the Doppler radar data on June 8, 1974: 1) $\hat{b}(0,0,0)$

averaged over 48 ACF's is .930, or a signal-to-noise ratio of 11.23 dB (equivalently a r·m·s error of about 2.3 m s^{-1}); 2) $\hat{b}$ falls off faster in the vertical z-direction than horizontally; and 3) the functions are elliptic sometimes oriented in the mean wind direction. Based on these results, a Gaussian function was used for a subjective fit to the observed ACF's and is shown in Fig. 14:

$$\hat{b}(x',y',z) = 0.93\exp\left[-\{(x')^2/20 + (y')^2/20 + (z)^2/2.25\}\right] . \quad (15)$$

This function is anisotropic in z, and statistically independent in x',y' and z. It was not necessary for this function to become negative since the lag intervals used in computations were smaller than that where the autocorrelation becomes zero. The integral scale of the ACF is defined by $L_x = \int_0^\infty b\, dx$, $L_y = \int_0^\infty b\, dy$, and $L_z = \int_0^\infty b\, dz$. It gives a rough measure of the interval over which v_a is correlated with itself. According to (10) and (15), $L_x = L_y = 3.97$ km, and $L_z = 1.33$ km. Using the Taylor hypothesis, the equivalent horizontal time scale would be about 5.5 min. Adequate sampling of these space scales on a three-dimensional grid would require greater than 3 grid-points within L_x,L_y and L_z, i.e., $\Delta x = \Delta y \lesssim 2$ km, and $\Delta z \lesssim 0.65$ km. The $\Delta x = \Delta y =$ 1 km clearly meet this requirement. Analysis of vertical scales would benefit by a reduced Δz, but the 1 km grid-spacing was used due to limited computer storage.

Computation of Three-Dimensional Wind Field

The basic theory of three-dimensional wind computations from two Doppler radars for an anelastic atmosphere is discussed by Armijo (1969). Later observational investigations such as Miller and Strauch (1974), and Ray et al. (1975) solve the cylindrical continuity equation for the vertical component rather than the more difficult inhomogeneous hyperbolic partial differential equation suggested by Armijo. The following uses the cylindrical coordinate system only for vertical velocity computation.[9] The wind components are defined as in Fig. 10. The u_r and u_s wind components are computed in both coordinate systems from $\hat{V}_{a1}$ and $\hat{V}_{a2}$ where 1 and 2 refer to the Norman and Cimarron radars, respectively. The u_r wind component is directed perpendicular to the radar baseline, while the u_s wind component is parallel to the radar baseline. The u_r and u_s components are given by

$$u_r = \frac{r_2 \hat{V}_{a2} s - r_1 \hat{V}_{a1} (s - 2d)}{2\ dr}$$

$$u_s = \frac{r_1 \hat{V}_{a1} - r_2 \hat{V}_{a2}}{2\ dr} \quad , \qquad (16)$$

where $r_1 = (r^2 + s^2)^{1/2}$, $r_2 = (r^2 + (s-2d)^2)^{1/2}$, $s = y$, $2d$ is the separation distance between the two radars, and $\hat{V}_a$

[9] The present analysis differs from previous analyses in that they interpolated u_r, u_s, u_α components from tilted planes to constant altitude planes. The current application is less subject to error in the v components since they are computed on Cartesian coordinates from only one interpolation.

is the interpolated radial air motion from each radar. The u_s component is the Cartesian v component, while the u_r component is tilted, and perpendicular to the radar baseline. The u_α component, which is directed normal to the tilted plane, may be found from the cylindrical coordinate continuity equation using winds in cylindrical coordinates:

$$\frac{1}{r}\frac{\partial}{\partial r}(r\rho u_r) + \frac{1}{r}\frac{\partial}{\partial \alpha}(r\rho u_\alpha) + \rho\frac{\partial}{\partial s}(u_s) = 0 \ , \qquad (17)$$

where $\rho = \rho(z) = \rho(r,\alpha)$. This anelastic form of the continuity equation $\nabla\cdot\rho(z)\vec{V}$ is for deep convection (Dutton and Fichtl, 1969) as in the case of a severe storm where vertical scales are the same order of magnitude as the scale height. The expansion or contraction of parcels moving in the vertical is taken into account. This assumption may not hold in severe storms, but as will be seen later, other problems (e.g., errors in the data) are more serious. With (5), (16) and (17), a complete set of equations results, i.e., along with the fallspeed relation (4) previously assumed.

The u_α are obtained at the i^{th} level by integration of (17) over α using trapezoidal integration:

$$u_\alpha^i = (\rho^{i-1}/\rho^i)\ u_\alpha^{i-1} - \left[r\rho\partial/\partial s(u_s) + \partial/\partial r(r\rho u_r)\right]^{i-\frac{1}{2}}\Delta\alpha/\rho^i \ , \qquad (18)$$

where $i = 1, 2....n$, u_α^0 is the vertical component at the surface (assumed zero), and the integration starts at the surface where $\alpha < 0°$ due to the earth's curvature. The in-

tegration of (18) requires u_s and u_r components on the surface which are not available from Doppler measurements. The lowest measurements used are those interpolated on the $\alpha = 0°$ plane, which are also used as surface winds. The derivatives in (18) were computed by centered differences in the numerical computations.

The horizontal winds are now obtained from the cylindrical wind components by the relations

$$\begin{aligned} u &= u_r \cos \alpha - u_\alpha \sin \alpha \\ v &= u_s \\ w &= u_r \sin \alpha + u_\alpha \cos \alpha \end{aligned} \qquad . \qquad (19)$$

The w component at a Cartesian grid-point is computed from an average of the nearest 2 to 3 w components in a r-z plane of cylindrical coordinates. The u component is determined from the u_r and w components according to the relation

$$\begin{aligned} u &= (x^2 + z^2)^{\frac{1}{2}} u_r/x - (z/x)w \\ &= A\, u_r - B\, w \; . \end{aligned} \qquad (20)$$

Interpolation to the two coordinate systems in the above application requires reduced interpolation, in comparison to when both u and v are interpolated from the cylindrical to Cartesian frame. An approximate u component (i.e., u_r) may also be obtained for low-elevation angles when the w component is not available due to insufficient data at lower levels (e.g., in the echo overhang). The error in approximating u by u_r is w tan α. For example, a

2.1 m s^{-1} error in u results when w = 20 m s^{-1} and $\alpha = 6°$. To summarize the above application: i) the v component and the basic u(or, u_r) component are evaluated directly at one reference time on constant altitude planes without further interpolation, and, ii) the error in the v component on horizontal planes will be smaller than re-interpolating v from cylindrical coordinates.

Errors in Interpolated Velocities

The errors in the three-dimensional winds due to random errors in radial velocities and fall velocity estimates and the bias errors resulting from an incorrect fall velocity relation and from use of the incompressible versus anelastic continuity equation are discussed by Doviak et al. (1976a). In this section we examine: i) the use of an analytical rather than empirical ACF, ii) the interpolation errors at grid-points which may be used in estimation of wind errors and iii) the sensitivity of the analysis to the advection speed assumed in adjustment of data to a common reference time.

Fig. 15 shows analyzed $\hat{V}_{al}$ grids at 1555 centered on x = 36 km, y = 1 km for $\alpha = 1.4°$ and $\alpha = 8.4°$. The top grids for each level were obtained by using (15). Grid-point values were also obtained using the empirical ACF computed over this same 15 × 15 × 8 km^3 region. The bottom grids for each level show difference fields between the two

$\hat{b}_{00}$ = .938 σ_δ = 2.6 m s^{-1}

$\hat{V}_{al}$ (analytical)

24.3	25.2	24.0	27.1	26.3	26.1	28.9	29.4	29.5	29.8	30.4	29.2	27.8	27.5	24.8	
29.5	32.3	30.7	39.1	26.9	27.3	30.7	30.6	29.3	30.1	39.8	26.5	19.4	11.4	3.5	
33.7	31.3	39.1	26.9	27.3	27.8	30.4	30.5	29.3	29.6	27.5	25.9	17.4	8.1	-2.2	
32.7	28.7	28.6	32.2	30.3	28.5	30.8	30.6	30.3	29.9	26.6	23.8	21.2	13.4	10.5	
31.4	28.9	30.9	32.7	30.7	29.4	30.1	30.5	29.8	30.2	27.6	23.2	21.6	21.2	19.7	
31.1	29.5	31.1	32.7	30.9	30.3	30.7	29.3	30.4	31.1	27.1	24.9	27.7	27.8	20.1	
32.8	32.4	32.3	33.5	34.2	32.5	31.1	28.1	28.2	31.4	28.1	24.5	30.3	36.3	32.7	
34.2	34.5	32.8	32.6	31.8	32.0	31.9	25.8	24.7	29.1	27.2	27.0	33.1	40.7	40.8	
33.5	34.5	33.8	33.3	32.2	32.3	31.0	28.1	29.6	28.9	27.2	27.9	33.2	37.4	36.3	
34.0	35.0	33.3	32.5	33.5	34.1	32.9	33.5	33.1	30.8	29.2	29.8	32.7	35.1	37.1	
33.0	33.3	32.5	32.1	33.4	34.6	35.2	35.4	34.5	32.4	30.6	31.3	33.6	35.1	37.3	8.4°
31.3	32.4	32.7	33.4	34.6	35.7	36.7	36.7	36.5	35.4	34.2	35.4	36.7	35.5	36.6	
31.0	31.2	32.6	34.0	35.6	35.9	36.2	37.2	37.1	36.8	36.8	37.1	37.3	37.0	37.3	
31.0	31.8	32.5	34.0	35.1	35.5	35.0	35.8	37.0	37.1	37.3	37.5	37.6	37.5	37.5	
33.1	31.9	31.6	31.6	34.7	34.3	34.4	35.0	36.2	36.5	37.1	37.9	37.6	37.5	37.6	

Correlation Coefficient = 0.99

$\hat{V}_{al}$ (empirical)

$-\hat{V}_{al}$ (analytical)

0.2	-0.3	0.3	-0.9	0.4	-0.2	0.4	0.7	0.1	-0.7	-0.2	1.0	-1.2	-2.4	1.0	
0.1	-0.5	0.8	0.3	0.4	-0.2	1.3	0.7	0.7	-0.2	0.2	-0.2	-1.6	0.2	-1.2	
0.4	0.3	0.2	0.2	-0.1	0.1	0.5	0.5	0.6	-0.4	1.2	1.8	1.4	2.0	0.8	
-0.1	0.4	-0.8	0.6	1.0	-0.1	-0.0	0.8	0.7	0.4	1.5	-1.5	2.8	3.6	2.0	
0.0	0.2	-0.8	-0.2	0.2	-0.8	1.0	0.5	0.1	-0.4	1.5	1.7	1.2	1.2	1.0	
-0.1	-0.0	-0.1	-0.6	0.4	-0.1	0.1	0.8	0.0	-0.1	2.0	0.4	-0.6	2.7	1.4	
-0.3	-0.5	-0.3	-0.7	-0.5	0.0	0.3	0.5	-0.4	0.6	1.2	0.6	-0.6	1.1	1.9	
0.3	0.4	0.2	0.3	0.3	0.5	-0.6	0.1	-0.9	-0.3	1.9	0.2	-1.3	0.9	0.7	8.4°
0.7	0.3	0.5	-0.0	0.2	0.4	0.9	1.3	0.5	1.1	0.7	0.8	-1.3	0.5	-0.2	
0.2	0.2	0.6	-0.3	0.2	0.2	1.6	-0.0	0.8	1.0	-0.1	0.3	-0.8	0.4	-0.4	
0.1	0.0	-0.1	-0.1	-0.5	-0.1	0.1	0.5	0.3	1.1	0.7	0.0	-0.7	0.0	-1.3	
0.3	-0.4	-0.1	-0.4	-0.3	-0.1	-0.1	0.3	0.4	1.1	0.9	0.6	0.4	0.2	0.6	
0.2	-0.2	0.2	0.1	-0.7	0.2	0.2	0.0	0.1	0.1	-0.1	0.8	0.3	0.2	0.3	
-0.3	-0.3	-0.1	-0.4	-0.3	-0.3	0.2	0.1	0.3	0.4	0.1	-0.2	-0.2	-0.1	-0.1	
0.6	-0.0	-0.2	0.3	0.3	0.2	-0.2	0.1	0.1	0.7	0.1	-0.2	-0.1	-0.1	-0.2	

$\hat{V}_{al}$ (analytical)

10.8	11.9	13.9	17.3	18.1	18.7	20.8	20.7	22.7	22.6	20.1	14.7	11.7	8.0	6.4	
10.1	11.8	14.2	14.2	15.9	18.0	19.3	19.4	20.0	17.6	15.5	12.3	11.4	9.5	6.5	
8.8	12.3	11.8	11.4	12.6	13.7	13.8	13.0	14.4	14.8	12.8	10.9	12.0	10.9	6.4	
13.8	13.8	12.5	14.3	13.1	10.0	9.3	10.1	8.8	10.4	10.5	9.1	5.8	7.0	2.9	
13.6	13.9	14.5	14.6	15.7	11.0	13.9	13.5	12.0	10.9	6.5	3.7	-3.9	-7.3	-4.7	
13.3	14.0	16.0	14.9	15.2	18.4	16.3	14.2	12.7	9.2	3.8	1.0	-4.8	-6.2	-4.1	
15.8	15.0	15.9	15.5	16.9	17.5	15.4	15.1	17.3	15.7	7.4	-3.5	-1.5	7.0	7.0	
17.4	17.6	15.6	17.6	18.9	16.0	13.1	13.1	14.6	14.4	9.6	5.3	10.0	16.3	16.3	1.4°
17.2	17.4	15.8	18.1	18.6	13.5	9.4	8.2	6.1	4.7	6.7	17.8	21.2	19.0	21.1	
17.2	19.2	20.2	19.8	21.0	17.4	12.3	10.3	10.5	12.0	17.6	23.0	24.2	23.8	25.9	
19.1	19.3	19.6	20.8	22.8	23.1	22.4	19.5	20.6	20.0	21.5	24.7	27.2	28.0	29.2	
24.5	22.4	22.7	21.9	21.9	23.1	24.1	24.5	25.1	20.7	24.0	26.3	29.5	30.3	30.6	
24.5	25.5	24.3	24.5	24.4	25.0	24.8	23.3	21.2	21.3	23.9	25.7	28.0	28.7	28.4	
25.5	25.6	25.3	25.6	26.8	27.4	26.3	22.9	19.6	20.7	23.1	24.5	27.3	27.9	24.1	
26.6	28.1	25.8	25.8	25.9	28.1	27.6	30.6	21.0	21.4	25.1	27.8	31.7	31.2	22.8	

Correlation Coefficient = 0.96

$\hat{V}_{al}$ (empirical)

$-\hat{V}_{al}$ (analytical)

1.3	1.5	0.7	0.5	-1.3	2.5	0.8	-3.5	-1.4	0.8	0.0	-1.6	-0.3	-2.4	-2.9	
1.9	0.9	1.1	1.1	1.8	1.2	1.8	1.2	1.0	5.3	4.5	2.7	-0.6	0.8	-2.8	
3.3	0.2	0.6	2.4	1.7	0.1	-1.1	4.1	4.5	-0.4	0.0	1.1	1.9	2.2	4.9	
1.8	0.9	2.6	3.8	2.6	-1.8	-3.5	-1.5	-0.4	-0.7	0.2	1.1	7.3	1.5	-1.4	
2.6	4.0	2.5	1.2	1.5	1.2	-0.7	0.2	-1.3	2.6	4.1	4.2	0.3	-1.3	-1.6	
1.3	1.2	3.4	2.8	3.9	2.1	-0.5	-1.9	-0.1	1.7	-2.2	-0.7	-5.1	-6.9	-5.9	
0.9	1.8	2.0	3.6	1.6	0.7	0.4	-0.7	-0.7	-3.2	-4.7	-1.7	-4.1	-3.9	-3.4	
0.6	-0.1	2.0	0.9	1.1	-0.6	1.6	1.1	0.6	4.9	3.5	1.7	-1.2	1.6	4.0	1.4°
2.5	2.0	3.2	1.5	0.9	0.4	1.9	2.4	5.4	3.7	1.1	-2.0	-1.7	2.6	-2.1	
3.0	3.0	3.4	2.3	1.6	2.6	2.8	-0.3	-4.3	-4.1	0.8	-0.1	-1.0	-2.5	-2.1	
1.8	1.7	1.5	1.6	0.3	1.1	1.1	-1.2	0.3	-1.8	-1.2	-2.6	-1.1	-1.3	-1.0	
-0.6	-0.8	-1.4	0.3	1.8	0.3	-0.9	1.5	-1.5	1.3	2.3	1.6	0.2	-0.3	-0.2	
1.0	0.9	0.9	1.4	-0.7	-1.4	-0.7	-3.8	-2.9	-1.6	-2.4	-1.9	0.8	0.5	-0.3	
0.1	-0.3	0.7	0.4	-0.5	-1.6	0.1	0.0	1.1	1.1	0.9	0.2	1.5	1.8	-1.3	
-0.1	-0.9	3.0	2.9	5.3	0.4	1.9	0.2	4.7	5.0	4.8	-0.0	1.1	0.7	0.5	

Fig. 15. Comparison tests between $\hat{V}_{al}$ computed with (15) and also the empirical ACF. The grids are centered at x = 36 km, y = 1 km at 1555 and $\alpha = 1.4°, 8.4°$. Grid-point values are in meters per second and grid-spacings are 1 km. A 99. indicates missing data due to weak reflectivity.

computations. The cross-correlation coefficients between these fields were 0.96 and 0.99. The use of the generalized function (15) rather than the empirical ACF function using linear interpolation as in Heymsfield (1976) gives smoother fields. The largest differences of a few meters per second occur in regions of strong horizontal shears (e.g., the tornado cyclone) on the right side of Fig. 15. The generalized expression in (15) may not represent the structure of this region as accurately as the empirical function for this particular section of the storm. Its use however is desirable since the continuous function gives lower interpolation errors at grid-points (as given in (12)), uses half the computer time, and gives smoother fields.

The statistical objective analysis attempts to obtain the true value at a grid-point, from observations having errors. The Eddy-Gandin interpolation provides an estimate of the interpolation error at a grid-point, as well as the random errors (σ_δ) in the v_a'. Thus the effectiveness of the analysis to reduce the σ_δ while interpolating the v_a' to grid-points may be determined. Let us assume that at a grid-point an observation which we call V_a exists. An interpolation of v_a' to this point would produce a residual interpolation error e previously defined, or a model error according to the assumed ACF in (15) and from (12) may be determined. Brady (1976) has performed

these tests on rainfall data using the Eddy analysis. Three error quantities are similarly obtained from the above Doppler analysis by i) performing an interpolation at a data point v_a' and obtaining $\overline{e^2}$ over a large number of interpolations from a region, ii) computing the interpolation error $\sigma_T{}^2\varepsilon$ at each grid-point, and iii) computing $\sigma_\delta{}^2$ from the 0-lag of the ACF. For a 15 × 15 × 8 km^3 volume centered on the main updraft of storm A (i.e., x = 41 km, y = 1 km) from the Norman radar at 1555, i) was computed over 1000 observations, resulting in $(\overline{e^2})^{\frac{1}{2}}$ = 2.74 m s^{-1}. Then ii) was computed according to (12) and from the total variance over the region. The average value of these interpolation errors over the same 1000 points were 2.44 m s^{-1}. Finally, σ_δ = 3.09 m s^{-1}. It is seen that the interpolation error of about 2.5 m s^{-1} is less than the observation error. It should be noted that in computing e, the observation at a grid-point was assumed as the true value. This observation has a random error so $(\overline{e^2})^{\frac{1}{2}}$ and ε would not generally be expected to be equal. If the analytical ACF were used in these tests, $\sigma_T{}^2\varepsilon$ is about 1.9 m s^{-1} rather than 2.45 m s^{-1}. The values for the above updraft region are larger than from other storm regions (see σ_δ in Fig. 14).

The errors in the vertical w component due to random grid-point errors may be obtained according to Fig. 2 in Doviak et al. (1976a). This figure gives the ratio

σ_w/σ of standard deviations of w the vertical wind component to σ, the random grid-point error of v_r. The ratio is a function of position, and altitude, increasing with altitude. Scaling this figure for the June 8 observations gives a range 4.5 to 7.5 for the above ratio in the approximate vicinity of the Harrah storm updraft, and at 6.0 km altitude. This would suggest errors in the vertical motion of about 11 to 19 m s^{-1} when σ = 2.3 m s^{-1}.

Initial computations of u_α from (18) resulted in extremely large values. Without filtering, u_α was as large as 60 m s^{-1} at 6 km, while the parcel method in Chapter II gives only 32 m s^{-1} at 6.5 km. As this suggested the presence of small scale phenomena and random observational errors, a low-pass filter was used to reduce smaller scales. A simple three-point filter with a response 0 for 2 km wavelengths, .561 for 6 km wavelengths, and .82 for 10 km wavelengths was applied to the u_r and u_s grids in both coordinate systems. This filtering resulted in vertical velocities of about 40 to 45 m s^{-1} at 6 km, though they are still considerably larger than the parcel method. If the random errors were reduced to 1.0 m s^{-1} from filtering, then errors in the vertical component would be reduced to 4.5 to 7.5 m s^{-1} at 6.0 km. With the above filtering, only largest updrafts and downdrafts should appear in the analyzed fields.

Two additional problems may account for errors in vertical velocity computations: 1) the assumption of $\vec{V}_s$ in adjustment of data to a common reference time, and 2) evolution of the storm structure over the 5 min collection time. If the Doppler observations were all collected instantaneously, the above would have no effect on the wind computations. As this is not the case, the Taylor hypothesis in (13) and (14) was assumed. We may illustrate only the effect of the $\vec{S}$ used in (14). Fig. 16 gives examples of the w component on 1.4° and 8.4° planes computed for $\vec{S} = \vec{V}_s$ = (12 m s^{-1}, 230°) and $\vec{S}$ = (16 m s^{-1}, 210°), a difference of 4 m s^{-1} and 20°. The mean unadjusted data collection time of the lower (α = 1.4°) and upper (α = 8.4°) levels is about 1553 and 1557, respectively. The grid center is again x = 41 km, y = 1 km, and the mean altitudes of these levels are about 1 km and 6 km. The reference time is T_0 = 1555, which means that the observations are shifted by the $\vec{S}$ shown in Fig. 16. For the larger advection speed, the w component is about 8 m s^{-1} larger than when $\vec{S} = \vec{V}_s$. The slope of the updraft (i.e., w maxima on grids) is larger for the storm motion advection. This simple illustration suggests the choice of $\vec{S}$ affects both the tilt and magnitude of the updraft. Recall that the motion of storm A is assumed. Different cells and features within storm A presumably move different from $\vec{V}_s$. Thus, errors due to assumption of $\vec{V}_s$ over the en-

$\vec{S} = \vec{V}_s$
(12 m s^{-1},230°)

0.	-1.	-1.	-0.	0.	1.	3.	3.	2.	1.	1.	2.	3.
1.	1.	2.	1.	-2.	-5.	-6.	-6.	-6.	-4.	-1.	2.	4.
2.	5.	8.	9.	7.	3.	-0.	-3.	-5.	-4.	-0.	3.	6.
2.	6.	11.	17.	21.	23.	22.	18.	13.	11.	11.	9.	8.
3.	7.	12.	20.	29.	37.	40.	38.	35.	32.	28.	20.	11.
5.	10.	15.	21.	29.	38.	42.	42.	42.	42.	39.	30.	16.
8.	11.	16.	20.	23.	28.	33.	33.	34.	39.	41.	36.	22.
10.	10.	12.	14.	12.	12.	16.	17.	20.	27.	35.	38.	30.
12.	10.	8.	6.	1.	-3.	0.	4.	6.	14.	25.	35.	36.
13.	10.	6.	0.	-8.	-14.	-11.	-7.	-5.	2.	16.	30.	37.
14.	11.	5.	-4.	-14.	-22.	-22.	-18.	-14.	-6.	6.	21.	32.
99.	99.	99.	99.	-14.	-25.	-26.	-22.	-17.	-10.	-2.	7.	19.
99.	99.	99.	99.	99.	-26.	-24.	-20.	-14.	-7.	-4.	-0.	4.
99.	99.	99.	99.	99.	99.	99.	99.	99.	99.	99.	99.	99.
99.	99.	99.	99.	99.	99.	99.	99.	99.	99.	99.	99.	99.

$\frac{8.4°}{(1557, 6\ km)}$

-1.	-0.	1.	1.	1.	1.	0.	0.	0.	0.	-0.	-1.	-1.
-2.	-0.	1.	1.	1.	1.	0.	-1.	-1.	-1.	-1.	-1.	-1.
-1.	-1.	-0.	0.	0.	-0.	-1.	-2.	-2.	-2.	-1.	-0.	0.
0.	-1.	-1.	-2.	-2.	-4.	-4.	-4.	-4.	-3.	-1.	0.	2.
1.	-1.	-2.	-3.	-4.	-6.	-5.	-5.	-5.	-4.	-3.	-1.	1.
0.	-1.	-2.	-2.	-3.	-2.	-1.	-1.	-2.	-2.	-2.	-3.	-2.
-1.	-1.	-1.	-0.	2.	5.	8.	7.	4.	2.	1.	-2.	-3.
-1.	-1.	0.	3.	6.	9.	10.	9.	7.	5.	3.	-0.	-4.
0.	-1.	0.	3.	5.	5.	4.	4.	5.	4.	2.	-1.	-4.
4.	1.	1.	0.	-0.	-2.	-2.	-0.	1.	1.	0.	-2.	-3.
7.	5.	4.	1.	-2.	-5.	-4.	-2.	-1.	0.	1.	0.	0.
99.	99.	99.	99.	1.	-4.	-3.	-2.	-1.	0.	0.	1.	3.
99.	99.	99.	99.	99.	-5.	-2.	-0.	0.	2.	2.	2.	3.
99.	99.	99.	99.	99.	99.	99.	99.	99.	99.	99.	99.	99.
99.	99.	99.	99.	99.	99.	99.	99.	99.	99.	99.	99.	99.

$\frac{1.4°}{(1553, 1\ km)}$

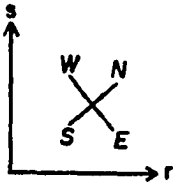

1.	-2.	-2.	-1.	1.	4.	5.	5.	4.	4.	4.	3.	2.
2.	1.	0.	-1.	-4.	-5.	-4.	-3.	-3.	-1.	2.	4.	4.
3.	5.	7.	7.	3.	-2.	-4.	-5.	-7.	-6.	1.	6.	8.
3.	7.	12.	17.	20.	19.	17.	11.	5.	2.	7.	10.	10.
3.	8.	14.	22.	32.	39.	40.	36.	32.	30.	26.	19.	12.
5.	10.	16.	24.	34.	43.	45.	43.	46.	50.	43.	29.	14.
8.	12.	16.	21.	26.	31.	32.	31.	35.	43.	43.	32.	17.
10.	10.	12.	12.	12.	12.	13.	13.	16.	26.	33.	33.	22.
11.	9.	7.	4.	-0.	-3.	-1.	1.	4.	13.	25.	33.	30.
12.	9.	5.	-1.	-7.	-11.	-9.	-7.	-4.	5.	20.	33.	36.
13.	12.	99.	99.	-10.	-19.	-18.	-15.	-11.	-2.	14.	29.	37.
99.	99.	99.	99.	99.	-29.	-26.	-21.	-15.	-8.	3.	16.	29.
99.	99.	99.	99.	99.	99.	-28.	-22.	-16.	-12.	-6.	1.	14.
99.	99.	99.	99.	99.	99.	99.	99.	99.	99.	-10.	-10.	99.
99.	99.	99.	99.	99.	99.	99.	99.	99.	99.	99.	99.	99.

$\frac{8.4°}{(1557, 6\ km)}$

$\vec{S}$
(16 m s^{-1},210°)

-1.	-0.	1.	1.	1.	1.	1.	-0.	-1.	-0.	-0.	-1.	-1.
-1.	-0.	1.	1.	1.	1.	0.	-1.	-2.	-1.	-1.	-1.	-0.
-1.	-0.	-0.	-0.	-1.	-2.	-2.	-2.	-3.	-3.	-1.	-0.	1.
0.	-1.	-2.	-2.	-3.	-5.	-5.	-5.	-5.	-4.	-3.	-1.	1.
1.	-1.	-2.	-3.	-4.	-5.	-4.	-4.	-4.	-4.	-3.	-2.	-1.
0.	-1.	-2.	-1.	-1.	0.	3.	4.	2.	0.	-1.	-2.	-3.
-0.	-1.	-0.	1.	3.	6.	9.	10.	7.	4.	2.	-0.	-3.
0.	-1.	0.	3.	6.	7.	7.	7.	6.	5.	2.	-0.	-4.
3.	0.	-0.	1.	2.	2.	0.	1.	3.	3.	1.	-1.	-3.
6.	3.	2.	1.	-0.	-2.	-3.	-3.	-1.	1.	1.	0.	-1.
7.	5.	99.	99.	2.	-3.	-4.	-3.	-1.	0.	1.	1.	1.
99.	99.	99.	99.	99.	-3.	-3.	-1.	1.	1.	1.	1.	4.
99.	99.	99.	99.	99.	99.	-2.	2.	3.	2.	2.	3.	6.
99.	99.	99.	99.	99.	99.	99.	99.	99.	99.	2.	1.	99.
99.	99.	99.	99.	99.	99.	99.	99.	99.	99.	99.	99.	99.

$\frac{1.4°}{(1553, 1\ km)}$

Fig. 16. Effect of adjustment of $\vec{S}$ on computed w. The grids are centered at x = 41 km, y = 1 km at 1555 and $\alpha = 1.4°, 8.4°$. Grid-point values are in meters per second and grid-spacings are 1 km. A 99. indicates missing data due to weak reflectivity. The approximate unadjusted data collection time, and altitude of grid center are given in brackets.

tire storm may result in inaccuracies in the wind computations.

Error in Kinematic Fields

An approximate estimate of the r•m•s error in computing divergence and vorticity can be made by considering that the errors in the u and v components are random, and uniform over the finite difference interval. Assume the r•m•s errors of the u and v components are given by σ_u and σ_v. Since later computations use centered finite difference approximations for derivatives, the r•m•s error of horizontal divergence ($\nabla \cdot \vec{V}$) or the vertical component of vorticity ($\vec{k} \cdot \nabla \times \vec{V}$) may be derived as

$$\sigma_\zeta = \left[2(\sigma_u/2\Delta)^2 + 2(\sigma_v/2\Delta)^2\right]^{\frac{1}{2}}$$
$$= (\sigma_u^2 + \sigma_v^2)^{\frac{1}{2}}/\sqrt{2}\,\Delta \quad . \qquad (21)$$

The r•m•s error of the v component is that of the interpolated u_s component. The errors in u_r and w are assumed uncorrelated at a Cartesian grid-point since the w are computed from $\hat{V}_a$ in cylindrical coordinates, and the u_r from $\hat{V}_a$ in Cartesian coordinates. The standard deviation of the u component is now computed from (20):

$$\sigma_u = \left[A^2\sigma_{u_r}^2 + B^2\sigma_w^2\right]^{\frac{1}{2}} \quad . \qquad (22)$$

Recall the constants A and B depend on x and z.

The results of the last section would suggest random errors in unsmoothed u_r and u_s of about 4 m s^{-1} (computed from Doviak et al., 1976a; Fig. 3,4), while after smoothing these errors are possibly reduced to 1.0 m s^{-1}. For an example, assume a grid-point spacing of Δ = 1 km, $\sigma_{u_r} = \sigma_v$ = 1.0 m s^{-1}, σ_w = 5 m s^{-1}, x = 50 km, and z = 6 km. the r•m•s error of u from (22) is 1.17 m s^{-1}, while the r•m•s error of divergence or vorticity from (21) is 1.09 × $10^{-3}s^{-1}$. In later chapters, it is seen that in more intense regions of the storm, the magnitudes of divergence and vorticity are often greater than 4 × $10^{-3}s^{-1}$ and 8 × $10^{-3}s^{-1}$, respectively. Therefore divergence and vorticity computations should be meaningful provided that the u_r and v winds on horizontal planes have better accuracy than approximately 0.5 - 1.0 m s^{-1}.

As an interesting side point, divergence calculations are quite difficult on the synoptic scale due to near-geostrophic equilibrium, and non-divergence at 500 mb. This is due to the nearly equal magnitude and opposite signs of $\partial u/\partial x$ and $\partial v/\partial y$. The synoptic scale vorticity calculations do not have this problem. For comparison, tests were performed on storm scale divergence and vorticity, computed from Doppler data. Two ratios $R_1 = |(\partial u/\partial x + \partial v/\partial y) / \partial u/\partial x|$ and $R_2 = |(\partial v/\partial x - \partial u/\partial y) / \partial v/\partial x|$ both tended to be greater than unity on the average, with values occasionally as low as 0.1. On the synoptic scale R_1 tends to be about 0.1.

From this chapter, several error sources in the wind computations are noted. Random errors of the interpolated grid-point values of $\hat{V}_a$ are significant and may produce large errors in the three-dimensional winds. Errors also arise from assumption of Taylor's hypothesis, as discussed. It is concluded that a study of storm scale phenomena (horizontal length scales greater than 5 km and vertical length scales greater than 1 km) is more appropriate for this set of observations as the above problems become less significant for these larger scales.

CHAPTER IV

PHYSICAL STRUCTURE OF HARRAH STORM

The three-dimensional winds and radar reflectivity are synthesized in this chapter from four analysis times (1545, 1555, 1605, 1613) to determine the physical structure of the Harrah storm. To facilitate comparisons to previous airflow and storm steering models, the discussion first presents various details of the airflow, reflectivity and kinematic quantities from which a storm structure is later suggested. Throughout this chapter, it is taken into account in interpretation that the u and v components have much greater accuracy than the w component. Recall that the u_r and v winds are sometimes displayed for cases when the w component does not exist at a grid-point. It should be noted that the inflow region of SR storms is generally associated with a WER. The inflow region of the Harrah storm was not void of echo enabling computation of three-dimensional winds in this region.[10] At 1555, the structure is examined in more detail by vertical cross-sectional

[10]Although a hook echo is seen, the inflow-updraft region is not void of echo as in the conventional definition of weak echo region; however, this terminology is used.

and precipitation trajectory analysis. The Harrah storm is well developed at this time and it is recalled that the reported tornado is at the surface.

Space-Time Continuity of Horizontal Fields

For purposes of later interpretation, Fig. 17 gives the cell structure for the different times as deduced from the reflectivity and vertical velocity observations. The dual Doppler radar coverage for each time is enclosed by solid lines. The large dots and the height in kilometers indicate radar tops when the WSR-57 radar scanned above or near the storm tops. The positions of the NRO and CMF radars are shown relative to the 1555 time. Figs. 18-22 give space-time representations of reflectivity, storm relative horizontal wind vectors, vertical motion, vertical component of relative vorticity ($\vec{k} \cdot \nabla \times \vec{V}$), and convergence $(-\nabla \cdot \vec{V})_h$, for 0.5, 3.5, and 6.5 km.[11] These figures readily show the space-time continuity and translational motion of the centers of vorticity and vertical motion, which may be tracked by straight lines. The position of the surface tornado damage track is shown on the 0.5 km level. Although the 1613 updraft is not as easily interpretable as other times, it is shown because there is some consistency of the fields with those of earlier times. Two

[11] All winds henceforth are relative to cell A_1, which moves at a velocity $\vec{V}_s$ defined in Chapter II.

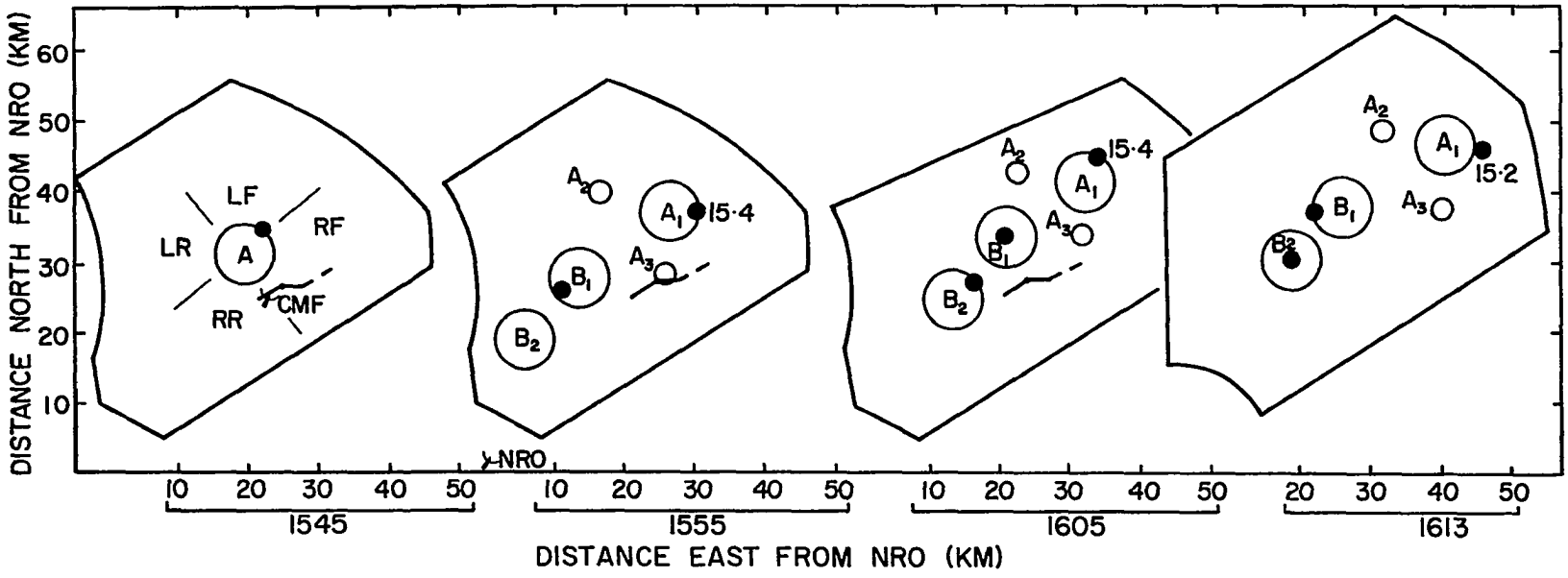

Fig. 17. Cell structure for 1545, 1555, 1605 and 1613. The approximate positions (large dots) and height in kilometers of storm tops are indicated when radar data was available. Surface Harrah tornado track is shown by thick line; the small dot indicates the 1555 position. The locations of the Norman (NRO) and Cimarron (CMF) radars are shown only for 1555; regions of common radar coverage are outlined by thickest lines. Storm quadrants (e.g., RR is right rear flank) are shown for cell A_1 at 1545. The expected location of cell A_3 is given at 1555.

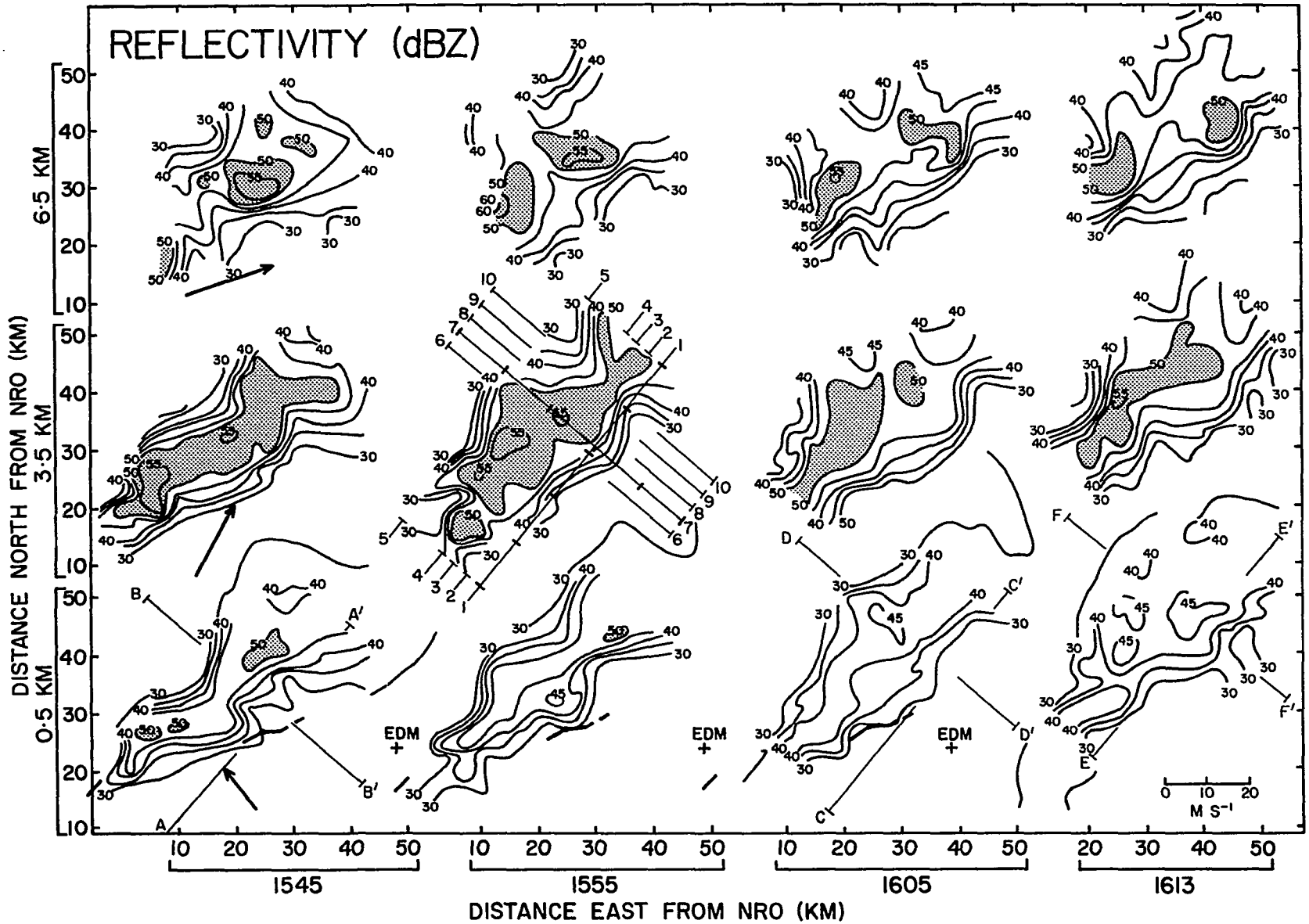

Fig. 18. Reflectivity fields. Contours are in intervals of 10 dBZ, unless otherwise indicated. The outer 30 dBZ contours at 0.5 km were partly from WSR-57 data. The environmental winds relative to cell A_1 are shown at the three levels and 1545 (scale at lower right). Positions of vertical cross-sections and surface tornado tracks are indicated. EDM is Edmond, Oklahoma.

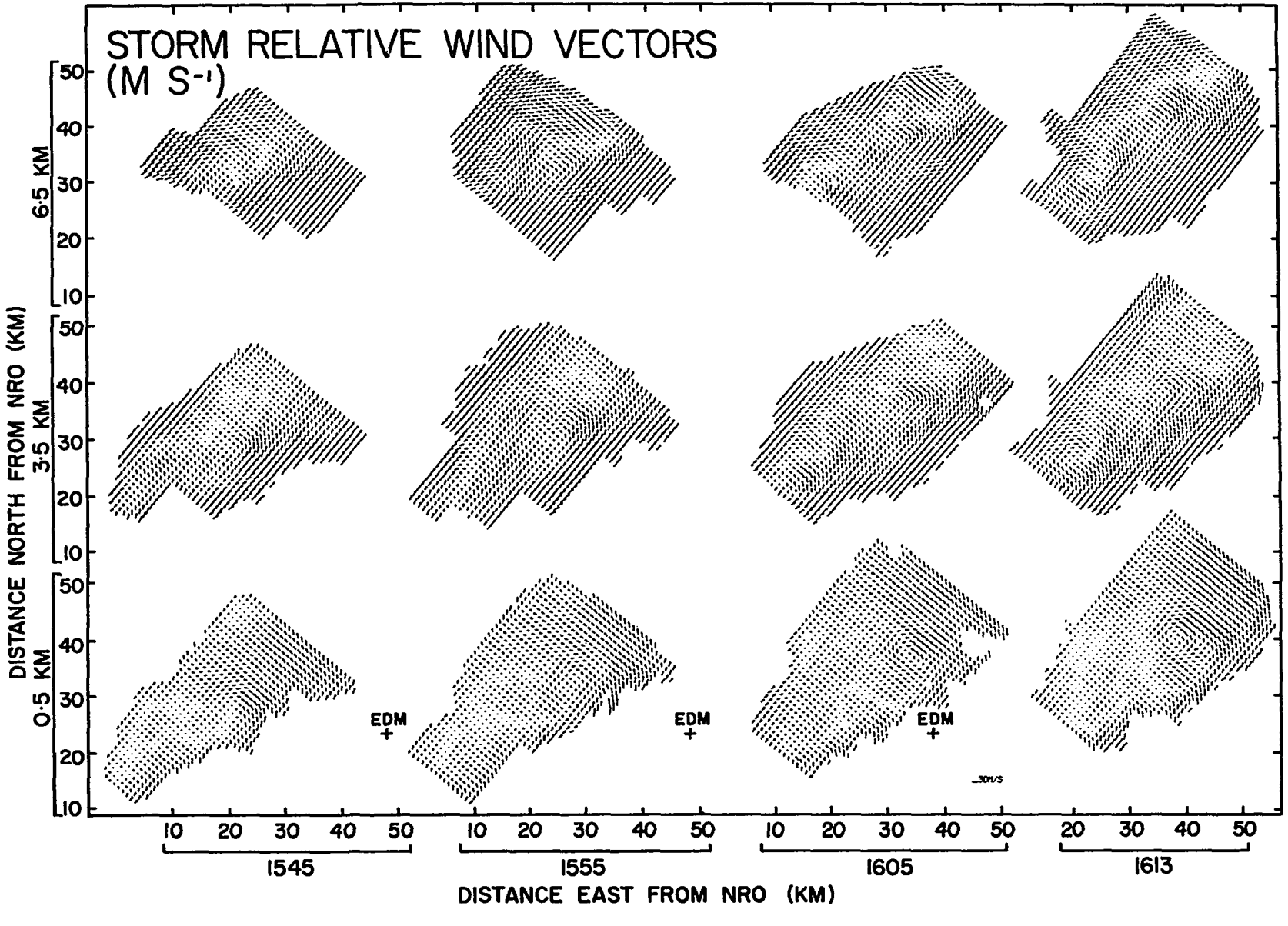

Fig. 19. Storm relative wind vectors. Velocities less than 4 m s^{-1} are indicated by a dot.

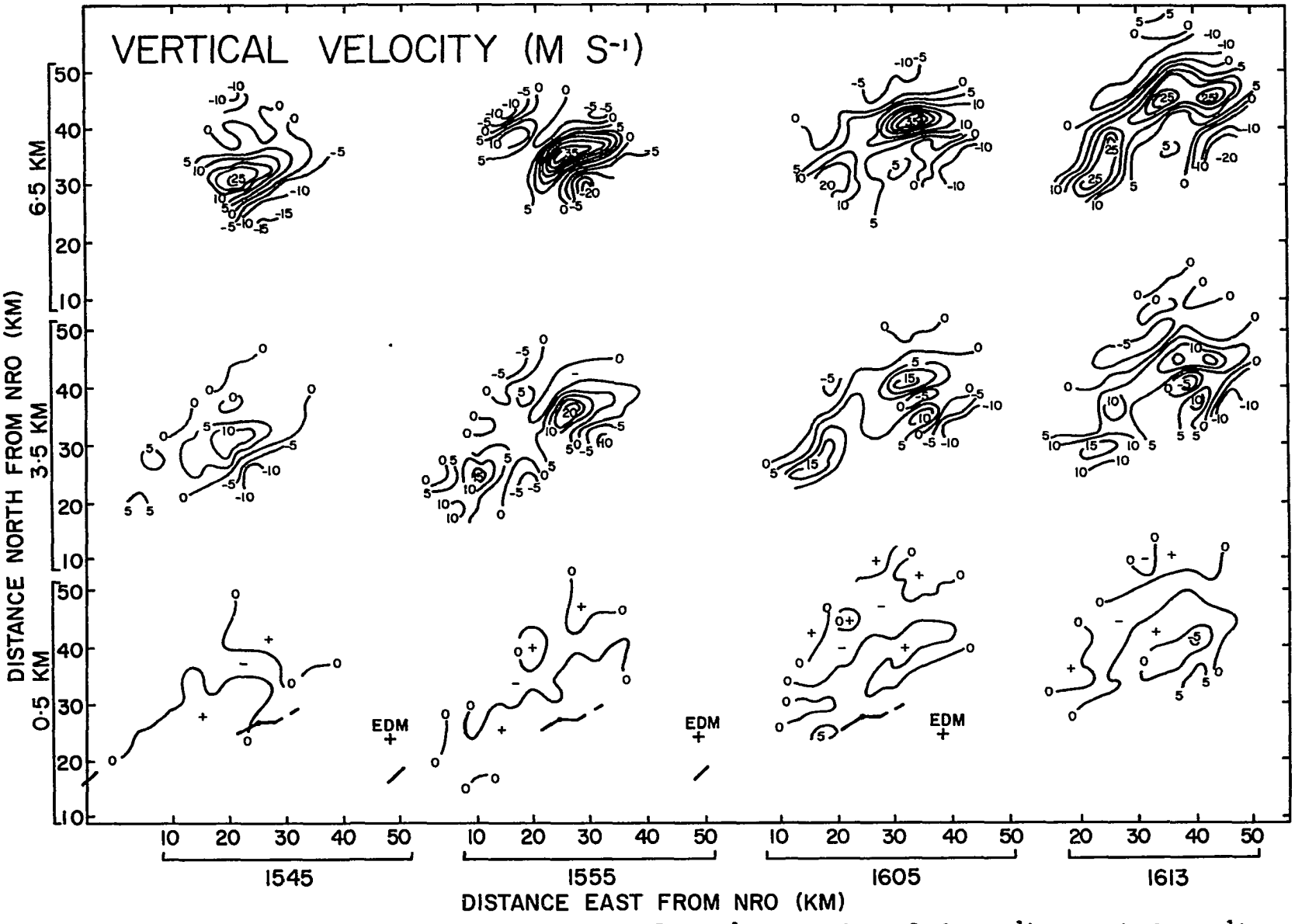

Fig. 20. Vertical velocity. Contours given in 5 m s^{-1} intervals; +(> 0 m s^{-1}), or -(< 0 m s^{-1}) are indicated.

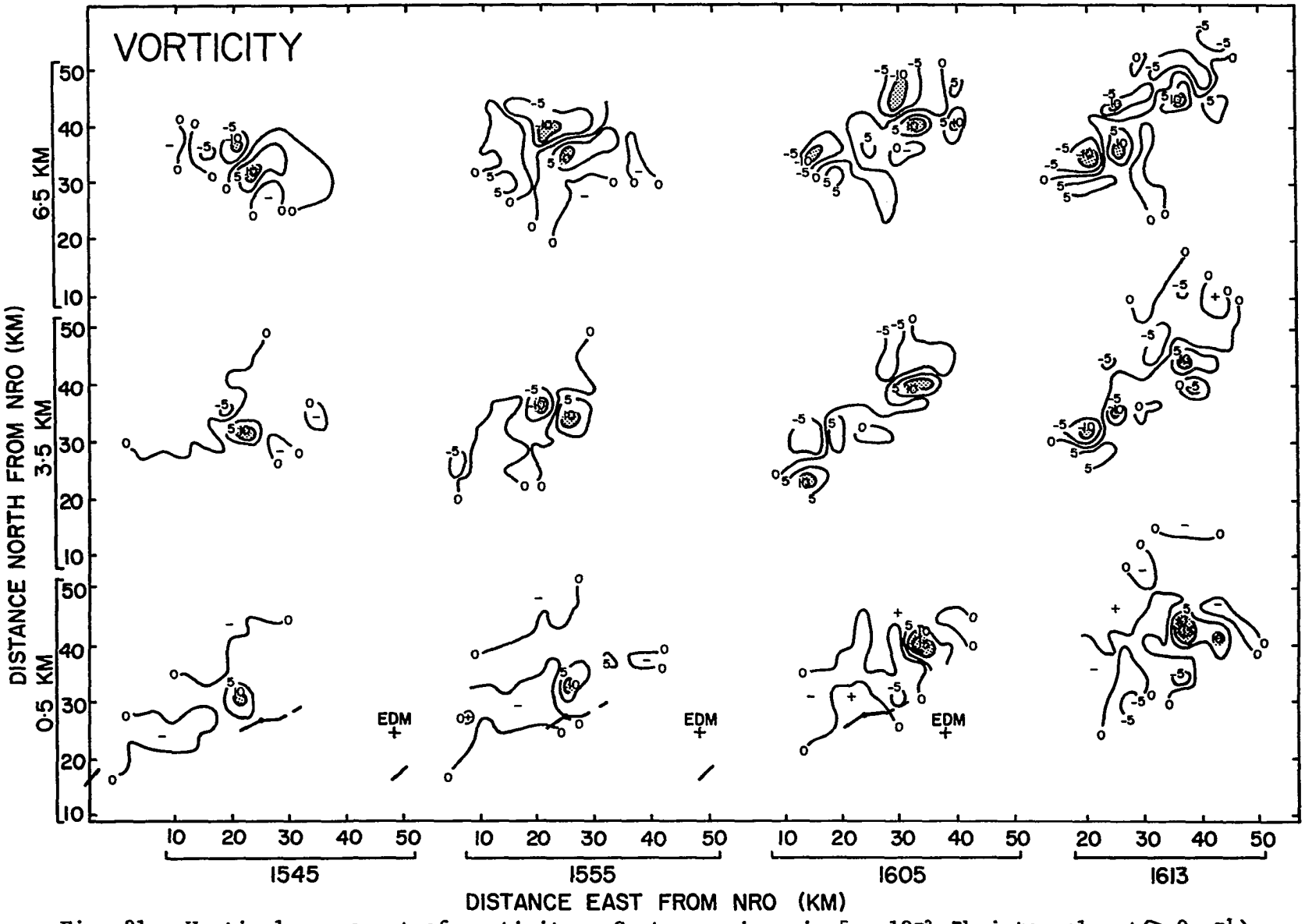

Fig. 21. Vertical component of vorticity. Contours given in 5 x 10^{-3} s^{-1} intervals; +(> 0 s^{-1}) and -(< 0 s^{-1}) are indicated.

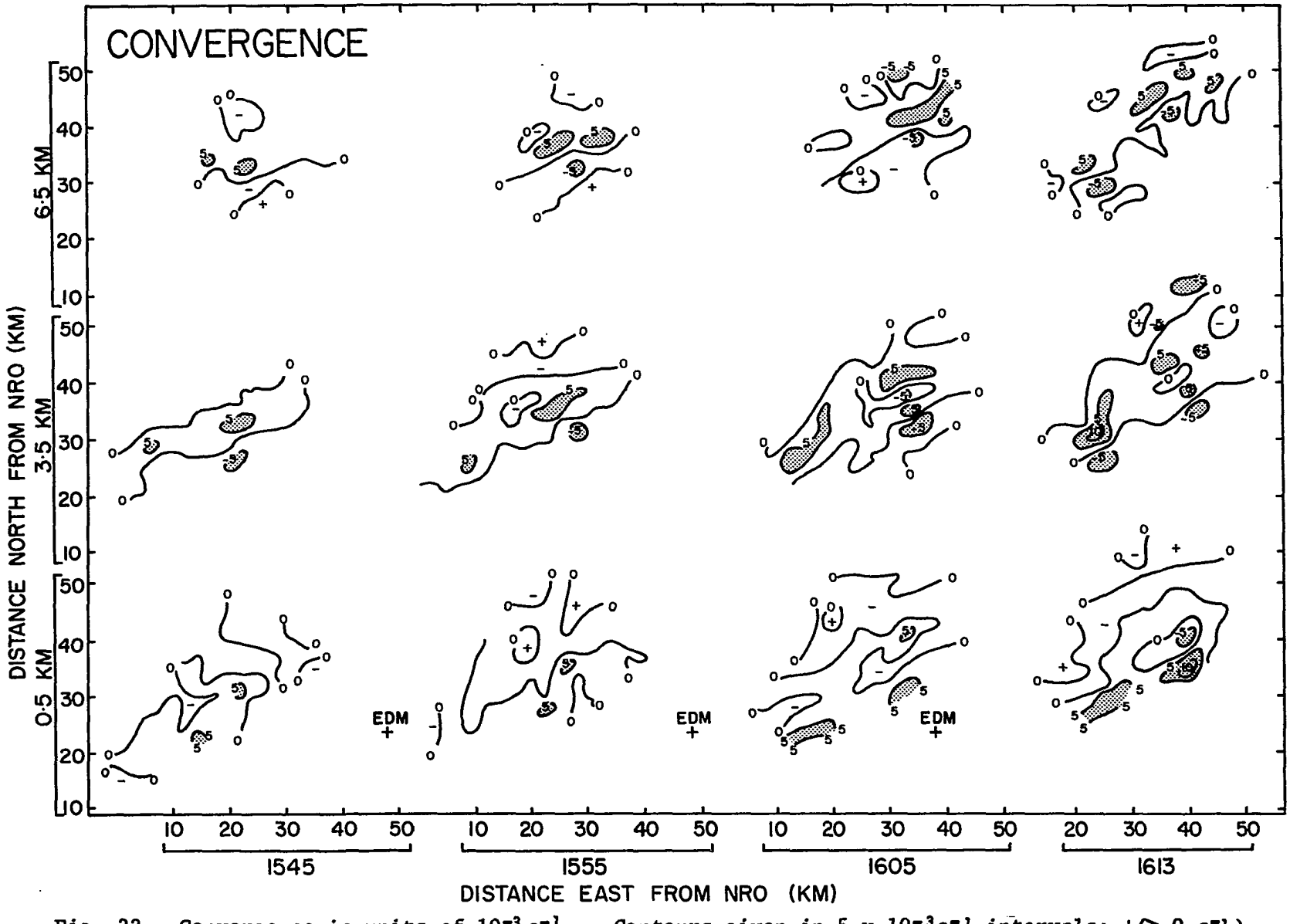

Fig. 22. Convergence in units of $10^{-3}\,s^{-1}$. Contours given in 5 x $10^{-3}s^{-1}$ intervals; +(> 0 s^{-1}) and -(< 0 s^{-1}) are sometimes indicated.

major storms A and B are evident by the high reflectivity regions greater than 50 dBZ (Fig. 18, 6.5 km) separated by about 20 km and a barrier flow at mid-levels (Fig. 19, 6.5 km). The cells with highest cloud tops during the analysis time are A_1, B_1, and B_2. Cell A_1 is studied in most detail, and was first observed on radar as a hook echo around 1530. The origin and early stages of this storm are difficult to determine since it formed in the radar ground clutter. The first time analyzed is 1545 when cell A_1 is a mature storm. After 1605, cell A_1 begins to dissipate, while cell A_3 is first observed at about 1605. Cell B_2 entered the dual Doppler region before 1545 and begins to dissipate by 1613. Upper level data were not available for this storm before 1605. The main observational results for the analyzed horizontal fields are now summarized, with most attention given to cell A_1 of the Harrah storm.

Reflectivity (Fig. 18)

i) Low-Levels (0-2.5 km): Along the right flank, WER are observed for cells A_1, B_1 and B_2 having reflectivity gradients of as large as 5 dBZ km^{-1}. A hook echo is associated with cell A_1 from 1545 to 1605.

ii) Mid-Levels (2.5-6.5 km): After 1555, the maximum reflectivity for cell A_1 decreases to less than 55 dBZ and is subsequent to tornado formation. There are two regions of strong reflectivity gradients. On the rear of

storms A and B, reflectivity indentations persist in time and height; the maximum indentation occurs between 2-5 km with reflectivity gradients of as large as 8 dBZ km^{-1}. On the right flank of cell A_1, to the south-southeast of the highest reflectivity, a strong (6 dBZ km^{-1}) reflectivity gradient is present as seen at the 6.5 km level.

iii) At the two earlier times, high reflectivity at 6.5 km (greater than 55 dBZ) is situated over the hook echo at lower levels and is part of an echo overhang along the entire right flank.

Storm Relative Wind Vectors (Fig. 19)

i) Low-Levels: A strong inflow jet with speeds in excess of 35 m s^{-1} enters the right forward flank of cell A_1 and is associated with a strong tornado cyclone.[12] Fankhauser (1971) has also found this to be a favored location for inflow air. Crawford and Brown (1972) similarly find the inflow jet strongest at the eastern portion of the strong reflectivity gradient. A weaker tornado cyclone exists for cell B_1. On the left rear quadrant of the circulation of cell A_1, a speed minimum is present, suggesting a low-level stagnation region, while to the southwest of the inflow jet there is northwest and anticyclonic flow.

ii) Mid-Levels: Cells A_1 and B_2 appear to be inter-

[12]The wind vectors are sufficiently dense so that streamlines are not plotted. Air trajectories are inferred from streamlines by assuming the storm is quasi-steady.

acting since air at 3.5 km flowing around the right of cell B_1 flows around the left of cell A_1. A vortex doublet appears nearly centered on the reflectivity maximum for both storms at 6.5 km. A horizontal wind speed maximum of greater than 35 m s^{-1} exists along the right flank of cell A_1 at 3.5 and 6.5 km, while a speed minimum is evident on the left front flank of cell A_1 and also to the left of the large reflectivity (and updraft as will be discussed). Barrier flow is most evidenced by a weak stagnation point upwind, and a more obvious stagnation region downwind of cell A_1. A second wind maximum along the left flank exists about 20 km northwest of the previous one. Along the left front flank of cell A_1, the strong 6.5 km northwest flow at 1555 and 1605 is nearly perpendicular to the environmental winds.

iii) The wind speed maximum along the right flank and minimum along the left flank extend nearly vertically for all times; however, a strong directional vertical shear of approximately 90° ($d\vec{V}/dz \approx 10^{-2} s^{-1}$) occurs along the right flank between the low-level inflow jet and the mid-level environmental flow.

Vertical Motion (Fig. 20)

i) Updraft: Air enters into the updraft of cell A_1 via the low-level jet and tilts toward the left flank in a cross-wind direction at low and mid-levels at 1545 to 1605; the vertical component at 1613 is difficult to interpret

from this data. At mid-levels, the updraft is nearly centered on the strong cyclonic flow.

ii) Downdrafts: Downdrafts are observed on both the left and right flanks. The strongest downdraft occurs on the right flank of cell A_1, as is also evidenced by a strong (6 dBZ km^{-1}) reflectivity gradient above 3 km in this same region. Along both flanks air may become cooled from evaporation of descending precipitation in the low θ_w mid-level air. The 50 dBZ reflectivity region at 3.5 km is somewhat centered on the interface between the updraft and the left flank downdraft at 1545 and 1555, suggesting that considerable precipitation falls into this downdraft. At 6.5 km the reflectivity maximum for cell A_1 slightly overhangs the right flank of the storm.

Vorticity and Convergence (Figs. 21, 22)

i) Low-Levels: The magnitude of the convergence associated with cell A_1 ranges from 5 to 10 $\times$ $10^{-3}s^{-1}$. A cyclonic vorticity maximum, centered on the hook echo of cell A_1, increases with time from 10 to greater than 15 $\times$ $10^{-3}s^{-1}$, while an anticyclonic region to the southwest of the cyclonic maximum increases negatively to values larger than $-5 \times 10^{-3}s^{-1}$. The most intense cyclonic vorticity is about 5 km in diameter. The 1555 surface position of the Harrah tornado is located about 5 km southwest of the vorticity maximum in a region of weak vorticity. The TVS

(Burgess, et al. 1975) were obtained from the NRO and CMF radial velocity data as additional verification of strong vorticity regions. Though the TVS's were weak (a shear of about $3 \times 10^{-2}s^{-1}$) from both radars at 1605 and 1613, they nearly coincide with the low-level vorticity maximum. At 1545, only the NRO TVS (weak) coincides with the low-level vorticity maximum. A larger TVS (a shear of about $4.5 \times 10^{-2}s^{-1}$) occurred between the vorticity maximum and the surface position of the tornado at 1555. Perhaps this latter TVS is associated with the tornado. The small feature at 4.3 km in the Cimarron reflectivity scans (Fig. 5K) is noted as it is near this second TVS and may indicate a strong circulation.

ii) Mid-Levels: Divergence of about $5 \times 10^{-3}s^{-1}$ is found on the right and left flanks, while strong convergence larger than $5 \times 10^{-3}s^{-1}$ is found in the interior of the storm in association with the updraft of cell A_1. A vortex doublet is centered on the convergence center of cell A_1. The axis of the vorticity doublet is nearly perpendicular to the mid-level environmental winds in all cases; the cyclonic and anticyclonic vorticity maxima are of equal magnitude and about $10 \times 10^{-3}s^{-1}$. The strong anticyclonic vorticity is generally associated with the reflectivity indentation on the rear of the storm.

From the w and ζ fields, the translational speed of updrafts and cyclonic vorticity centers may be calculated.

Table 2 summarizes results for cell A_1. The positions of the cyclonic vorticity and updraft maxima were vertically averaged over the 1 km interval to 7.5 km. The 1613 updraft position is not included since it is difficult to distinguish the updraft maximum at this time. The updraft moves at about 14 m s^{-1} from 230°-235°. Although this calculation is not independent of the $\vec{S}$ assumed, the values agree reasonably closely with the $\vec{V}_s$ assumed in the interpolation scheme. The vorticity center speed is considerably more variable and is observed at 1555 to move to the right of the straight line path between the vorticity centers at 1545, 1605 and 1613. This is consistent with the TVS observations, and appears to be associated with the tornado occurrence, or evolution of cell A_3 at 1555.

Vertical Cross-Sectional Analysis at 1555

The three-dimensional structure of cell A_1 at 1555 is studied in more detail in this section since the vorticity equation terms are evaluated for this same data, and the Harrah tornado is at the surface at this time. Fig. 23 shows y-z (Sections 6-10) and x-z (Sections 1-5) vertical cross-sections from 0.5 to 7.5 km altitude for: (a) v,w (Sections 6-10) and u,w (Sections 1-5) relative winds, (b) reflectivity, (c) vertical component of relative vorticity, and (d) convergence. The positions of these cross-sections are shown in Fig. 18. The x-z sections are nearly parallel to the mean tropospheric wind direction and thus represent

TABLE 2

TRANSLATIONAL MOTION OF UPDRAFT AND CYCLONIC VORTICITY MAXIMUM OF CELL A_1

	Time	x (km)	y (km)	u ($m\ s^{-1}$)	v ($m\ s^{-1}$)	Speed ($m\ s^{-1}$)	Direction (°)
UPDRAFT	1545	38.5	25.5				
				13.2	-4.5	13.9	238.8
	1555	46.4	22.8				
				13.8	-2.8	14.1	231.5
	1605	54.7	21.1				
VORTICITY	1545	38.0	23.5				
				8.5	-1.3	8.6	228.8
(cyclonic)	1555	43.1	22.7				
				15.7	-3.3	16.0	231.9
	1605	52.5	20.7				
				11.0	-1.5	11.1	227.4
	1613	57.8	20.0				

a lateral section through the inflow jet, for example. The y-z sections are nearly parallel to the inflow jet. The isotachs of the wind component transverse to the cross-section are contoured in Fig. 23 for a representation of three wind components. The shading indicates the transverse wind flows out of the page. The approximate surface position of the tornado is indicated by $\overline{V}$ in Sections 2 and 6.

The reflectivity fields and vertical motion fields are closely related through microphysical processes such as precipitation growth and evaporation, and the suspension of these particles in the vertical motion field. The reflectivity field therefore provides some qualitative information about the air flow in the storm. It is interesting to note the relation of the reflectivity maximum to the updraft of cell A_1. A WER is observed to correspond to this updraft in Sections 3 and 8. A strong inflow jet of nearly 30 m s^{-1} (Section 2) gradually slopes upward feeding cell A_1 with low-level warm moist air. The width of the jet using the 20 m s^{-1} v isotach is approximately 6 km and the depth, about 2.5 km. The jet maximum (Sections 1, 2) is located above the surface at about 1.5 km, perhaps due to surface friction in the boundary layer. An echo overhang along the right flank is observed at higher levels in Section 8 above this jet. There is a strong potential for mid-level air to be evaporatively cooled above 2-3 km in this overhang region,

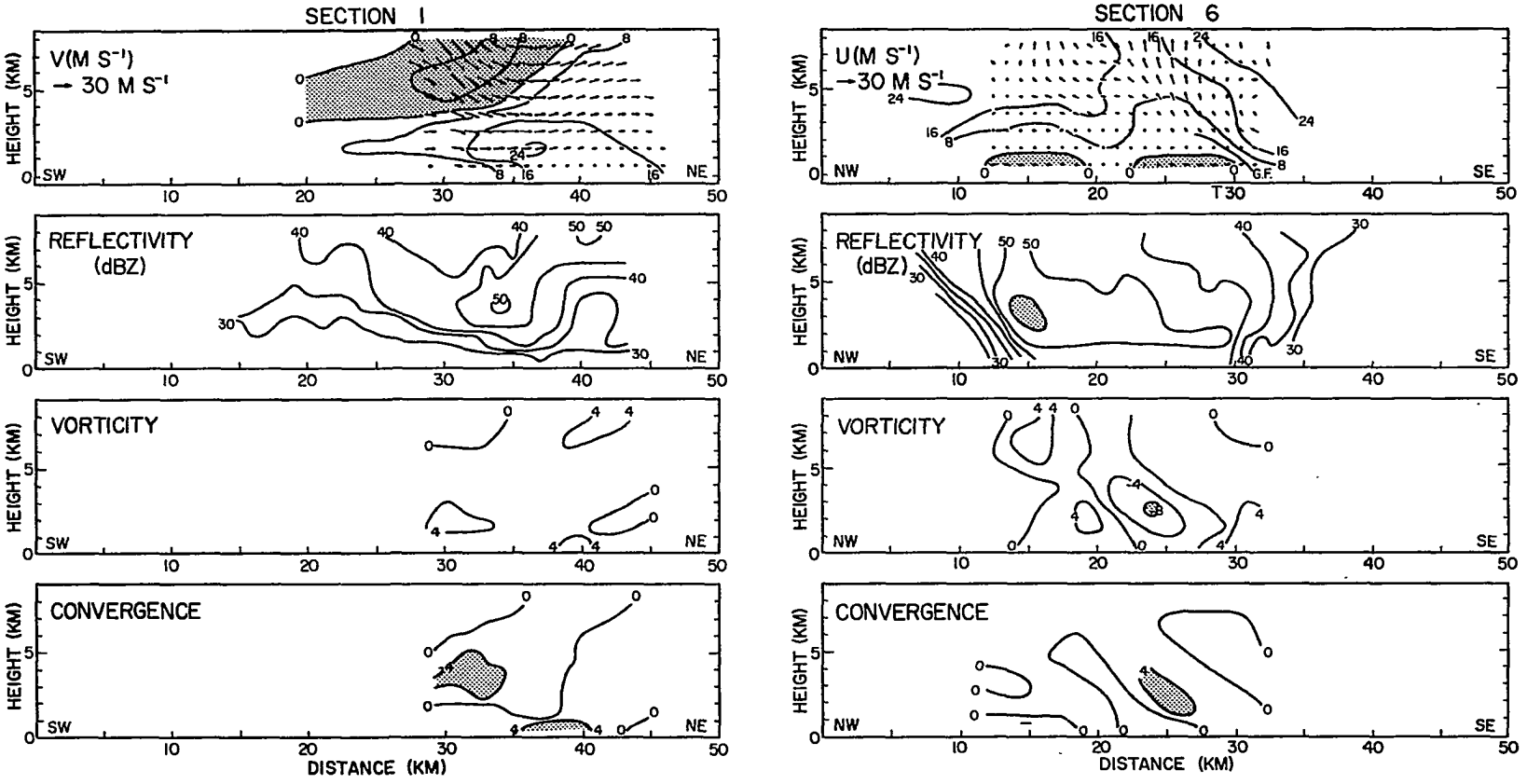

Fig. 23. Vertical cross-sections for 1555. Positions of sections are given in Fig. 18. The vertical scale is slightly larger than the horizontal scale (1·25:1). Winds in plane of cross-section less than 4 m s^{-1} are indicated by a dot, and missing data is omitted. Flow out of page is shaded. The approximate surface position of the tornado at 1555 is indicated by $\mathcal{V}$ and suggested gust front by G.F. Units of vorticity and convergence are in 10^{-3} s^{-1}.

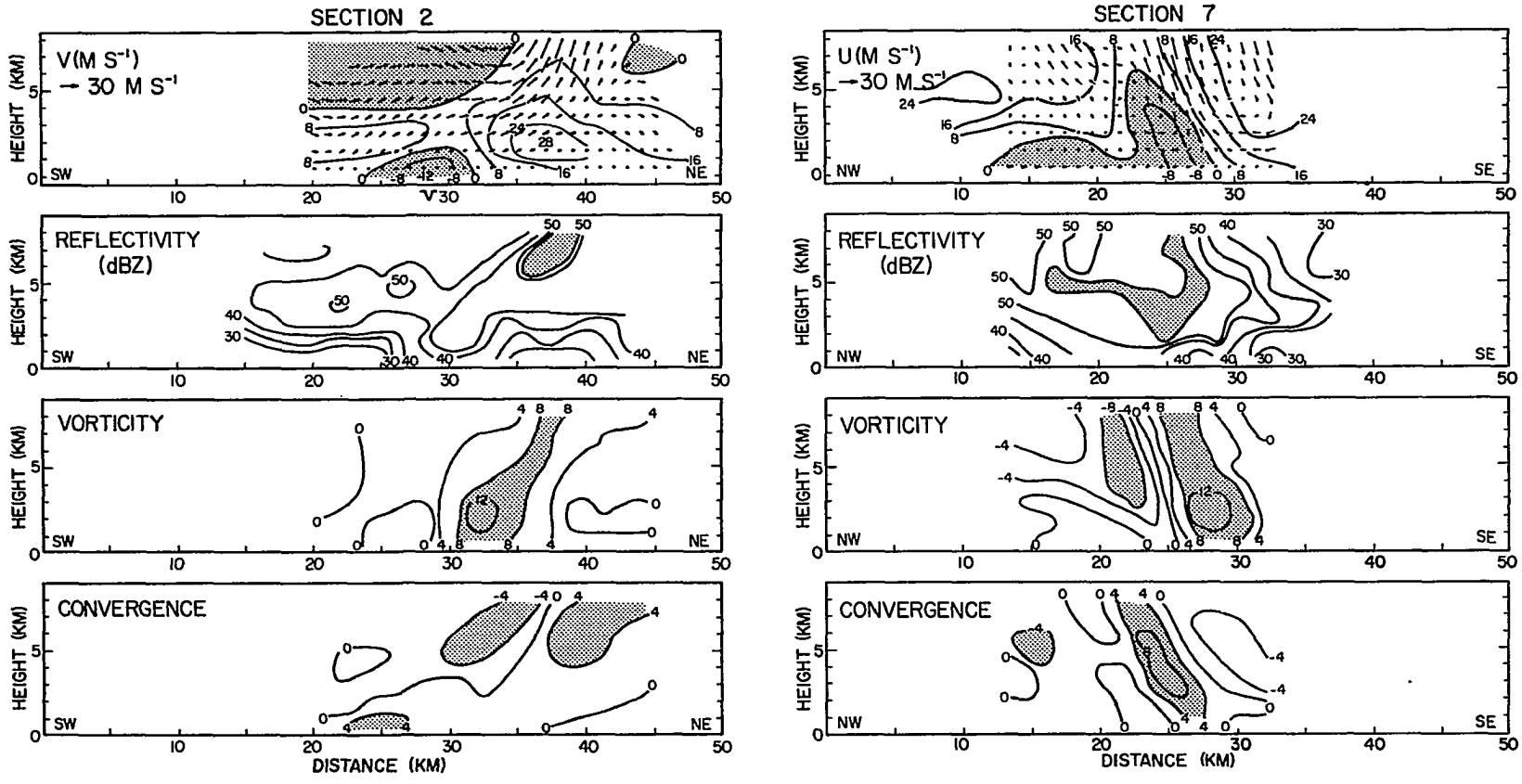

Fig. 23 (continued).

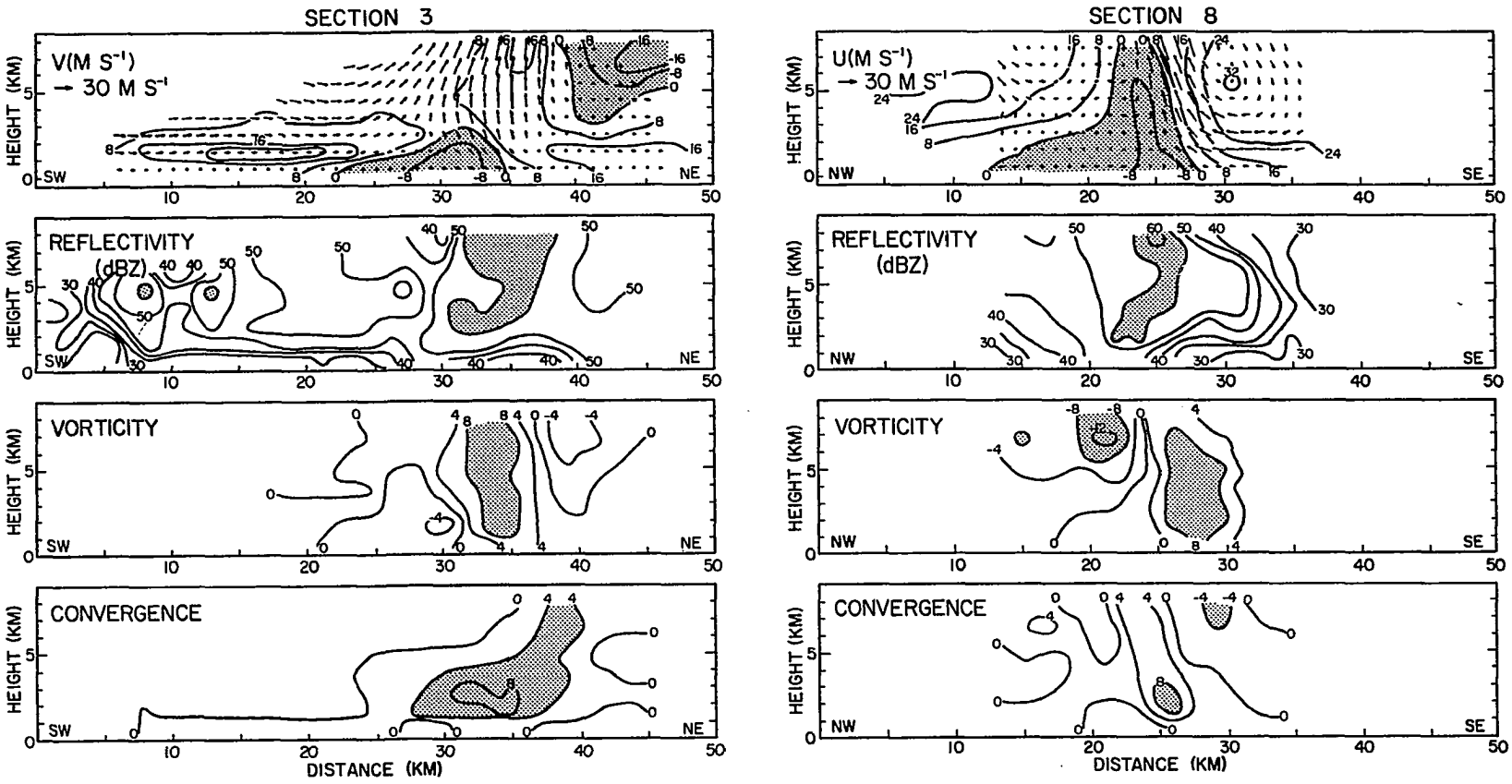

Fig. 23 (continued).

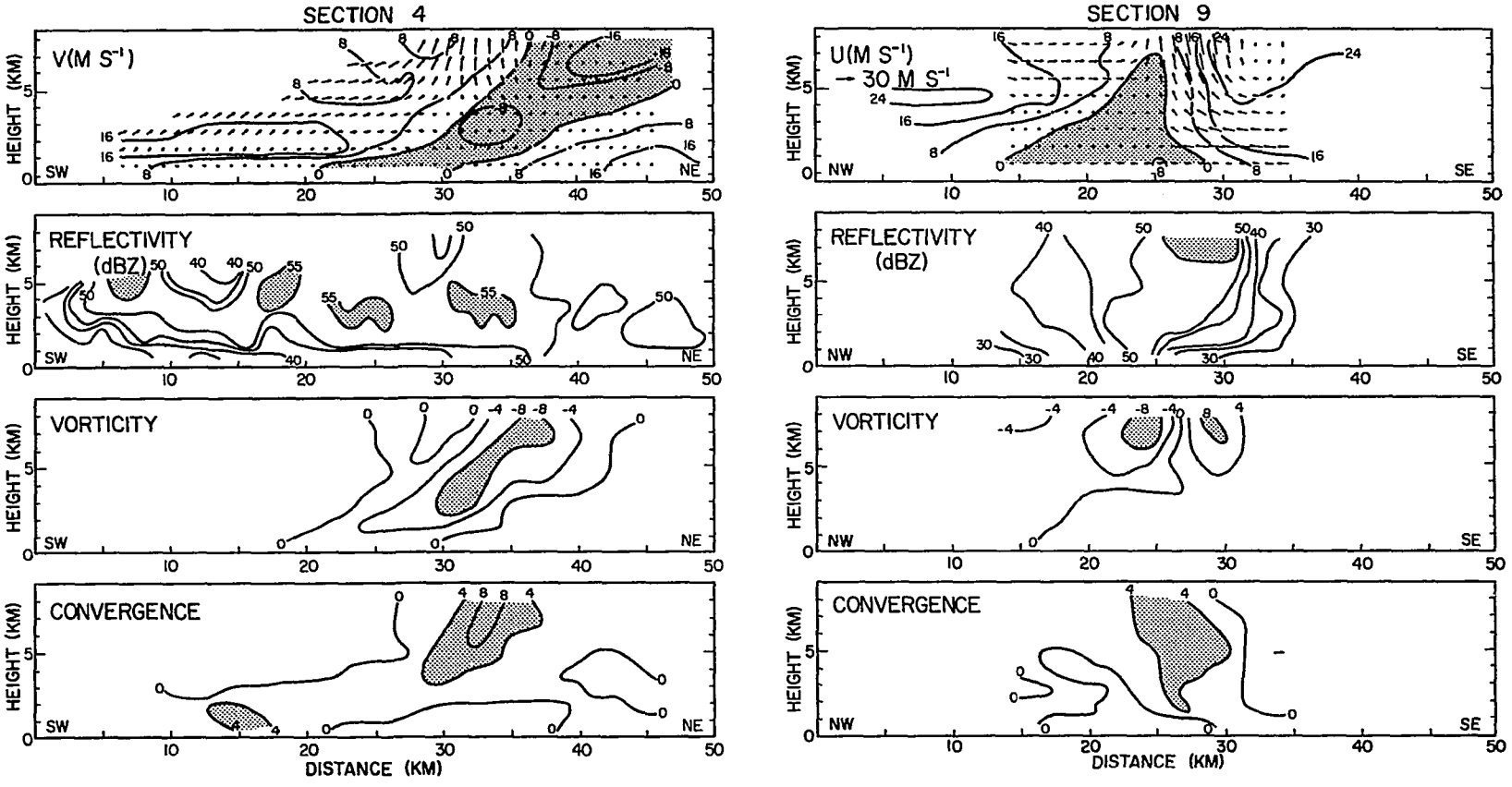

Fig. 23 (continued).

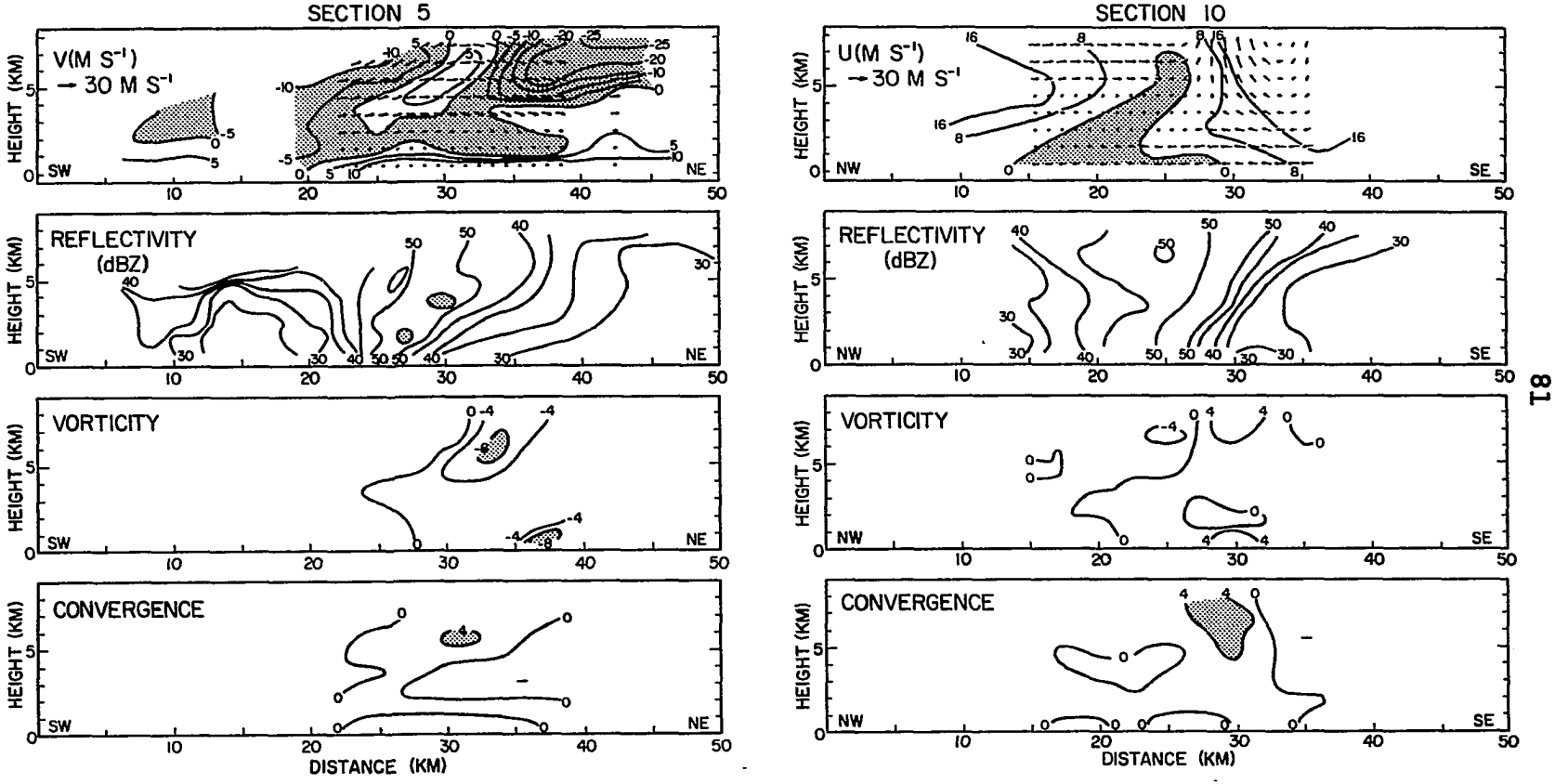

Fig. 23 (continued).

providing an impetus for the strongest downdraft (Section 1) observed on the storm's right flank. On the left storm flank, a weak downdraft is evident (Section 8) at lower levels. Section 4 suggests that a large portion of the air for this downdraft originates from environmental flow along the storm's left flank as seen by the large negative v at mid-levels. In Section 6, there appears to be a surface stagnation point due to this downdraft air. In Section 8, there is a precipitation shaft of greater than 55 dBZ originating at about 7.5 km (-20°C) and terminating in this downdraft. It originates from a region of strong vertical velocity of about 30 m s^{-1}. It should be noted that the overhang and precipitation shaft correspond to the Browning and Foote (1975) so-called embryo curtain and hail cascade regions.

A gust front formed by the outflow is suggested in the observations. In Section 6, the lowest levels indicate a wind discontinuity shown by G.F., while outflow is seen in Section 2, by $v < 0$ at low-levels. This wind discontinuity is also evident after 1545 in the horizontal wind vectors given in Fig. 19. Cell A_3 may exist prior to 1555, but is not resolvable in the analyzed fields. The deduced 1555 position of cell A_3 is above the outflow, nearly coincident with the 1555 tornado position.

Barrier effects are evidenced by a wind maximum along the storm's right flank and a stagnation region downwind of

the updraft. In Section 8, the u component on the storm's right flank is 32 m s^{-1} at 6.5 km, decreasing downward. In Section 3, a mid-level stagnation region is found nearly downwind from the updraft. Since the storm relative environmental winds at 6.5 km are approximately 20 m s^{-1}, there is clearly an increase in wind speed around the storm core at mid-levels. In Sections 6, 7, and 8, a velocity minimum ($u < 0$ m s^{-1}) exists along the left flank and a second wind maximum ($u \simeq 25$ m s^{-1}) exists 20 km northwest of the first. Both the updraft-downdraft couplet and the high reflectivity region seem to act as obstacles. The strong cyclonic vorticity of cell A_1, as noted previously, does not completely coincide with the updraft at mid-levels. There is however, significant overlap--the updraft being more northward. The vorticity maximum slopes north with height, approximately 30° from the vertical, as was similarly observed from the other analysis times. The anticyclonic region is strongest along the left flank above about 3.5 km, and correlates well with the downdraft air which reaches the surface along the left rear flank. In Sections 9 and 10, mid-level air enters this downdraft above 5.5 km at the left front flank with flow into the storm of about 20 m s^{-1}. This flow is clearly seen in Fig. 19 at 6.5 km and 1555. A strong ($u < -8$ m s^{-1}) northeast flow, in a direction opposite the environmental winds is found between the vortex centers (Section 7) along the storm's left flank.

The observations suggest that the updraft is rotating. If solid body rotation is assumed for simplicity, then $v_\theta = \bar{\zeta}a/2$, where v_θ is the tangential wind component, and $\bar{\zeta}$ is mean vorticity over a region of radius a. From Section 8 in Fig. 23, $\bar{\zeta} \simeq 8 \times 10^{-3} s^{-1}$ and a $\simeq$ 2.5 km resulting in v_θ = 10 m s^{-1}. Assuming an average vertical motion of 20 m s^{-1} in the updraft core, the air flows tangentially and ascends at an angle of approximately 60° from the horizontal. At this same radius, air ascending from the surface to 10 km would make approximately 1/3 a revolution. This simple calculation may lend support to the Browning (1965) model in which the air turns cyclonically 270° in the updraft.

The convergence fields correlate well with the vertical motion fields. The convergence center of cell A_1 slopes in a northerly direction with height, as evidenced in Sections 2, 7, and 8. Divergence exists above and below the sloped region of convergence. Although the analysis is sensitive to the advection velocity $\vec{S}$, the vertically integrated divergence would tend to zero with this configuration.

The horizontal and vertical shears of the transverse wind component are readily interpreted from the vertical cross-sections. Large horizontal gradients of the transverse wind component indicate strong horizontal shears, while large vertical gradients indicate strong vertical shears. Along the right flank, strong vertical shears

(Section 1) are found in the environmental flow while strong horizontal shears (Section 2) are found in the vicinity of the inflow jet. In Section 2, strong vertical shear, $\partial\vec{V}/\partial z$, exists above outflow air (computed as approximately $1.6 \times 10^{-2}s^{-1}$) and also above and below the inflow jet (computed as approximately $1.0 \times 10^{-2}s^{-1}$), as also observed from v isotachs. Inside the updraft (e.g., Section 8), strong horizontal shears perpendicular to the mid-level winds are present. Parallel to these winds, above the inflow jet, the ridge of v component inside the updraft (Section 2) indicates vertical transport of southerly momentum. The vertical wind shear throughout the storm complex is greater than $10^{-3}s^{-1}$, with values as large as $2 \times 10^{-2}s^{-1}$.

Recall that vorticity, ζ, may be separated into terms due to shear normal to the flow and curvature of the flow. The strong cyclonic vorticity at low-levels (i.e., tornado cyclone) associated with the inflow jet is most likely due to shear vorticity, resulting from the interface between cold air outflow and the inflow jet. It is similarly suggested that the mid-level vortex doublet is associated with shear vorticity. Along the right flank of the storm (Section 8), a speed maximum exists perhaps due to a barrier effect, while on the northwest side of the updraft, it will become more obvious that the speed minimum results from the downdraft structure.

Precipitation Trajectories

Precipitation trajectories are computed from the 1555 winds to further examine the downdraft structure. The storm is assumed steady state over the time (approximately 5 min) it takes a raindrop to descend to the surface from its starting point. The raindrops are assumed to move horizontally at the horizontal wind speed, without growth or evaporation, and to move vertically at a rate $dz/dt = w+v_T$, where $v_T = -10$ m s^{-1} is the terminal velocity of an extremely large raindrop or a small hailstone. Precipitation would thus descend when $w < -v_T$, and ascend if $w > -v_T$. With these assumptions, the storm relative winds are used to examine the precipitation trajectories for cell A_1. Fig. 24 shows precipitation trajectories computed by integrating downward from level to level. The starting points for selected trajectories are 4.5 and 7.5 km.

The strongest downdraft and speed maximum was observed along right flank. Precipitation particles descending in this region reach the surface on the front flank of the storm. This path closely relates to the reflectivity structure (e.g., Section 9) where the higher reflectivity slopes over this descending air. The echo indentation at mid-levels at the right front flank of cell A_1 previously noted in the horizontal sections would correspond to the region where the precipitation turns cyclonically toward the left front flank. The indentation is perhaps due to

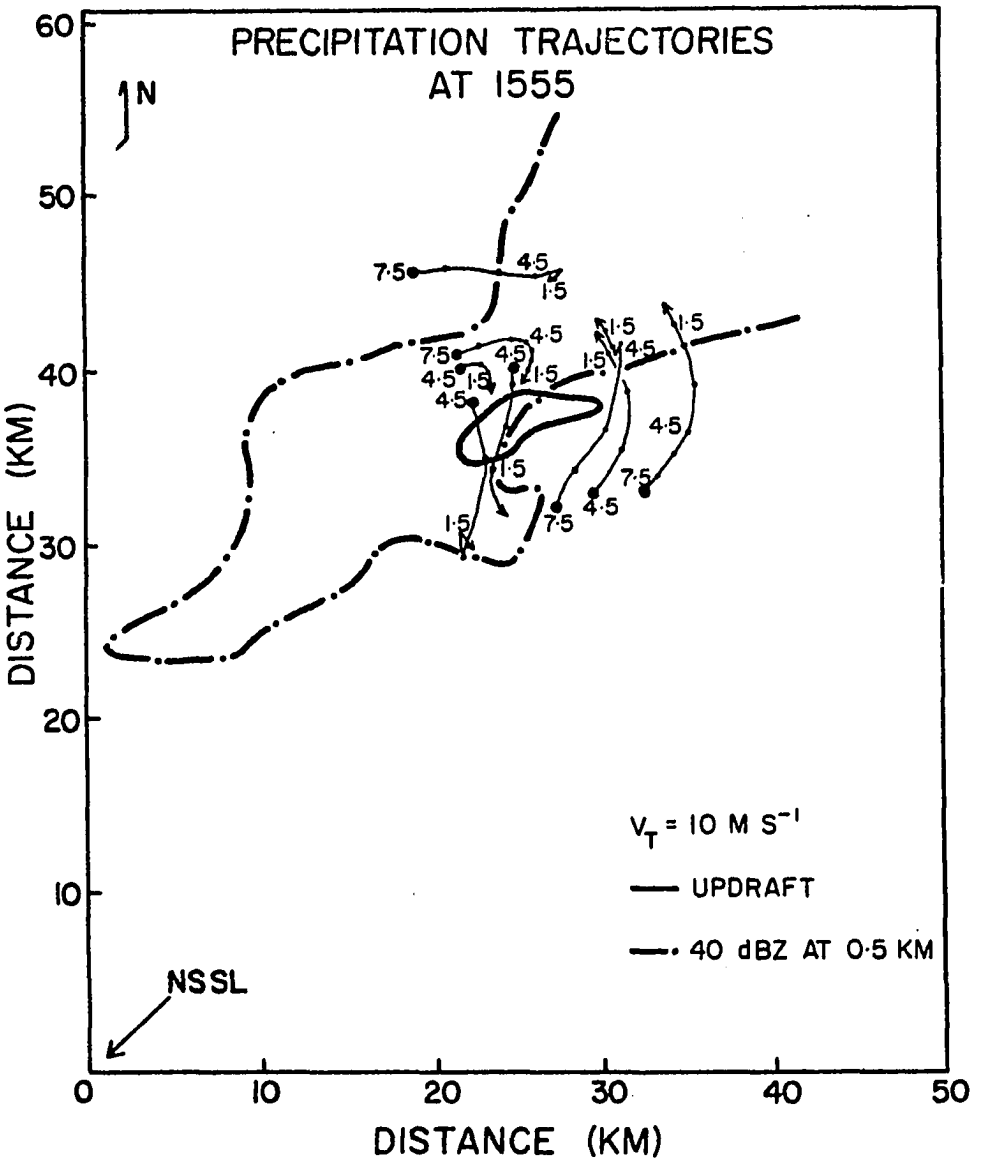

Fig. 24. Trajectories of hydrometeors computed for 1555, assuming a fall velocity of 10 m s^{-1} . Superposed is low-level 40 dBZ contour (thick dashed curve) and 25 m s^{-1} updraft core at 6.5 km (thick curve). Large dots indicate beginning of trajectory; all heights given in kilometers above the surface.

the evaporation of precipitation by low θ_w mid-level air.

The tilt of the updraft has an important effect on precipitation trajectories. A diagram (Fig. 1) given by Kessler (1975) illustrates this point. Particles with large v_T entering the sloped updraft column from the upwind side, exit the edge of the updraft column on the downwind side. This would correspond to the northwest of the updraft in Section 8, Fig. 23. The precipitation trajectories suggest particles move across the updraft, fall into the anticyclonic downdraft, and undercut the tilted updraft, to form a hook echo. Although no hail were reported at the surface from the Harrah storm, the large reflectivities (>60 dBZ) and strong vertical velocities, suggest hail were present. Suppose hail with a terminal velocity of 30 m s^{-1} falls out of the tilted updraft. Since a horizontal velocity minimum exists north-northwest of the updraft, hail would fall nearly vertically, as is also verified by trajectory calculations (not shown). This is the region of the storm where hail at the surface is typically reported. It is noted that the observed hook echo in Fig. 24 coincides with the low-level positions of the tagged raindrops falling out of the updraft.

Time Variation of Cells

Fig. 17 is a synthesis of the cell locations from 1545 to 1613. While cells A_1 and B_1 appear to be supercells

as evidenced by their three-dimensional airflow, new cells form along the right and right rear flanks of these cells, similar to what is expected for a multicell storm. Although 1545 was the earliest time studied, cell A_1 was observied back to at least 1536 (see Fig. 5B) when the hook echo was first observed. Cell A_1 does not undergo significant changes at 1545 or 1555, but dissipates after 1605. Fig. 25 presents vertical reflectivity cross-sections for 1545, 1605, and 1613 in which the approximate locations of cells A_1 and A_3 are shown. The positions of these sections are given in Fig. 18, while Fig. 23 gives similar cross-sections for 1555.

Cell A_1 appears to be weakening at 1605 (Section DD'), since the maximum reflectivity has decreased considerably from 1555, and there is no longer an obvious weak echo region. The inflow jet is still however about 30 m s^{-1} at 1605 and 1613. Cell A_2 is evident in Fig. 20 as a weak updraft, and is located about 11 km northwest of cell A_1. The role of this cell is not well understood, except that it is a secondary cell. Cell A_3 was first clearly detected at 1605 at approximately 5.5 km or -5°C. It is interesting to note, however, that this cell may have existed prior to 1555. In Fig. 5K, a small hook echo exists at 4.3 km which may be associated with this cell and the tornado. Cell A_3 formed in the vicinity of the low-level outflow in Section 2 (Fig. 23) above the surface tornado track. It is seen to

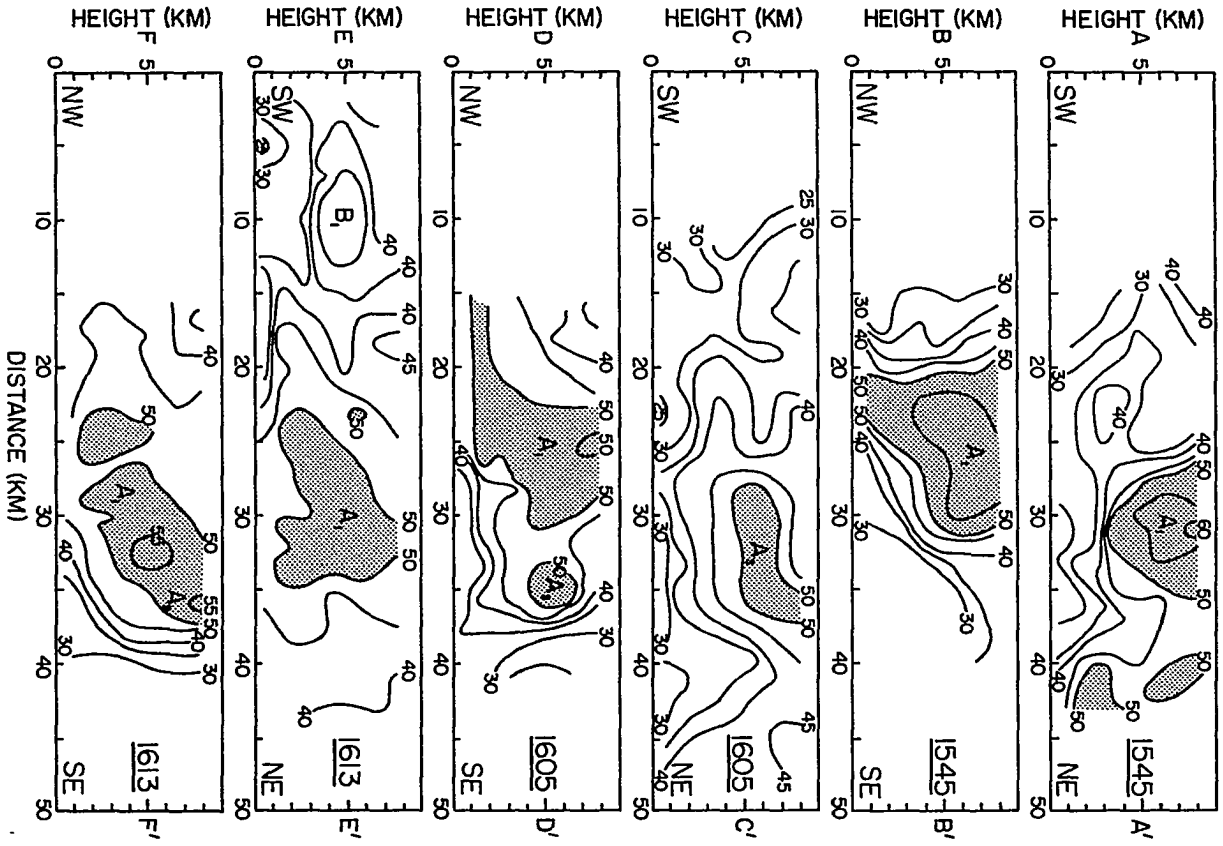

Fig. 25. Vertical reflectivity cross-sections. The positions of the sections are indicated in Fig. 18.

intensify at 1605 about 6 km southeast of cell A_1 in Sections DD' and FF' in Fig. 25. The updraft associated with this cell is also noted in Fig. 20 at the later times. Cell A_3 may have formed as a flanking cumulus cell, initiated by mechanical lifting of low-level air by the outflow. Recall that at 1545 cell A_1 has strong reflectivity aloft and a weak downdraft along the left flank. During the later times, the downdraft along the left flank intensifies which would increase surface outflow. The increased outflow may reduce inflow to cell A_1 and also provide a larger lifting of low-level air along the right rear flank.

Storm B formed about 15 km southwest of storm A. Cell B_1 first formed in the radar ground clutter sometime before 1530. It is a mature cell from 1545 to 1605, and then weakens as seen in the horizontal reflectivity analysis (Fig. 18). Cell B_1 appears to have similar flow characteristics to cell A_1. Similar to cell A_1, the mid-level reflectivity pattern at 1605 and 1613 has large indentations on both storm flanks. Also note the strong mid-level vortex couplet (Fig. 21) associated with this storm, and similar wind vectors (Fig. 19). Cell B_2 is a mature cell throughout the data collection.

The initiation and morphology of storms A and B suggest some difficulty in applying the conventional classification of multicell or supercell. The primary cell studied was A_1 which appears to have many characteristics

of a supercell. Although cell A_1 was originally thought to be part of a multicell storm complex at the analysis times, it has a highly three-dimensional airflow rather than a two-dimensional airflow suggested in previous multicell studies. Cells B_1 and B_2 have been combined into storm B due to their close proximity. There is some difficulty in applying the conventional storm classifications to these storms as they exhibit new cell growth and highly three-dimensional character, simultaneously.

Summary of Airflow in the Harrah Storm

Previous investigations have suggested that the updraft acts to block the environmental flow. Newton and Newton (1959) make the analogy of an updraft in a veering-shearing environment, to a cylindrical barrier. Charba and Sasaki (1971) and others suggest the cylinder is rotating, providing a mechanism for storm deviation by Magnus type forces. Connell (1975) suggests the analogy of a jet in a crossflow, which characteristically has a vortex doublet, entrainment in the lee, and a wake region.

Fig. 26 is a composite figure of the Harrah storm at 1555 and 6.5 km altitude to facilitate comparisons to the above models. The symmetry of the internal structure at mid-levels is nearly perpendicular to the relative wind, as in the case of the vortex doublet. Significant overlapping of the cyclonic rotation on the updraft exists, sug-

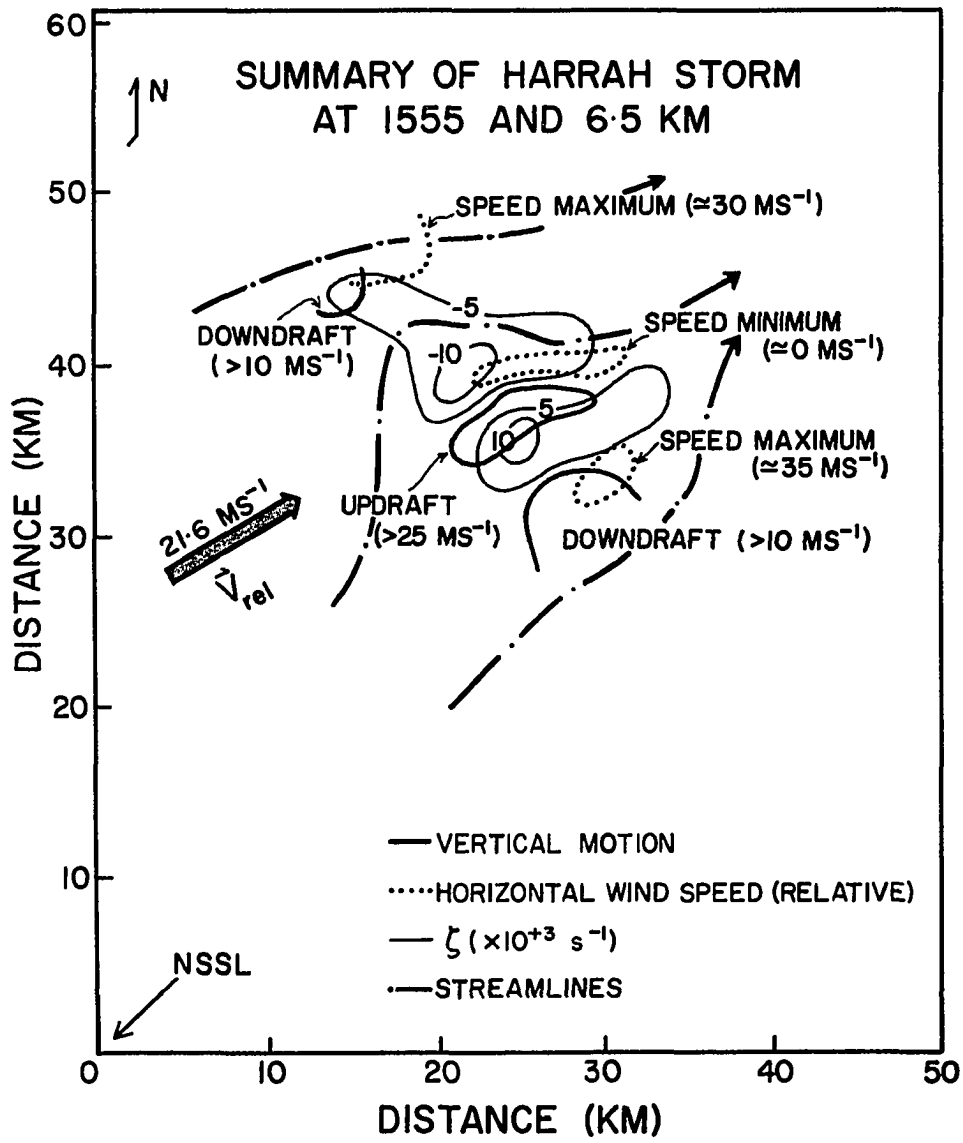

Fig. 26. Horizontal view of the Harrah storm at 1555 and 6.5 km.

gesting a rotating updraft. The strongest downdraft occurs along the right flank, a second weaker downdraft (not shown) occurs to the left of cell A_1, while a third downdraft may be associated with cell A_2. A speed maximum (about 13 m s^{-1} greater than environmental winds) and minimum surround the updraft, along the right and left flanks, respectively. A second speed maximum exists 20 km northwest of the first. It is mentioned that Fujita and Grandoso (1968) found wind maxima separated by about 25 km using aircraft, with the one along the right flank slightly larger. Fankhauser (1971) similarly observed wind maxima on both storm flanks, with a stagnation region downwind of the updraft. The highest reflectivity region (not shown) is situated over the hook echo at lower levels, and nearly coincides with the updraft at mid-levels.

If the updraft was analogous to a cylindrical barrier, the wind maxima surrounding the updraft would be 31 m s^{-1} and 43.2 m s^{-1} at 3.5 km and 6.5 km, respectively. The observations have a wind maximum approximately 30-40 m s^{-1} along the right of the updraft, while a wind minimum less than 5 m s^{-1} exists to the left and forward of the updraft (facing downwind). This analogy is not supported by the observations. The data would at first seem to support a jet model (e.g., Connell, 1975), but the storm structure is indeed more complicated. Recall (Fig. 1) that characteristic features of a jet in a crossflow are a vortex doublet, entrainment of environment air downwind of the updraft, and

a stagnation region. Figs. 23 and 26 suggest the anticyclonic vorticity region in the Harrah storm is in a weak downdraft, while the vortex doublet surrounds the updraft in the jet model. Though the wind speeds are possibly explainable by analogy to a rotating cylinder, the reason for only one wind maximum will become more apparent from the three-dimensional airflow structure (also see Appendix A).

The Harrah storm is more in agreement with airflow in supercell storms, rather than with multicell storms (e.g., Browning et al. 1976), which have more of a two-dimensional character. There is some evidence that a flanking line of cumulus clouds may exist as suggested by Lemon (1974). The main features of the airflow associated with the Harrah storm are summarized in Fig. 27a,b while Fig. 27c gives a simplistic representation of the vorticity distribution. Fig. 27a is a summary of the three-dimensional airflow at 1555, where the inflow jet (J), mid-level air (solid bands), descending precipitation (open circles), tornado ($\forall$), and gust front (barbed line) are shown. At low and mid-levels, the updraft tilts in a direction nearly perpendicular to the mean tropospheric winds, due to the vertical advection of the low-level southerly momentum. The downdraft originates from mid-level environmental air. The strongest downdraft is on the storm's right flank. This air may eventually reach the ground along the left front flank due to momentum mixing with the low-level southerly

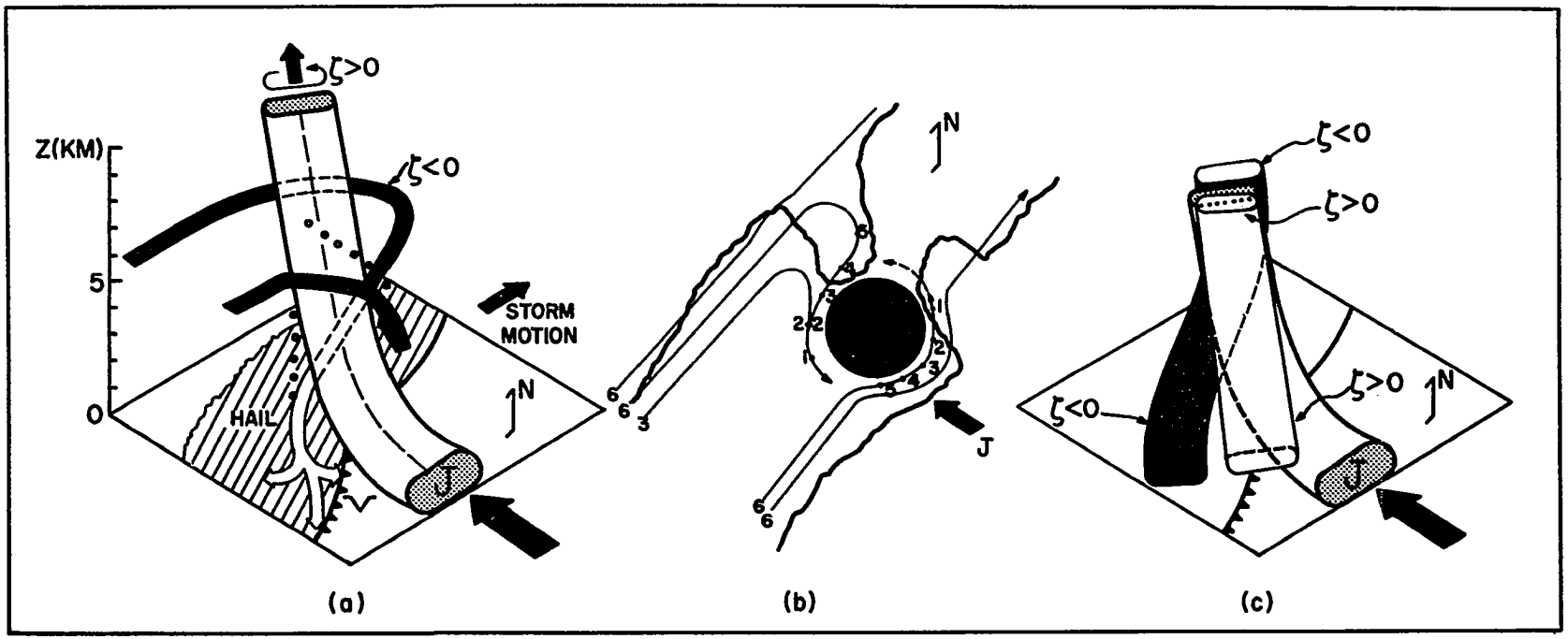

Fig. 27. A summary of the Harrah storm structure: (a) three-dimensional representation, (b) projection of descending mid-level air on horizontal plane, and (c) simplistic representation of the vorticity distribution. J indicates the low-level inflow jet. In (a), hatching at the surface indicates precipitation; small dots are hail and precipitation trajectories. In (b), paths of several mid-level air trajectories are shown, with altitudes in kilometers approximately indicated. The dashed portion of the trajectory along the left front flank indicates that the downdraft air may become mixed with low-level flow.

flow. Downdraft air also originates from environmental flow along the storm's left flank, turns anticyclonically, undercuts the tilted updraft, and forms a gust front. It is particularly noted that the left flank downdraft flows in an opposite direction to the environmental winds.

Fig. 27b shows approximate downdraft flow trajectories. The updraft is shaded and the mid-level 30 dBZ contour is indicated. The reflectivity indentations correspond to mid-level dry intrusion on the front flank of the storm. The dashed trajectory indicates that the descending air along the right flank may become mixed with low-level southerly flow. This is also shown by the solid line in Fig. 27a, which separates a region of mixed air (lower potential temperature) to the northwest of warmer moist low-level air.

Fig. 27c summarizes the vorticity observations corresponding to the airflow in Fig. 27a. The shaded tube is a region of strong anticyclonic vorticity, while the nearly vertical tube is strong cyclonic vorticity. Significant overlap of the cyclonic vorticity on the inflow jet and updraft exists. The anticyclonic vorticity is smallest near the surface and increases by nearly an order of magnitude with height. The observations suggest that the low-level tornado cyclone exists between the low-level inflow jet and the descended mid-level air. At mid-levels, the vortex doublet is oriented perpendicular to the relative wind direction and is associated with the shear vorticity

resulting from the anticyclonic downdraft.

The differences between the airflow structure in the Harrah storm and those studied by Browning (1965) and Fankhauser (1971) is in the downdraft's origin. They suggest the strongest downdraft is on the left forward flank which differs from the right rear flank of cell A_1. The left flank downdraft is similar to the anticyclonic downdraft suggested by Kropfli and Miller's (1976) observations, and also with Danielson's (1975) conceptual model. The right flank downdraft resembles the Browning (1965) model, however his model does not have downdraft air originating from mid-levels along the left flank. The trajectories of precipitation particles would be quite similar to Browning's speculations. Section 8 in Fig. 23 remarkably resembles Fig. 15.7 in Browning's report. A clue to the origin of this downdraft is also given by Browning, who suggested evaporative cooling due to precipitation falling from upper levels out of a cyclonically turning (over the right flank) updraft. In this connection, Kessler's (1969) steady state solutions for the case of a strong updraft has implications on the above.[13] According to his theory, particles above the updraft maximum have long residence times and are prevented from descending to the surface beneath the updraft column. Three-dimensional divergence of the rising air would be balanced by moisture condensation, while three-

---

[13]Strong updrafts are defined by $w >> v_T$.

dimensional divergence is a more dominant process in the upper troposphere. Since the water content is nearly independent of updraft speed, he suggests that the strong updraft would tend toward a steady value (non-oscillatory) governed by a balance of drag, buoyancy and water load forces. Thus even though larger particles may fall out of the tilted updraft, considerable water content is available to become divergent at higher levels of the storm, eventually sustaining a downdraft along the storm flanks as suggested by Browning (1965).

The vortex doublet in Fig. 26 appears to result from a cyclonically rotating updraft and an anticyclonic downdraft. This differs from the vortex doublet centered on the updraft as suggested by Kropfli and Miller (1976), and also computed in the Schlesinger (1975) numerical cloud model. Kropfli and Miller's data has an anticyclonic downdraft, but they suggest the doublet is due to barrier flow. Possibly at higher levels in the Harrah storm, there is a vortex doublet due purely to barrier flow. The downdraft structure suggested may offer an explanation for the Burgess, et al. (1975) observations in which the tornado cyclone appeared at the ground at least 8 min prior to the tornado. As the TVS descended, low-level vorticity increased. Thus, it is possible that the downdraft also played an important role in their observations.

CHAPTER V

IMPLICATIONS OF THE VORTICITY EQUATION ON STORM STRUCTURE

In this chapter the airflow associated with cell A_1 is examined physically. Some interesting questions are: (1) What produces an anticyclonic downdraft? (2) What is the importance of the strongly sheared region between the low-level inflow jet and mid-level environmental flow? (3) Is the tornado produced by concentration of ambient vorticity? Recall from Chapter IV observations that: i) a strong inflow jet and circulation existed at low-levels, ii) along the right flank of the storm, a downdraft exists which curves cyclonically into the front flank of the storm perhaps mixing with the more southerly ambient winds at lower levels, and iii) along the left storm flank, the southwest flow at mid-levels turned anticyclonically to northeast flow at low-levels. In the core of the updraft, vertical transport of low-level southerly momentum was evident with much stronger horizontal shears than vertical shears. The complexity of the observations suggest that cell A_1 acts as a dynamical entity, with interaction between the updraft, microphysics and storm environment. To

examine this interaction, low and mid-level vorticity production is evaluated with the vorticity equation.

Vorticity Equation-Background

The vorticity equation provides an expression relating changes in vorticity to physical processes. On the synoptic scale, the vorticity equation may be simplified from the full equation to form one basis for weather prediction. On the smaller scale of a severe storm, mechanisms are much more complex due to the strong vertical motion field, which implies considerably less horizontal stratification.

The vorticity equation is derived by performing the operation ($\vec{k} \cdot \nabla_h \times$) on the vector form of the full equation of motion. The rate of change of absolute vorticity following the motion, $d\zeta/dt$, is given by

$$d\zeta/dt = \partial\zeta/\partial t + \vec{V} \cdot \nabla (\zeta+f) + w\partial\zeta/\partial z$$

$$(1) \qquad (2) \qquad (3)$$

$$= -(\zeta+f)\nabla \cdot \vec{V} + \vec{k} \cdot (\partial\vec{V}/\partial z \times \nabla w). \qquad (23)$$

$$(4) \qquad (5)$$

$$-\vec{k} \cdot (\nabla\alpha \times \nabla p) - K_H\nabla^2\zeta - \partial/\partial z(K_z\partial\zeta/\partial z$$

$$(6) \qquad (7) \qquad (8)$$

where ζ is the vertical component of relative vorticity, $\vec{V}$

is the horizontal velocity, w is vertical velocity, f is Coriolis parameter, K_H is the horizontal eddy exchange coefficient (assumed constant), K_z is the vertical eddy exchange coefficient (assumed a function of z only), α is specific volume ($= 1/\rho$), p is pressure, and ∇ is horizontal gradient. The terms in (23) have the following physical interpretation: 1) local time rate of change of relative vorticity, 2) horizontal advection of absolute vorticity, 3) vertical advection of relative vorticity, 4) divergence term, 5) twisting or tilting term, 6) solenoidal term, 7) horizontal turbulent production of vorticity, 8) vertical turbulent production of vorticity. The tilting term represents the rate of conversion of horizontal vorticity into vertical vorticity resulting from differential vertical advection. The solenoidal term results from pressure torque on moving particles. The divergence term represents production of vorticity by convergence.

To determine the importance of the terms in the vorticity equation, a scale analysis similar to Holton (1972) is performed. The horizontal and vertical length scales are estimated from the autocorrelation functions in Chapter III. Recall that for the radial velocity ACF given in (15), the integral scales were $L_x = L_y \simeq 4$ km, and $L_z \simeq 1.5$ km. Using these values as typical, the remaining scale parameters are estimated from surface, radar and aircraft observations and are shown in Table 3. The scale analysis would be most ap-

TABLE 3

SCALE PARAMETERS FOR STORM SCALE

PARAMETER		MAGNITUDE
L	(characteristic horizontal scale)	4×10^5cm
D	(characteristic vertical scale)	$1{\cdot}5 \times 10^5$cm
V	(characteristic horizontal velocity)	2×10^3cm s^{-1}
W	(characteristic vertical velocity)	10^3cm s^{-1}
L/V	(characteristic period {advective period})	2×10^2s
δp	(horizontal pressure fluctuation)	10^4dynes cm^{-2} (10 mb)
$\delta\rho/\rho$	(fractional density fluctuation)	10^{-2}
ρ	(density)	10^{-3}gm cm^{-3}
K_H, K_Z	(eddy coefficients)	$10^6 cm^2 s^{-1}$
f_0	(Coriolis parameter at 35° N)	$10^{-4} s^{-1}$
β	("Beta" parameter at 35° N)	10^{-13}cm s^{-1}

plicable to the individual updraft or tornado cyclone. The pressure perturbation of 10 mb, may be considered an an upper limit and is based on surface pressure drops (e.g., Fujita, 1963) associated with mesolows. A characteristic value for the eddy diffusivities is given, however, this parameter is quite variable and not well understood in severe storms. In the theoretical cloud model by Hwang and Lin (1973), for example, values of 10^6 cm^2 s^{-1} for K_z and K_H, respectively were used. The tornado vortex studies by Morton (1966) and Golden (1974) used an eddy diffusivity of 10^6 cm^2 s^{-1}. This order of magnitude has also been found from aircraft observations (e.g., Pinus and Litvinova (1962)).

The order of magnitude of individual terms in the vorticity equation are given in Table 4. For comparison, the largest terms for mesoscale fields (L ≃ 100 km) are of order $10^{-8}s^{-2}$ and are three orders of magnitude less than for the storm scale. The most important terms are the local change, advection, divergence, and tilting terms. The solenoidal term has been dropped as it is two orders of magnitude less than other terms. From this scale analysis, the approximate vorticity equation for the storm scale is

$$d\zeta/dt = \partial\zeta/\partial t + u\partial\zeta/\partial x + v\partial\zeta/\partial y + w\partial\zeta/\partial z \tag{24}$$

$$\simeq -\zeta(\partial u/\partial x + \partial v/\partial y) + (\partial w/\partial y\ \partial u/\partial z - \partial w/\partial x\ \partial v/\partial z).$$

TABLE 4

MAGNITUDES OF TERMS IN VORTICITY EQUATION

	Individual Terms	Magnitude	Estimate of Magnitude (s^{-2})
TOTAL DERIVATIVE	$\partial\zeta/\partial t$, $u\partial\zeta/\partial x$, $v\partial\zeta/\partial y$	$\leq V^2/L^2$	2.5×10^{-5}
	$w\partial\zeta/\partial z$	$\leq WV/LD$	3.3×10^{-5}
	$v\partial f/\partial y$ $(= v\beta)$	$V\beta$	2×10^{-10}
DIVERGENCE	$f(\partial u/\partial x + \partial v/\partial y)$	$\leq f_0 V/L$	5×10^{-7}
	$\zeta(\partial u/\partial x + \partial v/\partial y)$	$\leq V^2/L^2$	2.5×10^{-5}
TILTING	$(\partial w/\partial y\ \partial u/\partial z - \partial w/\partial x\ \partial v/\partial z)$	$\leq WV/LD$	3.3×10^{-5}
SOLENOIDAL	$1/\rho^2\ (\partial\rho/\partial x\ \partial p/\partial y - \partial\rho/\partial y\ \partial p/\partial x)$	$\leq \delta\rho\delta p/\rho^2 L^2$	6.3×10^{-7}
TURBULENCE	$K_H \nabla^2 \zeta$	$\leq K_H V/L^3$	3.1×10^{-8}
	$\partial/\partial z(K_z \partial\zeta/\zeta z)$	$\leq K_z V/L^2 D$	8.3×10^{-8}

The rate of change of absolute vorticity following the motions ($d\zeta/dt$) is given by the sum of the divergence and tilting terms.

In the following, only the non-advective divergence and tilting terms are evaluated, whose sum is defined as $d\zeta/dt$. Recall in Chapter III the crude estimate of a time scale of 5.5 min assuming stationarity and the Taylor hypothesis. The vorticity tendency ($\partial\zeta/\partial t$) has not been evaluated due to the large time interval between data sets (10 min). It is also not possible to evaluate the solenoidal and eddy terms with radar data since these require thermodynamic and microscale data.

Computations of Vorticity Equation Terms

The wind fields previously analyzed are used for the evaluation of the non-advective terms (tilting and divergence) in the vorticity equation. The grid-spacings were similar to those previously utilized ($\Delta x = \Delta y = \Delta z = 1$ km). The derivatives were evaluated using centered differences. Presented in Fig. 28 are vertical cross-sections of the divergence term, the tilting term, and the sum of divergence and tilting terms ($d\zeta/dt$), corresponding to Sections 2, 3, 4, 7, and 8 in Fig. 23. The discussion again concentrates on cell A_1 at 1555 when the tornado has already formed, and the vorticity structure is quite intense.

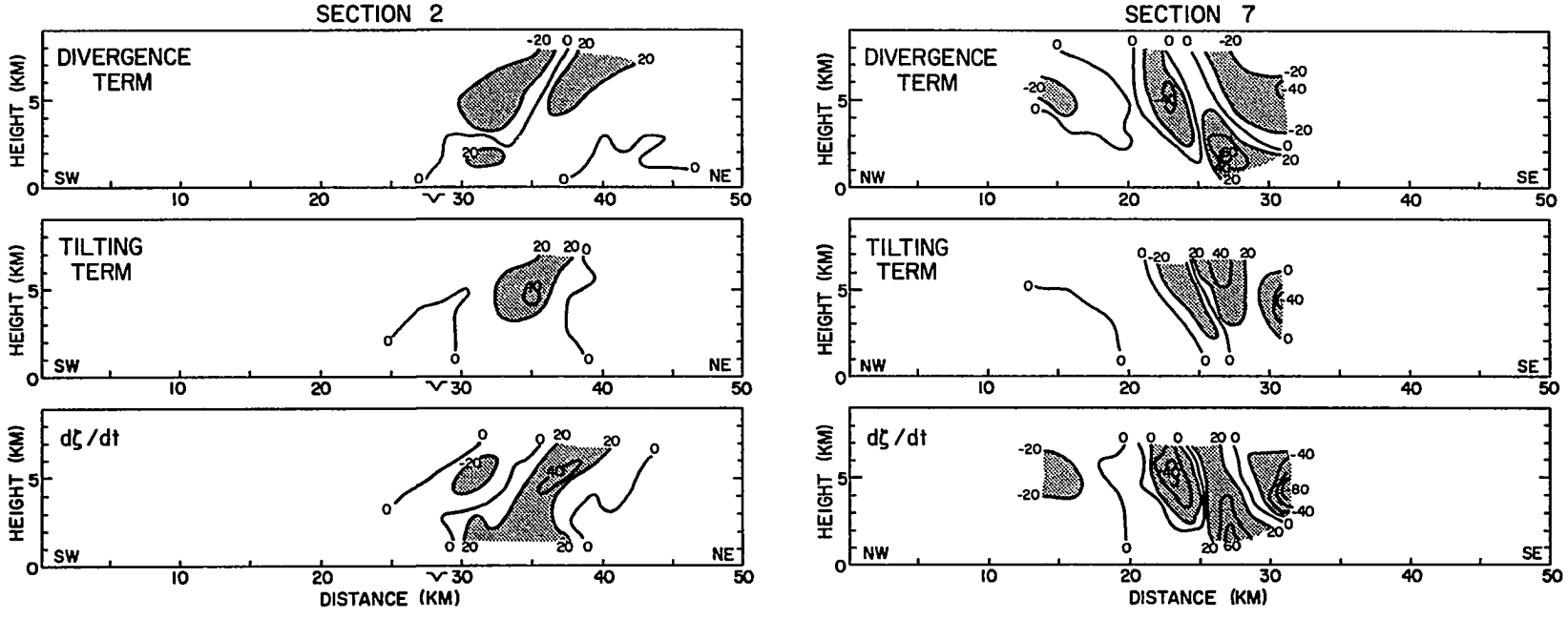

Fig. 28. Evaluated divergence, tilting, and sum of divergence plus tilting terms for selected vertical cross-sections in Fig. 23. The surface position of the tornado is indicated by ▽ in Section 2. Units are in $10^{-6}\,s^{-2}$.

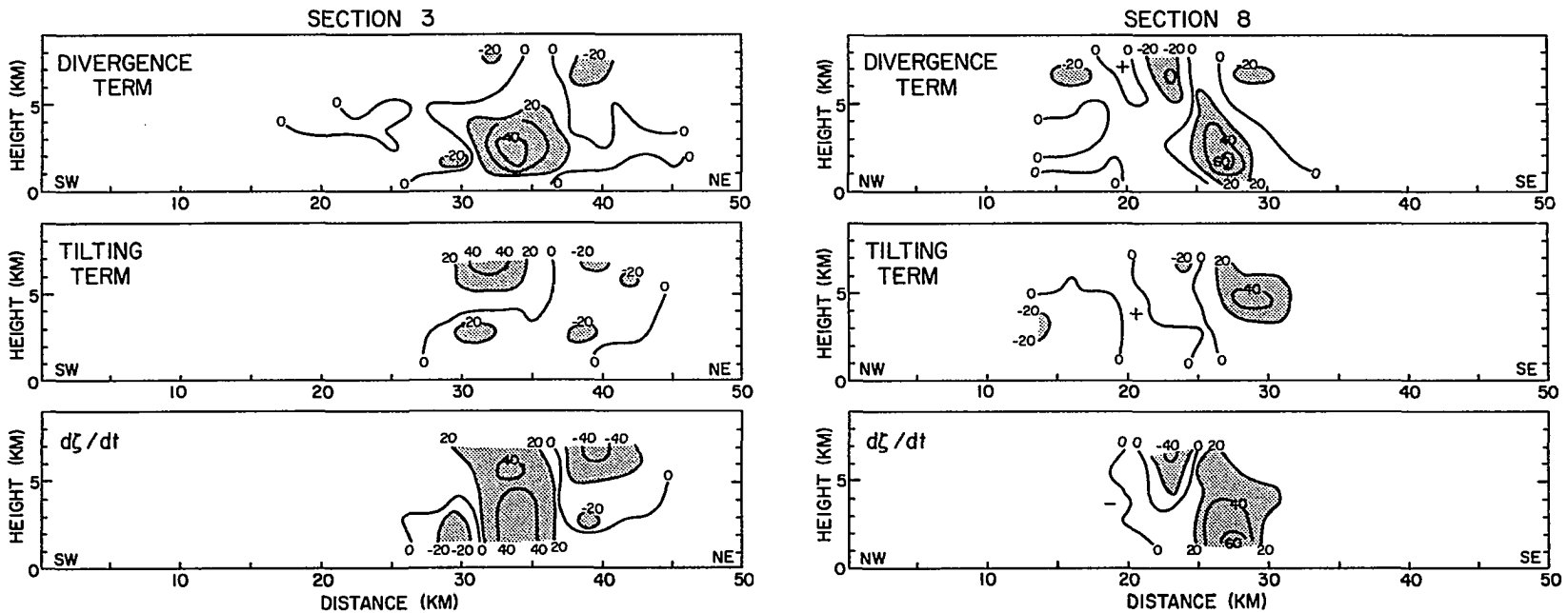

Fig. 28 (continued).

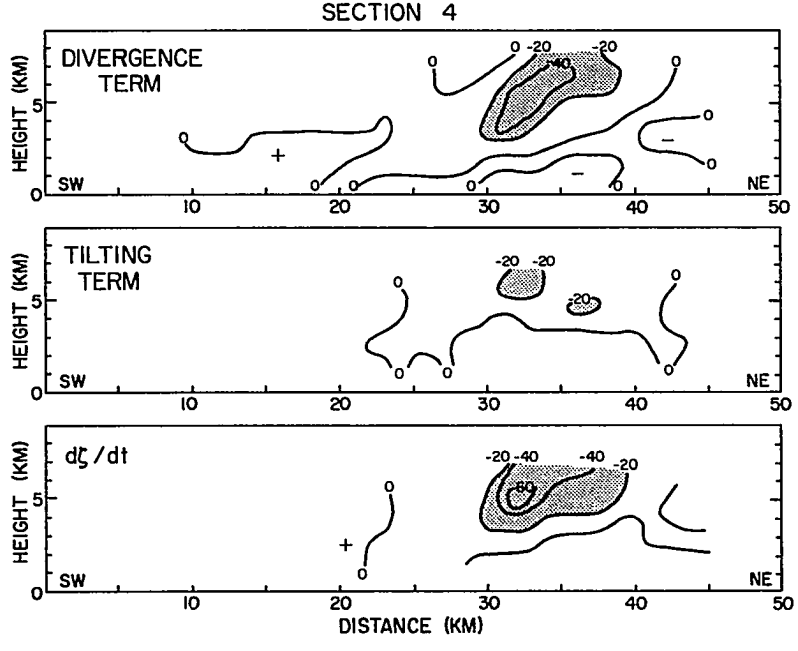

Fig. 28 (continued).

Errors in evaluating the terms are due to observational errors in u, v, and w and are also due to the inability of finite difference approximations to represent sub-grid scales. Since u, v, and w have inaccuracies, caution should be taken in quantitative interpretation. This calculation is not expected to resolve vorticity production associated with tornado initiation, since it is perhaps a sub-grid scale phenomenon, or has been smoothed out.

The divergence term becomes important in intensifying pre-existing vorticity. It is largest (positive) at low-levels, beneath the tilted updraft (Sections 3 and 8), or in the northern part of the low-level vorticity center. The maximum positive vorticity production was $60 \times 10^{-6} s^{-2}$. The observations suggest that low-level convergence intensifies the tornado cyclone. At mid-levels, regions of negative vorticity production by divergence (approximately $-20 \times 10^{-6} s^{-2}$) surround the updraft. The largest negative divergence term is on the right rear flank, and it is not strongly positive at mid-levels. It is noted that the product of vorticity and convergence in Figs. 21 and 22 give the divergence term. The centers of convergence and vorticity are more nearly coincident at 1545, suggesting also a large positive divergence term.

The tilting term shows largest positive production at mid-levels along the right flank (Sections 2,3), and has a maximum value of $40 \times 10^{-6} s^{-2}$, while negative production by

tilting ($\simeq -20 \times 10^{-6} s^{-2}$) exists along the right rear flank (Section 7) and along the left storm flank (Section 4). Barnes (1970) suggested that tilting of horizontal vorticity along the right flank of the storm may be important in storm rotation. Schlesinger (1975) found similarly in a diagnostic computation from his three-dimensional numerical model that vorticity was intensified by tilting along the right flank, and also anticyclonic vorticity was generated along the left flank. He suggested that this resulted from the updraft penetrating a sheared environment which produces strong ∇w and $\partial u/\partial z$. Along the right flank of the Harrah storm, the vertical shear ($\partial v/\partial z$) is quite large ($\simeq 10^{-2} s^{-1}$) above the inflow jet as are horizontal gradients of vertical velocity (∇w). Thus, cyclonic vorticity associated with the updraft appears to be intensified due to tilting of horizontal vortex tubes. On the left flank, the anticyclonic flow associated with the downdraft may be intensified by tilting, eventually causing the mid-level air to make a gradual turn and nearly reverse direction as shown in Fig. 27.

The total derivative $d\zeta/dt$ in Fig. 28 indicates that both the divergence and tilting terms are important in vorticity production. Strong anticyclonic vorticity production in the downdraft along the left flank and cyclonic production in the updraft and along the right flank are indicated. Anticyclonic production along the right rear flank which in sufficient time would tend to divert mid-level air (see

Section 2, Fig. 23) toward the southeast or out of the page. Further downstream, this air would then be turned cyclonically by the positive vorticity along the right flank and by ambient winds. From the time sequence of vorticity in Fig. 21, $d\zeta/dt$ of approximately $\pm 20 \times 10^{-6} s^{-2}$ is suggested by the movement of the vortex doublet from one time to the next. This is within the same order of magnitude as the sum of the divergence and tilting terms computed.

Fig. 29 summarizes qualitative results of the vorticity equation. Fig. 29a gives a vertical cross-section corresponding to Section 8. The u component is perpendicular to the plane of the figure, and the approximate location of the updraft to the upper limit of 7.5 km is enclosed by thick solid lines. The v,w winds in the plane of the cross-section are indicated by arrows, and $|\zeta|$ greater than $8 \times 10^{-3} s^{-1}$ is shown. Fig. 29b gives the signs of the vorticity equation terms. The importance of the low-level inflow jet, and mid-level speed maximum along the right flank is clearly seen to intensify the vertical wind shear, and hence the tilting term. Along the left flank, the reversal in direction of mid and low-level flow in the downdraft concentrates vertical wind shear. Suppose in the earlier part of the storm lifetime, this downdraft intensified by evaporative cooling from precipitation falling out of a tilted updraft. This would intensify anticyclonic vorticity by the tilting term by first increasing

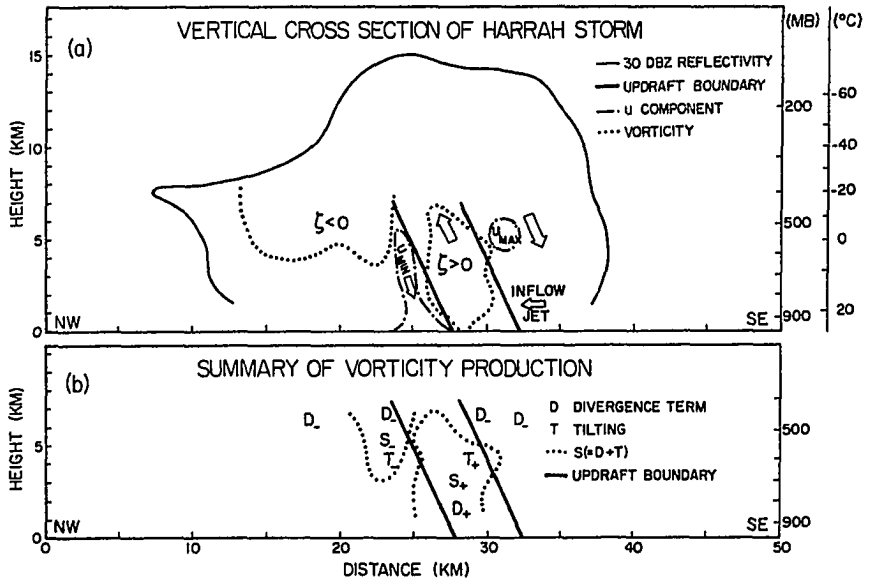

Fig. 29. Summary of vorticity equation terms from Harrah storm. The position of this cross-section correspons to Section 8 in Fig. 24. In (a), the wind flow in the same plane as the figure is indicated by arrows; isotachs of transverse winds less than -8 m s^{-1} (u_{min}) and greater than 30 m s^{-1} (u_{max}) are given. In (b), the signs of the tilting (T), divergence (D), and D plus T(S) are indicated by subscripts.

gradients of w. The mid-level flow reversal would then increase the vertical shear, and further intensify this vorticity. This vorticity production would sustain an anticyclonic downdraft along the left flank, and updraft rotation.

The source of strong vorticity production which resulted in the Harrah tornado is not apparent in the computations. The most notable feature associated with the approximate position of the tornado is the strong ($>10^{-2}s^{-1}$) vertical shear, $\partial v/\partial z$, above and at the leading edge of the outflow (Section 2). In view of the computational errors in the winds and the smoothing out of small scale features, strong vorticity production associated with the tornado is possibly explainable by the tilting term. The computation of vertical shear in the tilting term is more reliable than the horizontal gradient of vertical velocity, since the u,v winds are considerably more accurate than w. For example, if a $-5 \times 10^{-3}s^{-1}$ horizontal shear of w exists perpendicular to the outflow (e.g., along the left half of the outflow), the tilting term would be as large as $50 \times 10^{-6}s^{-2}$. A tornado with a vorticity $10^{-1}s^{-1}$ would be produced in about 30 min, if this outflow structure persisted over a long enough time. As the earlier 1545 data similarly had large vertical shear above the outflow, and the hook echo was first observed at 1536, this 30 min time scale is possible.

In conclusion, the storm-induced vorticity production is indeed large. Concentration of larger scale am-

bient vorticity at mid-levels does not appear essential in development of the mid-level vortex doublet. Both the divergence and tilting terms resulting from the storm structure are important and their magnitudes are sufficient to produce a tornado on a time scale comparable to the storm's early lifetime.

CHAPTER VI

SUMMARY AND CONCLUSIONS

The Harrah storm has been examined using a number of sources of data including WSR-57 and Doppler radar data, rawinsondes, aircraft, and a tornado damage survey. The primary emphasis is on the three-dimensional wind structure computed from the NSSL dual Doppler radar system.

The three-dimensional winds were computed from radial velocity observations interpolated to a uniform grid, and through use of the cylindrical continuity equation. The statistical interpolation scheme of Eddy and Gandin was applied to the radial velocity observations. Its use has given insight on the magnitudes of random noise in the observations, and on the accuracy of the interpolation. With these error estimates, a quantitative evaluation of the accuracy of the three-dimensional winds was made according to Doviak et al. (1976a). The interpolation errors are larger than suggested by Doviak et al. (1976a) since meteorological noise on scales larger than the pulse volume are included in the observation error. To reduce random errors and to focus attention on the storm scale, a low-pass grid

filter is employed. Other errors arise from the assumption of Taylor's hypothesis. The fact that different regions of the storm move with different motion vectors and the storm evolves over the data collection period weaken this assumption. Reduced scan times of the radars through the storm would help this latter problem. The analyzed fields were interpreted by a synthesis of data, taking into account that the u and v components have better accuracy than the w component

The synthesis of data suggests the Harrah storm was more in agreement with the supercell category of storms than that of a multicell storm. Detailed data was not available for the early storm evolution, and consequently the storm structure was well-established at the first (1545) analysis time. At 1545, strong ($>10^{-2}s^{-1}$) vorticity centers were associated with the Harrah storm, which lasted beyond 1613.

The most significant storm structure results for cell A_1 are the relation between airflow structure and the vorticity centers. The 1555 time was presented in most detail. The updraft is tilted toward the left flank at low and mid-levels due to the southerly momentum of the low-level air. Cyclonic and anticyclonic downdrafts existed along the right and left storm flanks, respectively. The descending air along the right flank presumably mixes with the lower level southerly flow, and is steered into the storm's front flank. The descending air along the left

flank turns anticyclonically, reverses direction over a gradual turn, and undercuts the tilted updraft to form a gust front. The observations suggest the low-level tornado cyclone (i.e., cyclonic vorticity) and hook echo result from horizontal shears between the descended cold air outflow and the warm air inflow jet. The three other times (1545, 1605, and 1613) show similar characteristics to the above though after 1555 the airflow is modified due to new cell growth along the right flank of cell A_1.

The high-speed inflow and updraft are suggested to be important in forming the three-dimensional airflow structure of the Harrah storm. The tilting and divergence terms of the vorticity equation were computed for a qualitative discussion of this structure. Both terms are quite large with magnitudes of $10^{-5}s^{-2}$. While no data were available prior to 1545, a sequence of events leading to the intensification of the storm vorticity centers is surmised from the vorticity equation. In early stages of the storm lifetime, a vortex doublet may exist at mid-levels (similar to Schlesinger's numerical model results), due to tilting of horizontal vortex tubes by the updraft. Rain and hail falling out of the rear of a tilted updraft along the left flank evaporate in the low θ_w mid-level air. The rain-cooled descending air would increase horizontal gradients of vertical velocity, parallel to the low-level flow. The tilting term would then tend to concentrate anticyclonic vorticity

as a result of these increased gradients of vertical velocity. The anticyclonic vorticity production may eventually cause the descending air along the left flank to reverse direction. A flow reversal would increase vertical shear, and hence an increase of anticyclonic vorticity production by the tilting term would be expected. The low-level circulation may have existed previously due to concentration of ambient mesoscale vorticity, but may be intensified as a result of the descended air.

The vorticity production calculations in Chapter V suggest a tornado would be formed in about 30 min. The mechanism of tornado initiation is difficult to extract from the observations though some clues are present. The strong $10^{-2}s^{-1}$ vertical shear found in the vicinity of the tornado above and at the leading edge of the outflow (right rear flank) is one notable structural feature. Another feature is cell A_3 which is conjectured to be a flanking cumulus tower. Though the tornado is a sub-grid scale phenomenom, it is suggested that the strong vertical shears combined with vertical motion due to cell A_3 or other flanking cells (if they exist) is sufficient to produce tornadic vorticity by tilting of horizontal vorticity. In this connection, it is noted that Brown et al. (1975) find the tornado to nearly coincide with the tornado cyclone on April 20, 1974. The storm structure differences of the April 20, 1974, and the June 8, 1974, storm which produce tornadoes in

different locations with respect to the parent cyclone may shed light on tornado initiation mechanisms.

This study has documented that vorticity production resulting from the storm and its environment are sufficient to produce a tornado cyclone and a tornado. The relative importance of the tilting and divergence terms is not clear from the computations as a result of inaccuracies in the winds. The vorticity equation was not balanced due to wind errors and insufficient sampling of data in time. It would be desirable to have more complete data sets over the entire storm evolution to further study the causal relations proposed.

The extremely large vorticities ($>10^{-2}s^{-1}$) in the storm suggest large storm deviation from Magnus type forces, while the Harrah storm motion is only 5° to the right of the mean tropospheric winds. It was hoped that the simplistic model with an anticyclonic vortex (Appendix A, Model B) would reduce the steering force, but instead it was increased. Several possible explanations were given for forces opposing the steering force. At present the frequency of storms which have mid-level vortex doublets, and whether anticyclonic updrafts exist is not known. Thus, whether simple potential flow analogies are adequate models remain to be tested.

The requirement for a three-dimensional numerical model to clearly depict three-dimensional observed airflow

is suggested. It was mentioned earlier that the observations have a number of similar features to Schlesinger's numerical model for a storm in a sheared environment (his Case P3). His model cloud had a 12 min lifetime, a vertical depth of 6 km, and did not include precipitation. A three-dimensional model with inclusion of a precipitation parameterization (e.g., Kessler, 1969) would be helpful in verification of the downdraft structure.

The overall results have answered some questions, yet leave many unanswered questions. The Harrah storm is one storm and only through further observational studies may we verify these observations, and the dynamical mechanisms suggested by the vorticity equation computations.

REFERENCES

Actemeier, G. L., 1975: Doppler velocity and reflectivity morphology of a severe left-moving split thunderstorm. Preprints, Sixteenth Radar Meteor. Conf., Houston, Texas, Am. Meteor. Soc., Boston, pp. 93-98.

Armijo, L., 1969: A theory for the determination of wind and precipitation velocities with Doppler radars. J. Atmos. Sci., 26, 570-573.

Barnes, S. L., 1970: Some aspects of a severe, right-moving thunderstorm deduced from mesonetwork rawinsonde observations. J. Atmos. Sci., 27, pp. 634-648.

Brady, P. J., 1976: Multivariate experimental design in meteorology. Ph.D. Dissertation, University of Oklahoma, 121 pp.

Brown, R. A. and K. C. Crawford, 1972: Doppler radar evidence of severe storm high-reflectivity cores acting as obstacles to airflow. Preprints, Fifteenth Radar Meteor. Conf., Boston, Am. Meteor. Soc., pp. 16-21.

_____, D. W. Burgess, J. K. Carter, L. R. Lemon and D. Sirmans, 1975: NSSL dual-Doppler radar measurements in tornadic storms: a preview. Bull. Amer. Meteor. Soc., 56, 524-527.

Browning, K. A., editor, 1965: A family outbreak of severe local storms--a comprehensive study of the storms in Oklahoma on 26 May 1963, Part I. Air Force Cambridge Research Laboratories, Special Rpt. 32, 346 pp.

_____, 1975: The structure and mechanism of hailstorms. NHRE Symposium/Workshop on Hail, Estes Park, Colo., National Center for Atmospheric Research, pp. 1-106.

_____, J. C. Fankhauser, J. P. Chalon, P. J. Eccles, R. G. Strauch, F. H. Merrem, D. J. Musil, E. L. May and W. R. Sand, 1976: Structure of an evolving hailstorm, Part V: Synthesis and implications for hail growth and hail suppression. Mo. Wea. Rev., 104, 603-610.

_____, and F. H. Ludlam, 1962: Airflow in convective storms. Quart. J. Roy. Meteorol. Soc., 88, pp. 117-135.

_____, and G. B. Foote, 1975: Airflow and hail growth in supercell storms and some implications for hail suppression. NHRE Tech. Rept. 75/1, National Center for Atmospheric Research, Boulder, 75 pp.

Burgess, D. W. and R. A. Brown, 1973: The structure of a severe right-moving thunderstorm: new single Doppler radar evidence. Preprints, Eighth Conf. Severe Local Storms, Boston, Am. Meteor. Soc., pp. 40-43.

_____, L. R. Lemon and Rodger A. Brown, 1975: Tornado characteristics revealed by Doppler radar. Geophysical Research Letters, 2, pp. 183-184.

Byers, H. R. and R. R. Braham, 1949: The Thunderstorm. Washington, D.C., U. S. Govt. Printing Office, 287 pp.

Charba, J. and Y. Sasaki, 1971: Structure and movement of the severe thunderstorms of 3 April 1964 as revealed from radar and surface mesonetwork data analysis. J. Meteor. Soc. Japan, 49, pp. 191-214.

Chisholm, A. J., 1970: Alberta hailstorms: a radar study and model. Ph.D. Thesis, McGill Univ., 237 pp.

Connell, J., 1975: A non-thermal mechanism for forcing cumulonimbus cloud. J. Appl. Meteor., 14, pp. 1406-1410.

Costen, R. C., 1975: Theory for the drift of severe local storms with applications to the storm of April 21, 1961, near Topeka, Kansas. Preprints, Ninth Conf. on Sev. Loc. Storms., Boston, Am. Meteor. Soc., pp. 124-131.

Crawford, K. C. and R. A. Brown, 1972: Doppler velocity measurements in an approaching squall line. Preprints, Fifteenth Radar Meteor. Conf., Boston, Am. Meteor. Soc., pp. 27-34.

Danielson, E., 1975: The conceptual theory of tornado genesis based on macro-, meso- and microscale processes. Preprints, Ninth Conf. on Sev. Loc. Storms, Boston, Am. Meteor. Soc., pp. 376-383.

Darkow, G. L., 1969: An analysis of over sixty tornado proximity soundings. Preprints, Sixth Conf. on Sev. Loc. Storms, Boston, Am. Meteor. Soc., pp. 182-183.

_____, 1969: Deflecting forces on non-rotating convective systems due to environmental shear. Preprints, Sixth Conf. on Sev. Loc. Storms, Boston, Am. Meteor. Soc., pp. 20-23.

Davies-Jones, R. P., 1974: Discussion of measurements inside high-speed thunderstorm updrafts, J. Appl. Meteor., 13, pp. 710-717.

_____, and E. Kessler, 1974: Tornadoes, Weather and Climate Modification, John Wiley, New York, pp. 552-595.

Doviak, R. J., D. Sirmans, D. Zrnic, and G. B. Walker, 1976b: Resolution of pulse-Doppler radar range and velocity ambiguities in severe storms. Preprints, Seventeenth Radar Meteor. Conf., Seattle, Washington, Am. Meteor. Soc., Boston.

_____, P. S. Ray, R. G. Strauch and L. J. Miller, 1976a: Error estimation in wind fields derived from dual Doppler radar measurements. J. Appl. Meteor., 15, No. 7.

Dutton, J. A. and G. H. Fichtl, 1969: Approximate equations of motion for gases and liquids, J. Atmos. Sci., 26, pp. 241-254.

Eddy, Amos, 1963: Kinematic divergence and large scale energy conversion. Arctic Meteorology Research Group, McGill University, Publication No. 60, Ph.D. Dissertation, 105 pp. (Available from Department of Meteorology, McGill University)

_____, 1973: The objective analysis of atmospheric structure. Meteor. Soc. Japan, 51, pp. 450-457.

Fawbush, E. J. and R. C. Miller, 1954: The types of air masses in which North American tornadoes form. Bull. Am. Meteor. Soc., 35, pp. 154-165.

Fankhauser, J. C., 1971: Thunderstorm-environment interactions determined from aircraft and radar observations, Mo. Wea. Rev., 99, pp. 171-192.

Foote, G. B. and P. S. duToit, 1969: Terminal velocities of raindrops aloft. J. Appl. Meteor., 8, pp. 249-253.

Fujita, T., 1963: Analytical mesometeorology: a review. Meteor. Mono., 5, No. 27, pp. 77-123.

_____, and H. Grandoso, 1968: Split of a thunderstorm into anticyclonic and cyclonic storms and their motion as determined from numerical model experiments. J. Atmos. Sci., 25, pp. 416-439.

Gandin, L. S., 1963: Objective analysis of meteorological fields. Israel Program of Scientific Translation, 242 pp. (Available from NTIS (TT-65-50007)).

Golden, J. H., 1974: Life cycle of Florida Keys' waterspouts, NOAA-ERL NSSL-70, U. S. Dept. of Comm., 147 pp.

Goldman, J. S., 1966: The role of the Kutta-Joukowski force in cloud systems with circulation. NSSL Tech. Rept. 27, U. S. Weather Bureau, Washington, D.C.

Gray, W. M., 1969: Hypothesized importance of vertical windshear in tornado genesis. Preprints, Sixth Conf. on Sev. Loc. Storms, Boston, Am. Meteor. Soc., pp. 230-237.

Gunn, R. and G. D. Kinzer, 1949: The terminal velocity of fall for water droplets in still air. J. Appl. Meteor., 6, pp. 243-248.

Hammond, C. R., 1967: Study of a left moving thunderstorm of 23 April 1964. ESSA Tech. Memo. IERTM-NSSL 31.

Henderson, J. H., 1974: A detailed description of the internal structure of a thunderstorm. NOAA Tech. Memo. ERL NSSL-69, pp. 111-124.

Heymsfield, G. M., 1976: Statistical objective analysis of a tornadic storm. J. Appl. Meteor., 15, pp. 59-68.

Holton, J. R., 1972: An introduction to dynamic meteorology. Academic Press, New York.

Hwang, H. J. and Y. J. Lin, 1973: A numerical study of some effects of the low level moisture distribution on the thermal structure of the severe thunderstorm. Preprints, Eighth Conf. on Sev. Loc. Storms, Boston, Am. Meteor. Soc., pp. 273-278.

Jessup, E. A., 1972: Interpretations of chaff trajectories near a severe thunderstorm. Mon. Wea. Rev., 100, pp. 653-661.

Joss, J. and A. Waldvogel, 1970: Raindrop size distribution and Doppler velocities. Preprints, Fourteenth Radar Meteor. Conf., Boston, Am. Meteor. Soc., pp. 153-156.

Kessler, E., 1969: On the distribution and continuity of water substance in atmospheric circulations. Meteor. Mono., 10, No. 33, 84 pp.

_____, 1975: Condensate content in relation to sloping updraft parameters. J. Atmos. Sci., 32, pp. 443-444.

Kraus, M. J., 1974: Doppler radar investigation of flow patterns within thunderstorms. AFCRL-TR-74-0290, 86 pp.

Kropfli, R. A. and L. J. Miller, 1976: Kinematic structure and flux quantities in a convective storm from dual-Doppler radar observations. J. Atmos. Sci., 33, pp. 520-529.

Lemon, L. R., 1974: Interaction of two convective scales within a severe thunderstorm: a case study. NOAA Tech. Memo. ERL NSSL-71, pp. 1-16.

Maddox, R. A. and W. M. Gray, 1973: A frictionally driven model for tornado genesis with similarities to hurricane genesis. Preprints Eighth Conf. on Sev. Loc. Storms, Boston, Am. Meteor. Soc., pp. 203-206.

Margason, R. J., 1969: Analytic description of the jet-wake cross sections for a jet normal to a subsonic free stream. NASA SP-216, Washington, D.C., pp. 131-140.

Marwitz, J. D., 1972: Structure and motion of severe hailstorms. J. Appl. Meteor., 11, pp. 166-201.

McCarthy, J., G. M. Heymsfield and S. P. Nelson, 1974: Experiment to deduce tornado cyclone inflow characteristics using chaff and NSSL dual-Doppler radars. Bull. Amer. Meteor. Soc., 55, 1130-1133.

_____, G. M. Heymsfield, L. G. Tidwell and S. P. Nelson, 1975: Evolution of a tornadic cyclone as seen by dual-Doppler, instrumented airplane and chaff. Preprints Ninth Conf. on Sev. Loc. Storms, Boston, Am. Meteor. Soc., pp. 389-395.

Miller, L. J. and R. G. Strauch, 1974: A dual-Doppler radar method for the determination of wind velocities within precipitating weather systems. Remote Sens. of Envir., 3, pp. 219-235.

Milne-Thompson, K. M., 1960: Theoretical Hydrodynamics, 4th ed., Macmillan, New York.

Morton, B. R., 1966: Geophysical vortices, Progress in Aeronautical Sciences, 7, Pergamon Press, New York, N.Y., pp. 145-193.

Newton, C. W., 1965: Severe convective storms. Advan. Geophys., 12, pp. 257-308.

_____, and H. R. Newton, 1959: Dynamical interactions between large convective clouds and environment with vertical shear. J. Appl. Meteor., 16, 483-496.

_____, and J. C. Fankhauser, 1964: On the movement of convective storms, with emphasis on size discrimination in relation to water budget requirements. J. Appl. Meteor., 3, pp. 651-668.

Pinus, N. Z. and V. D. Litvinova, 1962: On the intensity of turbulence in clouds. Bull. (Izvestiya) Acad. Sci. USSR, Geophysics Series, 1, pp. 86-88.

Ray, P. S., R. J. Doviak, G. B. Walker, D. Sirmans, J. Carter and B. Bumgarner, 1975: Dual Doppler observation of a tornadic storm. J. Appl. Meteor., 14, pp. 1521-1530.

Schlesinger, R. E., 1975: A three-dimensional numerical model of an isolated deep convective cloud: preliminary results. J. Atmos. Sci., 32, pp. 934-957.

Tegtmeier, S. A., 1974: The role of the surface, subsynoptic, low pressure system in severe weather forecasting. M.S. Thesis, University of Oklahoma, 66 pp.

Tidwell, L. G., 1975: A synoptic and sub-synoptic study of the June 8, 1974, severe thunderstorm and tornado outbreak in Oklahoma., 65 pp.

Zrnic, D. S. and R. J. Doviak, 1975: Velocity spectra of vortices scanned with a pulse-doppler radar. J. Appl. Meteor., 14, pp. 1531-1539.

APPENDIX A

SOME SPECULATIONS ON STORM TRANSLATIONAL MOTION

Studies of the translational motion of severe tornadic storms suggest that they move both to the right and left of the mean tropospheric winds. The Magnus force concept provides a means by which a cyclonically (anticyclonically) rotating updraft may deviate to the right (left) as a result of pressure gradient forces on the cylinder. Schlesinger (1975) found in his numerical model that pressure gradient forces existed which would tend to produce right deviate motion. The Harrah storm moved only 5° to the right, while other storms deviate to the right by as much as 60°. The strong vortex cores in the Harrah storm suggest they are important in determining the motion of the storm.

Potential Flow Models

The Magnus concept does not consider the presence of an anticyclonic vortex, as suggested by the observations in Chapter IV. To examine the effect of this additional vortex, two potential flow analogies are considered: A) a vortex doublet, and B) a cyclonically rotating solid cylin-

der with an anticyclonic vortex outside the cylinder. Model A considers no barrier effects, while Model B considers the updraft as a non-mixing barrier. It should be noted that potential flow theory assumes incompressible, irrotational flow, and effects of vertical motion are not considered with this two-dimensional flow.

For a vortex doublet in a uniform flow, (Model A) the complex potential, ω ($=\Phi + i\Psi$, where Φ is velocity potential and Ψ is stream function), reduces to the complex potential of a cylinder in a uniform flow (Milne-Thompson, 1960). Thus no net pressure force perpendicular to the flow is exerted on the doublet.

In Model B, it is assumed that the observed flow may be represented by a cyclonically rotating cylinder and an anticyclonic circulation. The vortex doublet is oriented perpendicular to a uniform flow field, U, as shown in Fig. A1. Also it is specified that the anticyclonic and cyclonic circulations are of equal strengths, $-\kappa$ and $+\kappa$, respectively, where the κ are defined at a radius a from the vortex center. Furthermore, the anticyclonic circulation is considered to be outside of the updraft represented by a cylinder. Following a similar approach to Milne-Thompson (1960), the complex potential for this arrangement may be found by applying the circle theorem:

$$\omega = -U(Z + a^2/Z) - i\kappa\left[\log (Z-f) - \log(Z-f')\right] , \qquad (A1)$$

where a is the radius of the cylinder, $Z = X + iY$, $f = iY_0$ is a singularity and is the position of the anticyclonic vortex, $f' = ia^2/f$ is a singularity, $\kappa = 2\pi\Gamma$, and Γ is circulation. The complex velocity for this flow ($= -u + iv$) is derived as

$$d\omega/dz = -U(1-a^2/Z^2) - i\kappa\left[1/(Z-f) + 1/(Z-f')\right] \quad . \qquad (A2)$$

From the theorem of Blasius the pressure forces on a fixed cylinder placed in a steady and irrotational flow (neglecting external forces), may be computed. The forces per unit arc length on the cylinder F_d and F_s in the X and Y directions are thus given by (the proof may be found in Milne-Thompson)

$$F_d = 0 \ , \quad F_s = \rho\phi(d\omega/dZ)^2 dZ \ , \qquad (A3)$$

where the integral is taken around the contour of the cylinder. (A3) is evaluated from (A1) by expressing quantities as partial fractions and applying the residue theorem. The resulting steering force (perpendicular to the flow) on the updraft is derived as

$$F_s = -2\kappa\rho\pi\left[U(1-a^2/Y_0^2) + \kappa Y_0/(Y_0^2-a^2)\right] \quad . \qquad (A4)$$

The solution is valid when $Y_0 > 2a$, due to the singularity at f' and also κ is defined at distances greater than a from the vortex centers. When $Y_0 > 2a$, the updraft is steered to the right of U by the Magnus force $(-2\kappa\rho\pi U)$ times

a constant less than one, plus another term also less than zero. This result is also suggested by the Bernoulli equation for a steady state, incompressible fluid: $p + \frac{1}{2}\rho U^2$ = constant, where p is pressure. To the left of the rotating cylinder (facing downstream), the anticyclonic circulation increases flow in a direction opposing the uniform flow, resulting in lower speeds in this region. Thus, the pressure on this side of the cylinder would become increased, producing a larger deviation force. When the anticyclonic vortex is far removed from the updraft ($Y_0 >> a$), F_s becomes the Magnus force. Thus, the addition of the anticyclonic vortex produces a larger force to the right of the mean winds, for the case of a rotating updraft.

The magnitude of the horizontal pressure gradient force in these two models depends on the extent to which the updraft acts as a barrier to the flow. It would also depend on the relative strengths of each vortex, and the positions of the vortex doublet relative to the updraft. The force on the cylinder (F_d) parallel to the uniform stream is zero in both cases. In reality a drag force ($F_d \neq 0$) would exist in Model B due to separation of flow.

Comparison With Harrah Storm

The potential flow models may be compared with observations from the Harrah storm. As an example, the observations for cell A_1 at 6.5 km altitude and 1555 (Fig. 26) sug-

gest that a ≃ 2.5 km, Y_0 ≃ 5 km, κ ≃ $10^5 m^2 s^{-1}$, and U = $\vec{V}_r$ = 21.6 m s^{-1} from 251°. The streamlines and isotachs are shown in Fig. Ala for Model B. The pressure coefficient distribution, steering force, and drag force F_d are shown in Fig. Alb. The pressure coefficient, C_p, is defined by $(p - p_{env})/(\frac{1}{2}\rho U^2)$, where p_{env} is the pressure at large distances from the cylinder. For comparison the wind vectors in Fig. 19 at 1555 and 6.5 km should be used.

Model B shows an enlarged barrier flow region, approximately 12 km in diameter. A wind maximum greater than 40 m s^{-1} exists along the right flank and a second wind maximum 30 m s^{-1} exists to the northwest of the anticyclonic circulation. A speed minimum exists between these two wind maxima. The flow for Model A would be quite similar except that the two wind maxima would be equal. Recall that inside of the updraft, winds are from the south-southeast due to vertical momentum transport. The streamlines (Fig. Ala) and the wind vectors (Fig. 19, 6.5 km, 1555) are qualitatively similar upwind of the updraft, while there is less agreement downwind of the updraft. The potential flow model would be in least agreement in the downwind region, since it does not consider separation of flow, or a stagnation region. In view of the limitations of these models, it appears that both the updraft and downdraft produce an "effective" barrier with a diameter of about 12 km.

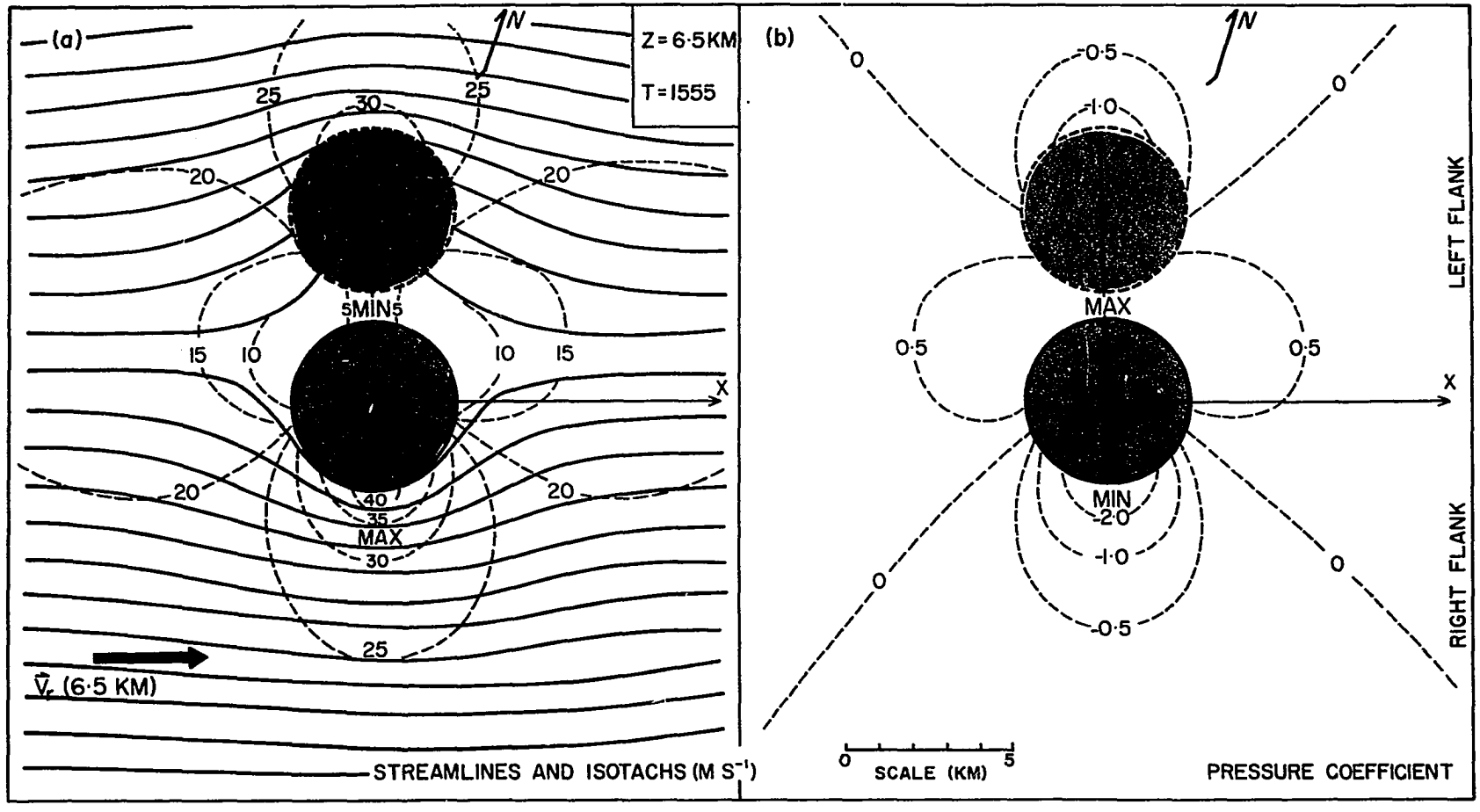

Fig. A1. Horizontal view for potential flow model of well developed updraft-downdraft couplet when updraft acts as barrier. Shown are: (a) streamlines and isotachs (m s^{-1}) and, (b) pressure coefficient, Cp. Circle in center (thick-solid curve) shows updraft boundary, and thick dashed curve is the anticyclonic downdraft. Maximum (MAX) and minimum (MIN) wind speeds and pressures are indicated in (a) and (b), respectively. The steering force, F_s, drag force, F_d, and F_i due to southerly momentum, are shown in (b).

The steering force for Model B computed according to (A4) is $F_s/\rho = -2.6 \times 10^7 m^3 s^{-2}$, while the Magnus force alone would be $F_s/\rho = -1.25 \times 10^7 m^3 s^{-2}$. Thus the force is about twice as large as the Magnus force. The ratio of the Magnus to drag force gives the tangent of the deviation angle which according to Fujita and Grandoso (1968) is theoretically $2\pi v_\theta/U$, where v_θ is rotational speed. The storm would deviate greater than 45° using the 6.5 km data, while the mean tropospheric winds relative to cell A_1 would suggest an even larger angle. It is possible that F_d is increased due to the "effective" barrier region. The larger F_s due to Model B combined with a larger F_d would also result in approximately 45° deviation angle.

Factors other than the effectiveness of the updraft as a barrier, and positions of the vortex pair relative to the updraft, may be responsible for the small (5°) deviation of cell A_1 from the mean tropospheric winds. One explanation is the vertical advection of strong low-level southerly momentum in the updraft opposing F_s. Such an opposing force is indicated by F_i in Fig. Alb. Another opposing pressure gradient force is the interacting flow around cell B_1. Darkow (1969) has shown that a non-rotating cylinder in a sheared flow also is deflected with forces comparable to the Magnus force. The environmental winds may become anticyclonically sheared due to cell B_1, resulting in a force opposing F_s. Finally, Costen (1975) sug-

gests that the horizontal component of buoyant force opposes the Magnus force. His model however, has the updraft tilting along the direction of storm motion while the Harrah storm tilts in a direction perpendicular to storm motion. We have not considered storm propagation (e.g., Charba and Sasaki, 1971) since a single updraft was tracked. In summary, the steering of the storm would seem to depend on the internal storm structure, for example tilt of the updraft, rotation of the updraft, etc. The applicability of the above models is questionable in view of the complexity of dynamical and microphysical processes operative in the storm.